LASER INTERFEROMETER GRAVITATIONAL WAVE OBSERVATORY

LIGO Laboratory / LIGO Scientific Collaboration

LIGO-T060269-02-D *ADVANCED LIGO* 8/20/07

Input Optics Subsystem
Preliminary Design Document

Muzammil A. Arain, Antonio Lucianetti, Rodica Martin, Guido Mueller, Volker Quetschke, David Reitze, David B. Tanner, Luke Williams, and Wan Wu

Distribution of this document:
LIGO Science Collaboration

This is an internal working note
of the LIGO Project.

California Institute of Technology
LIGO Project – MS 18-34
1200 E. California Blvd.
Pasadena, CA 91125
Phone (626) 395-2129
Fax (626) 304-9834
E-mail: info@ligo.caltech.edu

Massachusetts Institute of Technology
LIGO Project – NW17-161
175 Albany St
Cambridge, MA 02139
Phone (617) 253-4824
Fax (617) 253-7014
E-mail: info@ligo.mit.edu

LIGO Hanford Observatory
P.O. Box 1970
Mail Stop S9-02
Richland WA 99352
Phone 509-372-8106
Fax 509-372-8137

LIGO Livingston Observatory
P.O. Box 940
Livingston, LA 70754
Phone 225-686-3100
Fax 225-686-7189

http://www.ligo.caltech.edu/

Table of Contents

Table of Tables

Table of Figures

Abstract

This document presents aspects of the Preliminary Design for the Advanced LIGO Input Optics Subsystem relating to power control, overall modulation method, the input mode cleaner, and the mode matching telescope as well as ancillary IOO functions. The IOO preliminary design is consistent with the requirements listed in LIGO-T020020-01-D, "Input Optics Subsystem Design Requirements Document." The Input Optics Subsystem includes the RF modulation of the light, the input mode cleaner, optical isolation and distribution of length and alignment control signals, mode matching of the light to the interferometer, and beam steering into the interferometer. The scope of the IOO includes the following hardware: phase modulation Pockels cells, photodetectors and related protective shutter, active jitter suppression system, input mode cleaner optics, suspensions, Faraday isolator, and mode matching telescopes.

This document does not address the electro-optic modulators or Faraday Isolators in detail; their preliminary design was presented in "Upgrading the Input Optics for High Power Operation", LIGO T060267-00-D.

1 Introduction

1.1 Purpose

This document along with supporting analysis documents presents the current design status for the Advanced LIGO Input Optics. The design information in this document supersede that presented in the IOO Conceptual Design and are intended to present a detailed preliminary design for the LIGO Input Optics Subsystem which conform to the *Advanced LIGO Input Optics Design Requirements,* LIGO-T020020-01-D. The intended audience for this document is the LIGO Detector Team.

1.2 Scope

This document details the current status of the Input Optics design effort. The IOO provides for the conditioning of the laser light after the PSL and before the IFO input, and for the disposition of the IFO reflected light to the ISC subsystems. It includes power control into the interferometer, RF phase modulation of the light for the generation of length and alignment control sidebands; mode-matching, a mode cleaner cavity for spatial as well as amplitude and frequency filtering of the PSL beam; mode matching of the light to the IFO; beam steering into the IFO; and diagnostic beam pick-offs for the ISC subsystems.

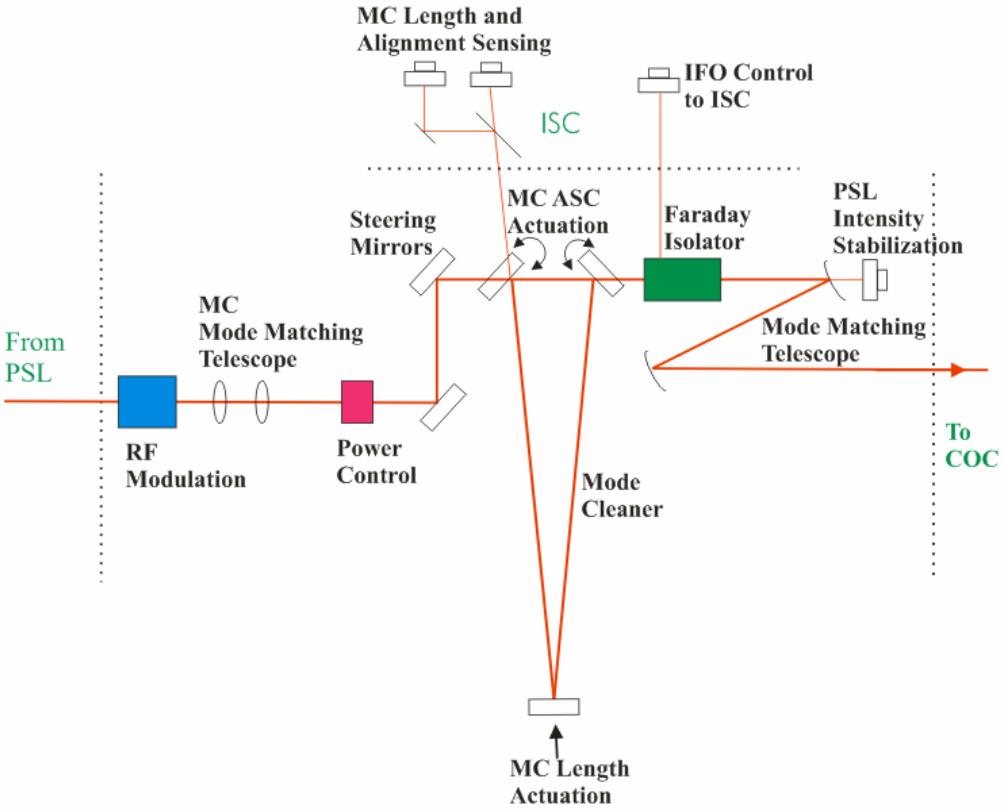

Figure 1.1. Block Diagram of the Input Optics

1.2.1 IO Subsystems

The Input / Output (IOO) subsystem layout consists of the following units, schematically shown in Figure 1.1:

- Outside vacuum
  - RF modulation
  - Power control into the IFO
  - Steering and mode matching optics for the input mode cleaner
  - Required IOO diagnostics
- In vacuum
  - Input mode cleaner cavity
  - IFO mode matching and beam steering
  - Faraday isolation and signal extraction for ISC
  - Signal extraction for PSL intensity control

1.3 Definitions

- Modulation index *m*: The application of RF sidebands using an EOM results in a modulated output field $E_{mod} = E_{in}\, exp[-i\omega t - im \cos \Omega t]$ where ω and Ω are the carrier and modulation frequencies and E_{in} is the input field amplitude.

1.4 Acronyms

AM	Amplitude Modulation
AOS	Auxiliary Optics Support (detector subsystem)
BS	Beamsplitter (optical component)
CD	Conceptual Design
CDS	Control and Data System (detector subsystem)
CMRR	Common Mode Rejection Ratio
COC	Core Optics Components (detector subsystem)
DC	Direct Current (steady state - low frequency)
EOM	Electro-Optic Modulator (optical hardware)
ETM	End Test Mass (optical component)
FI	Faraday Isolator (optical component)
GPM	Gallons per Minute (flow rate)
GW	Gravitational Wave
HAM	Horizontal Access Module
HWP	Half-Wave Plate (optical hardware)
IFO	LIGO Interferometer
IMC	Input Mode Cleaner (formerly, just the ‘MC’)
IO	Input Optics (detector subsystem)
ISC	Interferometer Sensing / Control (detector subsystem)
ITM	Input Test Mass (optical component)
LOS	Large Optic Suspension
LVEA	Laser and Vacuum Equipment Area
MMT	IFO Mode Matching Telescope
MSPRC	Marginally Stable Power Recycling Cavity
MZ	Mach-Zehnder Interferometer

Nd:YAG	Neodymium doped Yttrium Aluminum Garnet
PDH	Pound-Drever-Hall
PM	Phase Modulation
PSL	Pre-Stabilized Laser (detector subsystem)
PZT	Piezo-electric Transducer (mechanical hardware)
RC	Radius of Curvature of a Reflective Mirror
RF	Radio Frequency
RM	Recycling Mirror (detector subsystem)
SEI	Seismic Isolation (detector subsystem)
SM	Suspended Steering Mirror
SOS	Small Optic Suspension
SPRC	Stable Power Recycling Cavity
TBD	To Be Determined
TCS	Core Optics Thermal Compensation System
TGG	Terbium-Gallium-Garnet (optical material used in Faraday Isolators)
TFP	Thin Film Polarizer (optical hardware)
WFS	Wave Front Sensors

1.5 Applicable Documents

1.5.1 LIGO Documents

Advanced LIGO Input Optics Preliminary Design Document, LIGO T-020020-01-D

Advanced LIGO Input Optics Conceptual Design Document, LIGO T-020027-00-D

Advanced LIGO Input Optics Subsystem: Design Requirements Review Panel Report, LIGO-T020065-02-R

Generic Input Optics Requirements and Standards, LIGO-E070170-00-D

Upgrading the Input Optics for High Power Operation, LIGO- T060267-00-D

Response to EOM-FI Preliminary Design Action Items, LIGO T060081-00-D

Modulators and Isolators for Advanced LIGO, LIGO-G060361-00-D

Effect of sideband of sideband on 40m and Advanced LIGO, LIGO-G040081-00-R

Analysis of Stray Magnetic Fields from the Advanced LIGO Faraday Isolator, LIGO T060025-00-Z

1.5.2 Non-LIGO Documents

E. Khazanov, N. Andreev, A. Mal'shakov, O. Palashov, A. Poteomkin, A. M. Sergeev, A. Shaykin, V. Zelenogorsky, Igor Ivanov, Rupal Amin, Guido Mueller, D. B. Tanner, and D. H. Reitze, "Compensation of thermally induced modal distortions in Faraday isolators", IEEE J. Quant. Electron. **40**, 1500-1510 (2004).

V. Quetschke, J. Gleason, M. Rakhmanov, J. Lee, L. Zhang, K. Yoshiki Franzen, C. Leidel, G. Mueller, R. Amin, D. B. Tanner, and D. H. Reitze, Adaptive control of laser modal properties", Opt. Lett. **31**, 217-219 (2006).

2 Overview of Design Status

We believe that the IOO design is substantially complete at the Preliminary Design level. Several of the IOO components will be tested in Enhanced LIGO, including the electro-optic modulators and the Faraday Isolator.

2.1 Summary of the design changes from the Conceptual Design

Since the completion of the IOO Conceptual Design in April 2002, there have been the following changes to the IOO design:

2.1.1 In-vacuum Layout

Several changes have been made to the in-vacuum layout. Due to the relocation of HAM3 (→ HAM1) and the movement of the ISC sensing table into HAM 1, the beam injection from the PSL table has changed. As of this writing, the injection path has not been completely determined but it will most likely be through HAM1

In addition, the ISC group is considering the possibility of changing from unstable to stable power and signal recycling cavities. A change in the PRC would affect the IOO since the mode matching telescope would be integrated within the PRC. While the marginally stable is still the baseline, we have developed a preliminary design level layout for the stable recycling cavity.

2.1.2 Modulation Method

The double demodulation length sensing scheme initially posed by ISC was discovered to be compromised by serial modulation (the 'sidebands-on-sidebands' problem) during work at the 40 m.[1] Thus, we have developed modulation schemes which do not produce sideband cross products.

Most of the preliminary design work has focused on developing requirements for and prototyping a Mach-Zehnder (MZ) modulation scheme. Some effort has also been directed at complex modulation methods (combined AM/PM) modulation.

We adopt the MZ modulation as the baseline for the preliminary design.

2.1.3 Reduction in the IMC finesse

The IOO CD proposed a finesse of ~ 2000 for the IMC was conservative based on expected performance of the PSL pointing and required jitter suppression. The high finesse coupled with high input powers results in very high intracavity powers (~ 100 kW) and peak intensities on the mirror surfaces (~ 700 kW/cm^2). This results in 100 mW absorption assuming a 1 ppm loss which leads to some degradation of the IMC performance at the highest power operating power.[2] In order to reduce the thermal loading on the IMC and relax the tolerances on mirror coatings:

We adopt a finesse of 500 for the Advanced LIGO input mode cleaner.

---

[1] O. Miyakawa, "Effect of sideband of sideband on 40m and Advanced LIGO", LIGO-G040081-00-R

[2] Franzen Melody work

Assuming that the required jitter specification of $\varepsilon_1 \sim (3 \times 10^{-5}/f)$ /Hz$^{1/2}$ for the PSL is met, the IMC will have no problems meeting the requirement. Recent results by the LZH and MPG groups indicate that this specification should be easily met.[3]

2.2 Areas that need more work

2.2.1 Complex (AM/PM) modulation

Since we have proposed MZ modulation as the baseline for AdvLIGO, we have put more effort into developing requirements and prototyping that system. An alternative modulation system based on the use of a single amplitude modulator and phase modulator is also possible.[4] We have performed experiments and modeling on the complex modulation at a level commensurate with a conceptual design, but not yet to the full maturity of a preliminary design.

2.2.2 Adaptive Mode-matching

The design of the mode matching telescope is fairly mature, including distances, mirror specifications and tolerances, etc. The adaptive mode matching concept has been changed recently from our original idea of CO2 heating of the MMT mirrors to a four segment ring heater (RH) on the FI DKDP. This was done to simplify the interface between IOO and AOS (the TCS system); TCS is responsible for keeping a constant mode target for the IOO to mode-match.

Preliminary modeling has been done on the RH, but we have not yet experimentally tested the idea.

2.2.3 IO Baffling

AOS and IOO recently redefined the interface to put the beam dump, suspension protection, and scattered light baffling for the IOO in the IOO subsystem. Since this scope change just occurred, not much has been done on this.

2.3 Areas that have been de-emphasized

2.3.1 Active jitter suppression

The IOO CD proposed high bandwidth active jitter suppression using electro-optic actuators (RTP-prisms) to complement the passive suppression provided by the IMC. As noted above, we have reduced the IMC finesse to mitigate thermal effects, and do not believe that these will be necessary.

Some preliminary experimental characterization has been done. In the event that more jitter suppression is needed, we will develop and prototype an active jitter suppression system based on RTP prisms.

---

[3] LIGO G070137-00-Z "Status of the Advanced LIGO PSL Development", Benno Willke

[4] V. Quetschke, "Complex Optical Modulation", LIGO G060452-00-Z

3 Interfaces with other subsystems

This section contains the IOO interfaces with other subsystems, including:

- Optical
- Electrical/Electronic
- Mechanical
- Water

3.1 PSL

3.1.1 Optical

3.1.1.1 Main Beam

The output beam from the PSL will be delivered to IOO at (X,Y,Z) = (144", 50" ,3") in the optical table local coordinate system defined in Figure 3.1. The spot size at the beam waist, of the PSL output beam shall be **TBD** mm. The PSL output beam waist location shall be within 5.0 cm of the PSL output beam location.

The polarization of the beam shall be such the electric field vector is horizontal to the table.

3.1.1.2 PSL Intensity Stabilization Beam

The intensity stabilization beam for the PSL will be delivered to the PSL photodiode located (**TBD PSL/ISC**) on the ISC seismic platform in HAM 1(7). At the IOO/PSL interface location, the spot size of the IOO output beam sample for power stabilization shall be **TBD PSL/IOO.** The power of the beam shall be **TBD PSL/ISC**.

3.1.2 Mechanical

The IOO shares an optical table with the PSL (PSL/IOO table). Components of the IOO that are located on the PSL table include

- modulation
- power control
- mode matching optics for the IMC,
- periscope and beam injection optics
- diagnostics

Figure 3.1 shows the proposed allocation of table area for each subsystem. The optical table itself as well as the physical enclosure surrounding the table (for controlling acoustic noise, air currents, dust, and thermal variations) is the responsibility of the PSL subsystem. Note that the PSL subsystem has not yet developed a detailed layout, and hence the allocation below is subject to change. A larger table may be required.

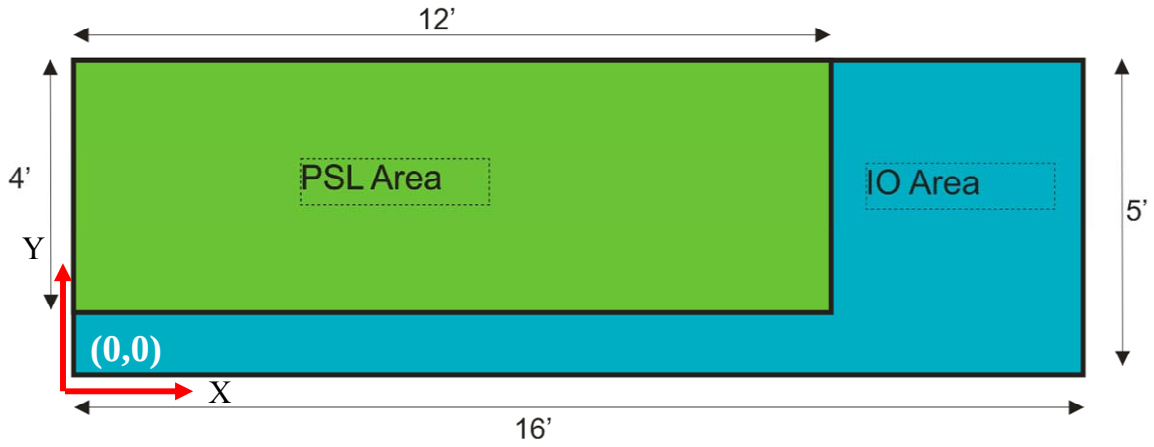

Figure 3.1. Defined IOO and PSL areas on the PSL table,

3.1.3 Water

The IFO power control beam dump must dissipate as much as 180W of power. Thus water-cooled beam dumps are required. The IOO power control beam dump requires the following

- Flow rate: 0.5 GPM
- 3/8” outside diameter
- 1/4” inside diameter
- Poly tubing; NPT fittings

Two other beam IOO dumps on the PSL table will not see more than a few Watts of power.

3.2 COC

3.2.1 Optical

The IOO delivers the main beam to the power recycling mirror (PRM) at (X,Y,Z) = (-3930.48mm, 222.355mm, -156.562mm) in LIGO Global Coordinates and direction cosines (θ_x, θ_y, θ_z) = (1, -0.0000951851, -2.5693 x 10^{-14}).

3.3 ISC/CDS

3.3.1 Optical

3.3.1.1 Interferometer Length and Alignment Sensing Beams

The IOO delivers diagnostic beams for interferometer length and alignment control to the ISC subsystem (REFL port) from Faraday Isolators located in HAMs 2,8 to the ISC sensing tables in HAM1,7 (**TBD/ISC)**. These beams will have spot sizes of 2 mm (**TBR ISC/IO**) with nominal powers of **TBD ISC** mW and up to **TBD ISC** W during lock acquisition of the IFO.

3.3.1.2 IMC length and alignment sensing beams

The IOO delivers diagnostic beams for IMC length and alignment control to the ISC subsystems (IMC_REFL port) using the reflected beam from IMC1 to the ISC sensing tables in HAM1,7 (**TBD/ISC)**. These beams will have spot sizes of 2 mm (**TBR ISC/IO**) with nominal powers of 300 mW and up to 6 W during lock acquisition of the IFO.

3.3.2 Electrical

3.3.2.1 RF modulation

The RF modulation signals for the two interferometer control sidebands and the IMC sideband are supplied to the IOO EOMs from ISC/CDS. IOO will use in-house resonant RTP electro-optic phase modulators[5] with the following characteristics:

- Electro-optic crystal: RTP
- Maximum Optical Power: 7 kW/cm^2
- Modulation Depth : 0.071 rad/V (depends on frequency; assumes matching circuit with Q=20, 20 mm long, 4 mm thick RTP crystal)
- Aperture: 4 mm
- Electrical Input Impedance: 50 Ω

At the time of this review, the choice of modulation frequencies is still under discussion by the ISC group. The signal characteristics are given in Table 1.

Table 1. Required RF inputs to IOO EOMs.

Sideband	*Frequency (MHz)*	*Max. Modulation Index*	*Voltage*	*RF Power, RMS (in 50 Ω)*
Upper IFO control sideband	9 (**TBR ISC)**	0.8 (**TBR ISC)**	10 V (**TBR ISC)**	2 W (**TBR ISC)**
Lower IFO control sideband	45 (**TBR ISC)**	0.8 (**TBR ISC)**	10 V (**TBR ISC)**	2 W (**TBR ISC)**
IMC control sideband	31.457 **(TBR IO)**	0.03	0.5 V	5 mW

3.3.2.2 Automated Power Control

The IOO provides power control of the PSL into the interferometer for commissioning as well as different operational modes of the interferometers. The CDS will provide control signals for rotating a 1/2 wave plate (see section 5.2.2.3). A motorized stage Newport URS-100 CC is controlled via an ESP 300 controller with a GPIB/RS232 interface. A script containing appropriate

[5] Upgrading the Input Optics for High Power Operation, LIGO- T060267-00-D

commands can be used to drive the ESP 300, or alternatively direct connection to the URS-100 CC can be used.

3.4 SEI

3.4.1 Mechanical

All in-vacuum IOO components are located on seismic isolation platforms in HAMs 1,2,3 and HAMs 7,8,9.

3.5 AOS

3.5.1 Optical

There are eleven optical lever beams from AOS that interface with the IOO subsystem. There is one optical lever on each of the suspended optics (IMC1, IMC2, IMC3, SM1, SM2, MMT1, MMT2, MMT3, and PRM), and one optical lever for each HAM table (HAM 2 and HAM 3).

AOS is responsible for the transmitters and receivers; IOO for the routing in the vacuum.

3.6 SUS

SUS supplies the IMC triple suspensions and MMT3 LOS-type suspension to the IO. All small optics suspensions (for SMs, small MMT mirrors) will use LIGO 1 small optics suspensions (SOS) manufactured by UF.

4 Optical Layout

This section includes the status of the physical layout of the IOO components for Advanced LIGO.

4.1 Assumptions

We assume that the LIGO facilities meet the specifications for vibrational and acoustic noise given in the Civil Construction Facilities *Design Configuration Control Document,* LIGO C960703-0.

4.2 PSL Table Layout

TBR Pending PSL layout

The layout of IOO optical components on the PSL table is shown in Figure 4.1 and Figure 4.2. All beam paths will be enclosed in either beam tubes or plexiglass enclosures to minimize environmental effects and for safety purposes. Red represents the main beam, and green represents beams that will be dumped or used for diagnostics.

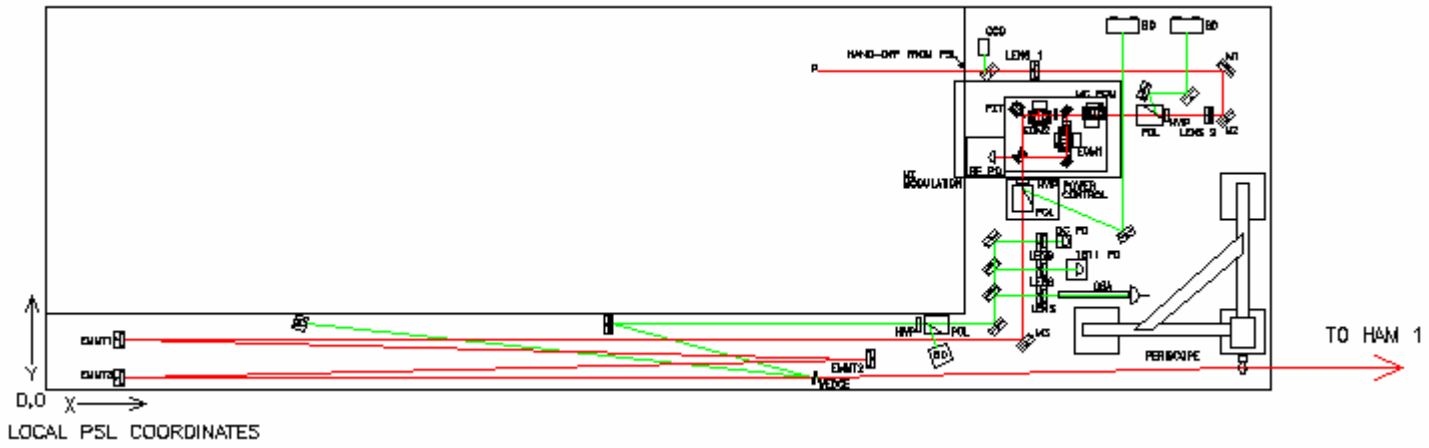

Figure 4.1. Diagram of the PSL Table showing IOO components

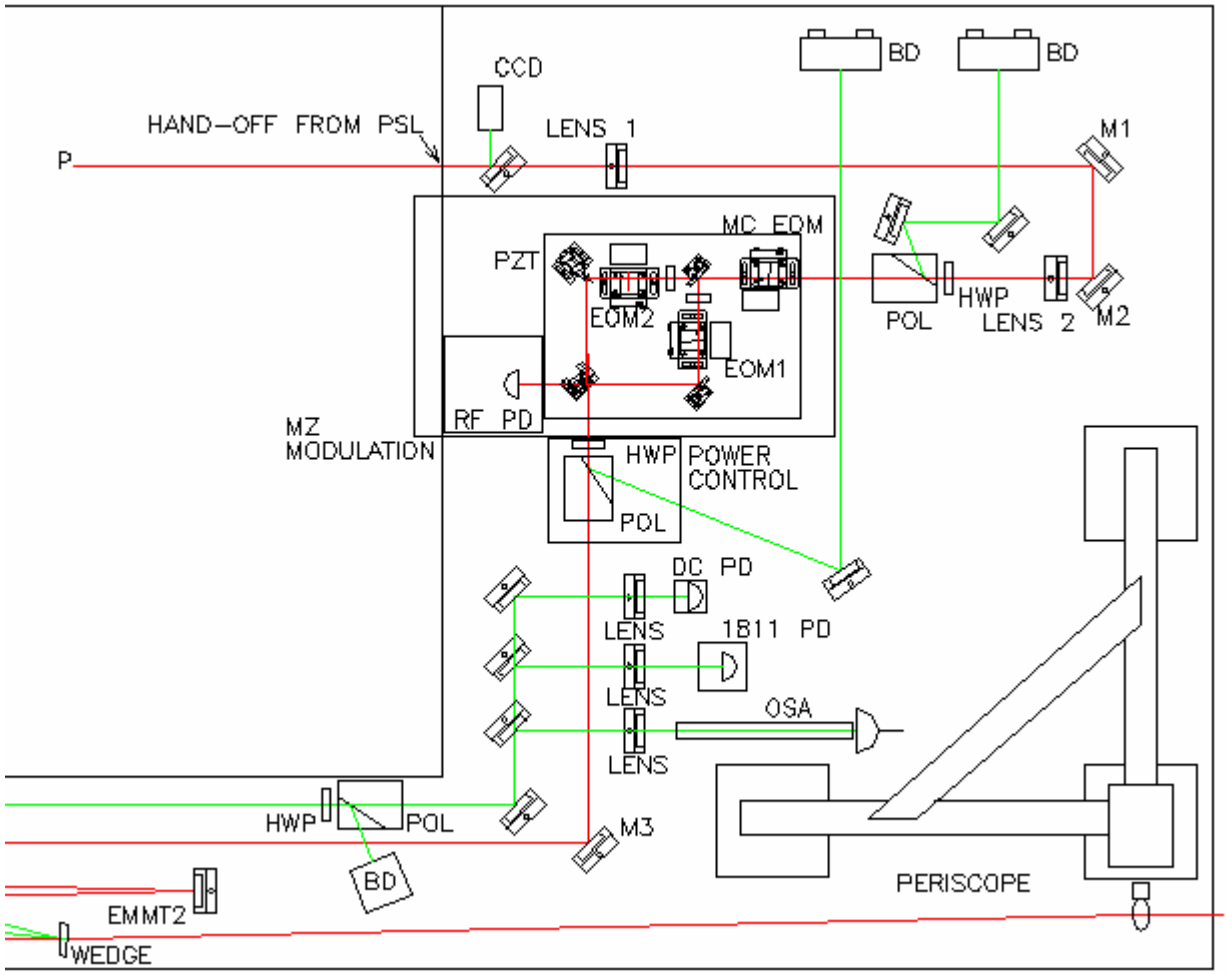

Figure 4.2. Blowup of the main area of the IOO components on the PSL table showing functional blocks of IOO components.

4.2.1 Optical Components

4.2.1.1 General Characteristics

4.2.1.1.1 Optical components

All transmissive optical components (excepting modulators and wave plates) will use fused silica for minimal thermal distortions.

4.2.1.1.2 Kinematic mirror mounts

Newport Ultima®/Suprema® kinematic mounts or Linos Lee's mounts will be used for all in-air mirror mounts in the IOO subsystem.

4.2.1.2 Optical Component Dimensions

Table 2 gives the physical dimensions and clear apertures for the optical components on the IOO table.

Table 2. Summary of PSL table optical component sizes

COMPONENT	*PHYSICAL DIAMETER (MM)*	*CLEAR APERTURE (MM)*	*COMMENTS*
Lens	50	45	
0° beam path mirror	50	45	
45° beam steering mirrors	50	35	
Wave Plate	25	20	
Thin Film Polarizer	50	27.5	Brewster angle
MMT mirrors	50	45	
MZ Beamsplitter	50	35	
MZ active mirror	10	8	Low mass for High Loop Gains for MZ LSC servo

4.2.2 Laser Beam Injection Periscope

At the time of this writing, the injection of the laser beam into the vacuum system is still under discussion, with the possibility of injecting the beam either beneath HAM1,7, above the HAMs, or through HAM1,7. The IOO group has a strong preference for direct injection through HAM1,7. In that case, there are two known periscope designs that can be used. The first periscope is similar to that used in current LIGO.[6] The second option is to modify the design of the tubular ISC periscope. The ISC tubular periscope is significantly shorter than the current LIGO periscope, so a FEA with the actual height needs to be completed to determine the lowest resonant frequency. A major advantage of the tubular periscope is its small footprint.

[6] LIGO drawing D010231-A

4.3 In-vacuum optical layout

4.3.1 Design Considerations

The in-vacuum layout of the IOO components was driven by several considerations:

- IMC length - the requirements on mode cleaner length determine the positions of the suspensions in the HAMS
- Positioning of the MMT mirrors - To be able to achieve the maximum independent adjustability of the mode parameters into the interferometer, we require that the mirror MMT 2 be able to move at least 20 cm forward or back along the HAM3 platform.
- Minimization of coupling of stray magnetic field (*B*) to the suspended IMC mirror actuators - a minimum separation distance of 30 cm between the FI and the suspension is required to reduce the displacement noise induced on the suspended mirror by *B*-field fluctuations to a level below the ambient displacement noise induced by seismic fluctuations.[7]
- Scattered light baffles – A large baffle plate will be located on HAM 3,9 to minimize scattered light coupling between the IOO and COC. The IOO components must not interfere with these baffles and visa versa.

The current state of the layouts is shown in the figures below. Lines representing beams are drawn at the 25 ppm intensity contour.

NOTE: The layouts below assume laser beam injection from HAM 1. Other variations have been discussed (injection from the floor through the bottom of HAM2, injection through side viewports), and both of these options would complicate the layout issues.

4.3.2 Stable Recycling Cavity Layouts

The overall layout and close-ups of HAM2,3 are shown below.

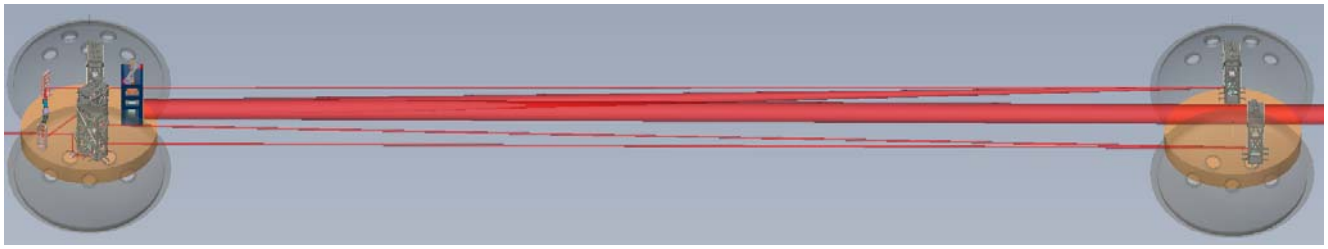

Figure 4.3. Layout drawing of HAM2,3 for the stable power recycling cavity configuration.

[7] LIGO T060025-00-Z, "Analysis of Stray Magnetic Fields from the Advanced LIGO Faraday Isolator", G. Mueller and S. Stepuk

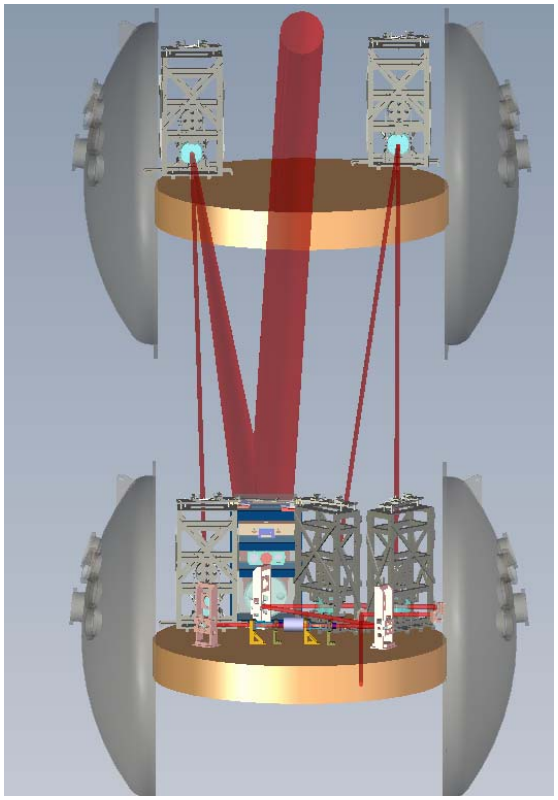

Figure 4.4. Another view of the SPRC layout looking from HAM2 to HAM3.

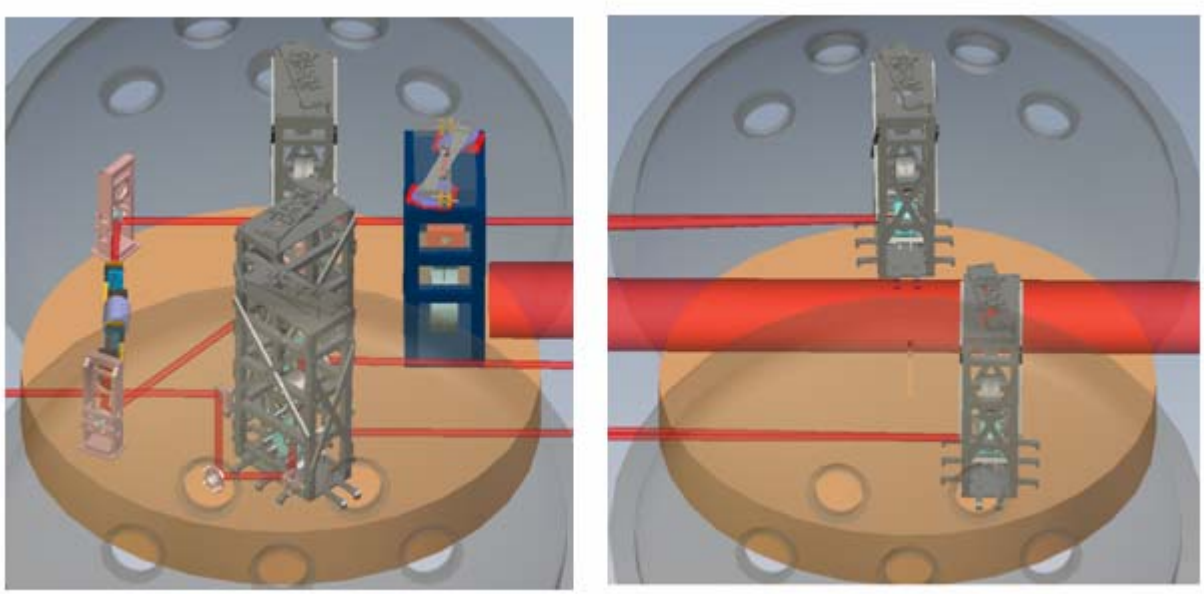

Figure 4.5. Close up views of HAM2 and HAM3 for the SPRC configuration.

4.3.3 Marginally Stable Power Recycling Cavity

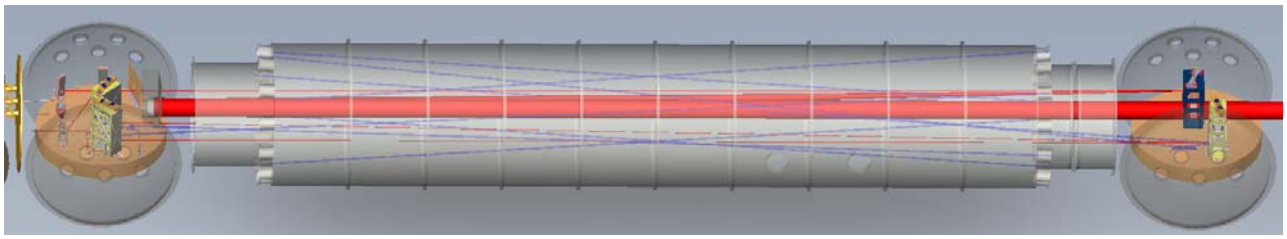

Figure 4.6. Layout drawing of HAM2,3 for the marginally stable power recycling cavity configuration. Red indicates the path of the main laser; optical lever beams are shown in blue.

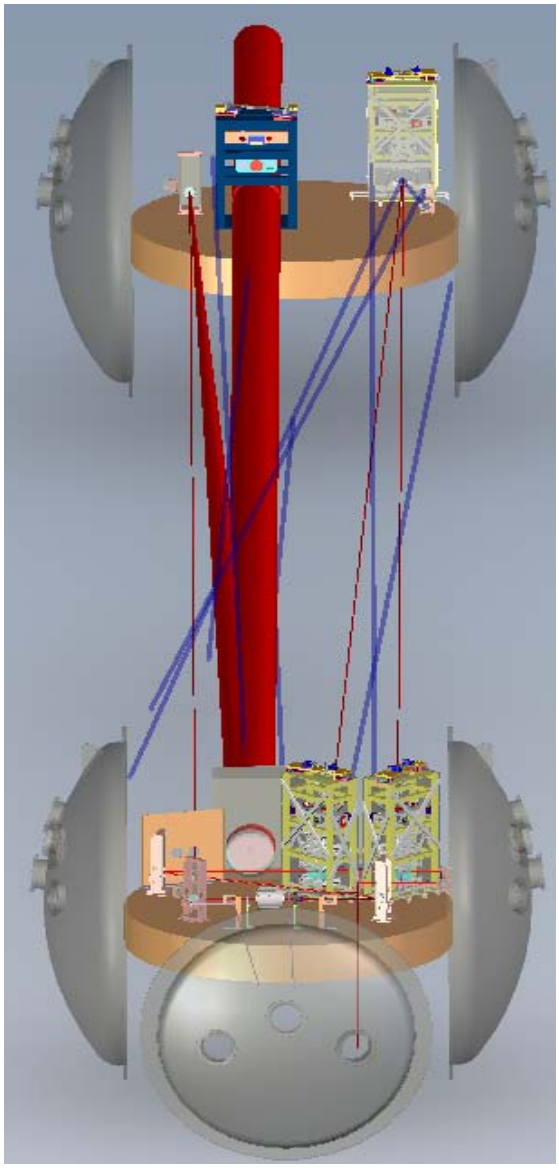

Figure 4.7. Another view of the MSPRC layout looking from HAM2 to HAM3. Red indicates the path of the main laser; optical lever beams are shown in blue.

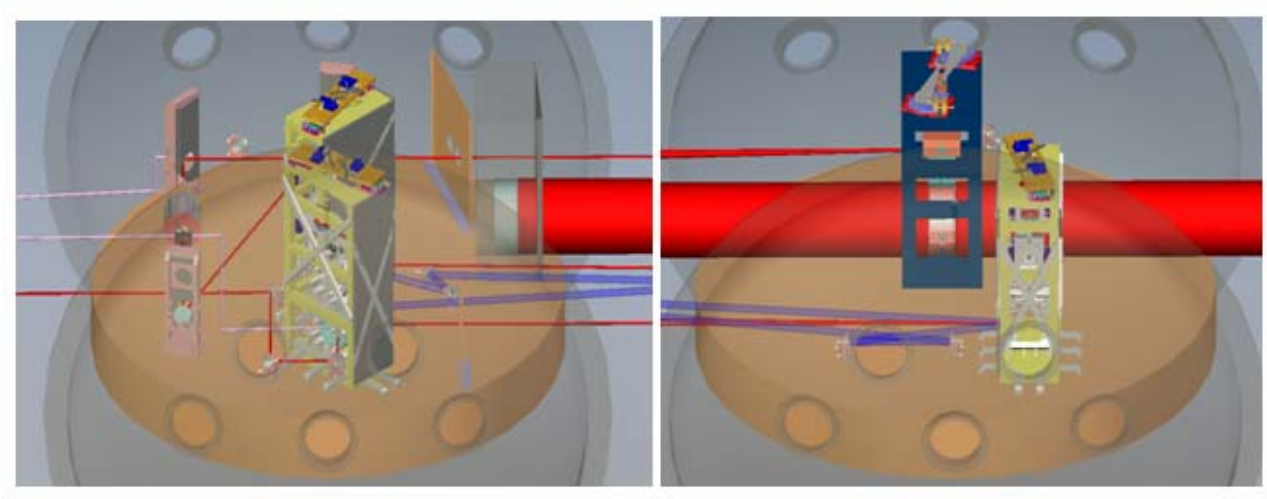

Figure 4.8. Close up views of HAM2 and HAM3 for the MSPRC configuration.

4.4 Baffles

The responsibility for the baffles in the IOO region has recently been moved from AOS to IO. The AOS subsystem has released a conceptual design document (T060263) that includes these baffles, but IOO will create its own scattered/stray light control document that presents these baffles in the context of the IOO subsystem. As such, the baffles of the IOO subsystem will need to undergo a separate review of the scattered/stray light control design, as well as a review of the materials used in the baffles. Here, we report progress from initial research and design on the baffles.

The baffles in the IOO subsection serve two purposes: to prevent errant beams from damaging components inside the vacuum system, and to prevent scattered light noise. The baffles must also survive heating from an intense errant beam (135W, 2mm waist size). The two main design considerations are the material (or materials) and the layout.

4.4.1 Baffle materials

A key choice in the selection of baffle materials is whether they should be absorptive or reflective. Absorptive baffles will create less scattered light noise, but must withstand greater heating. In addition, absorptive baffles can stop an errant beam, while reflective baffles pass the beam to a new location before eventually being absorbed or scattered. Other factors in determining a baffle material are thermal conductivity, maximum operating temperature, machinability, and vacuum compatibility. Candidate materials are copper, aluminum, stainless steel, and silicon carbide. In addition, the materials may be oxidized or coated to change the reflectivity. Initial analysis and tests have shown that even mostly reflective materials become hot when exposed to an intense beam for hours in vacuum. It may be necessary to use scattered light sensors in vacuum to detect an errant beam and automatically attenuate the laser power.

4.4.2 Baffle layouts

Currently there are two concepts for baffling the IOO section. The first is to place the baffles directly on the suspension frames and HAM tables. The second is to mount large baffles on the beam tube between HAMs 2 and 3.[8] Another option is to combine the two approaches.

Baffle apertures have both upper and lower bounds. If the apertures are too large, sensitive components are at greater risk of damage. If they are too small, significant amounts of the main beam will be clipped. The aperture radius of cavity beam baffles (IMC baffles, IMC cleaning baffles) will be set to the 1ppm clipping level, plus 1mm. The aperture radius of non-cavity baffles will be set to the 25 ppm clipping level, plus 1mm.

4.4.3 Suspension and table mounted baffles

All suspension mounted baffles will have fiducial marks to aid visual alignment of the beam onto the mirrors. The figure below shows the locations of suspension and table-mounted baffles. The resonant frequencies of the table mounted baffles will be determined with FEA. Additional structure may be required to raise the resonant frequencies to an acceptable level.

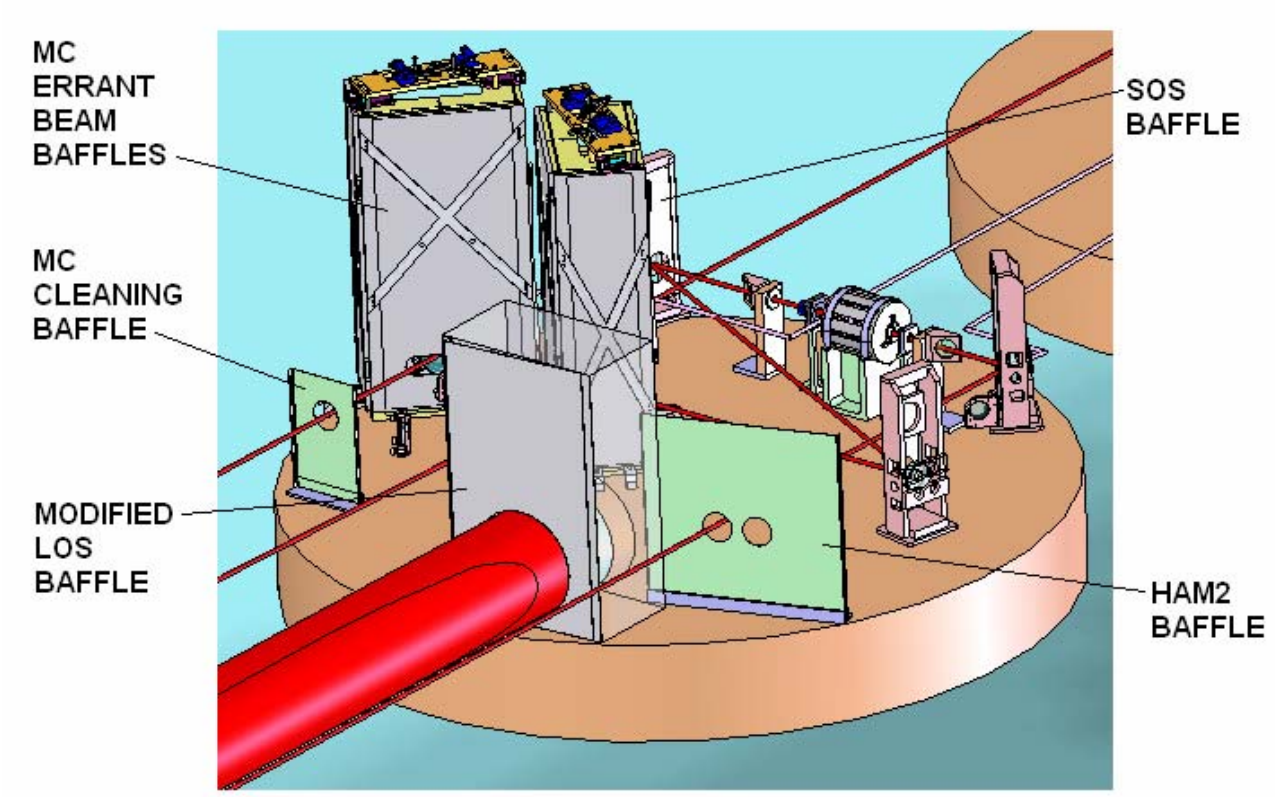

Figure 4.9. Suspension and table mounted baffle locations.

[8] The possibility of mounting a baffle on the vacuum chamber will require an analysis of stray light paths and scattered light noise. This is TBD.

4.4.4 IMC errant beam baffles

The IMC suspensions have baffles that serve two purposes. First, they protect the suspension from errant beams. Second, they provided stiffening to the IMC support structure. They are made from single pieces of material TBD, which are milled to .050" thick in most locations, but are .500" thick in areas where diagonal bracing is needed. These baffles are placed only on the sides of the suspensions that need protection from errant beams.

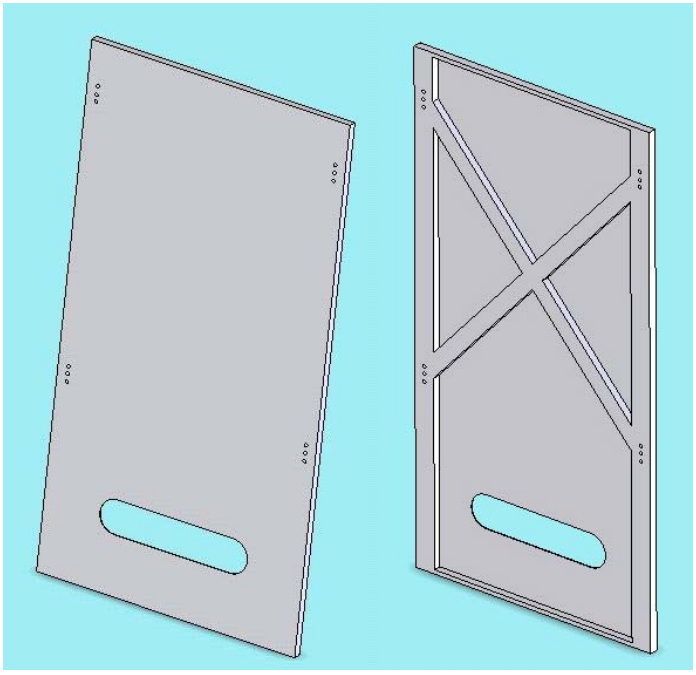

Figure 4.9. IMC front baffle

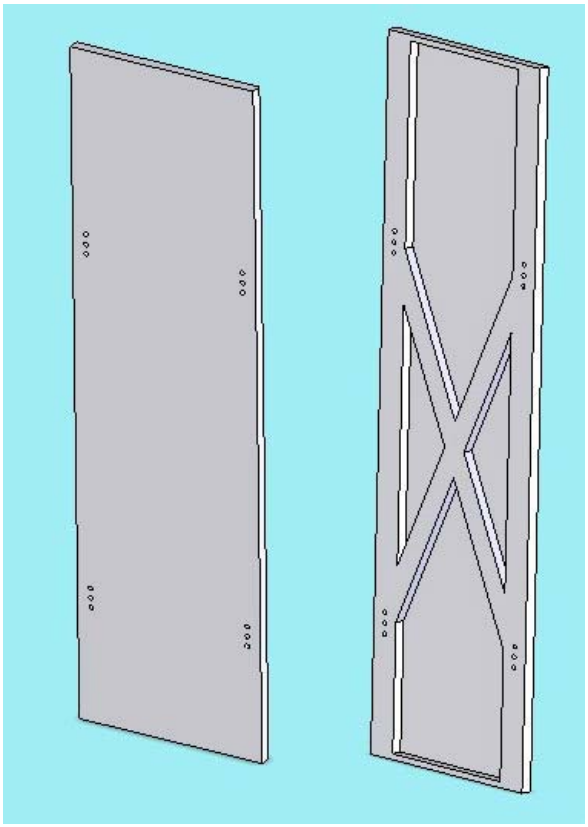

Figure 4.10. IMC side baffle.

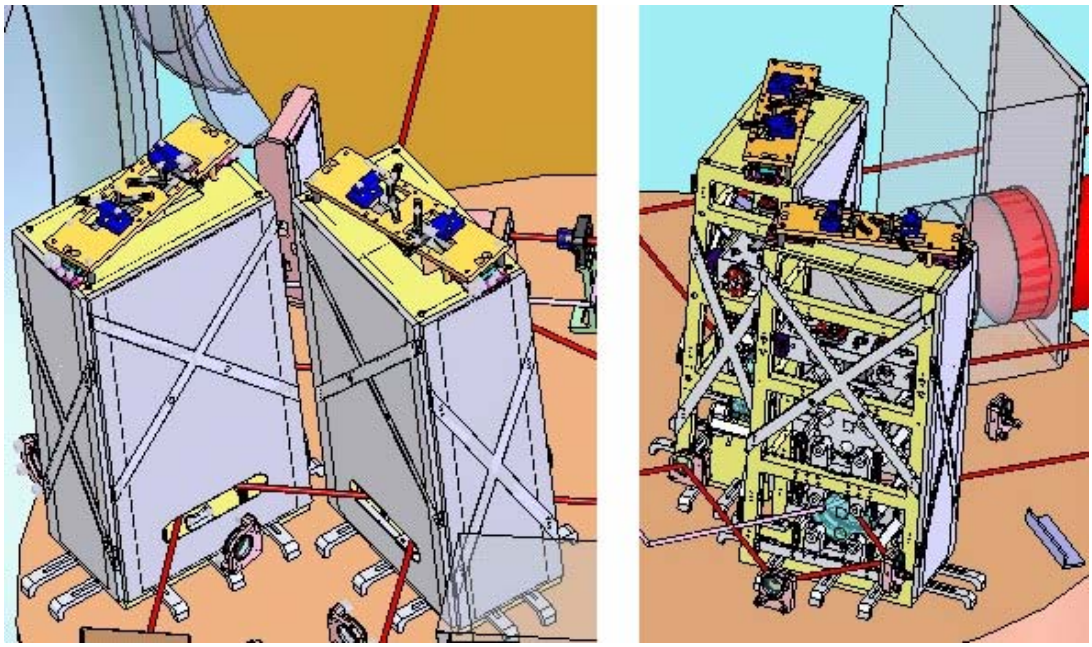

Figure 4.11. IMC1 and IMC3 with baffles.

4.4.5 SOS baffles

The SOS baffles protect the suspensions from errant beams. They are made from either bent (SM1, SM2, MMT2) or flat (MMT1) sheet metal. The baffle on MMT1 is flat because of the large angle of incidence of the beam. Also, the aperture of the MMT1 baffle will be an oval hole rather than a circular one.

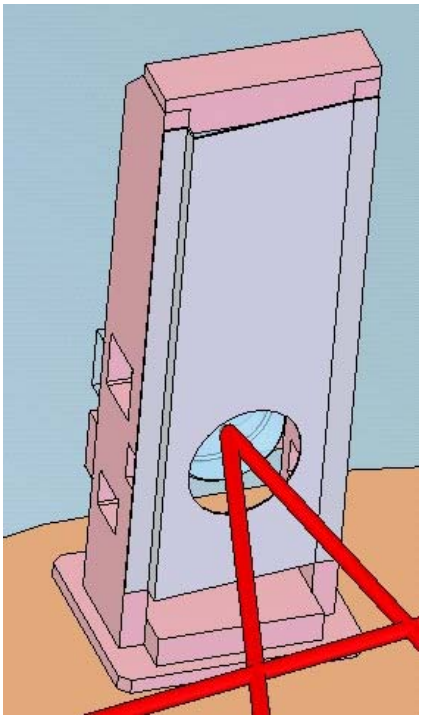

Figure 4.12. SOS baffle for SM1, SM2, and MMT2.

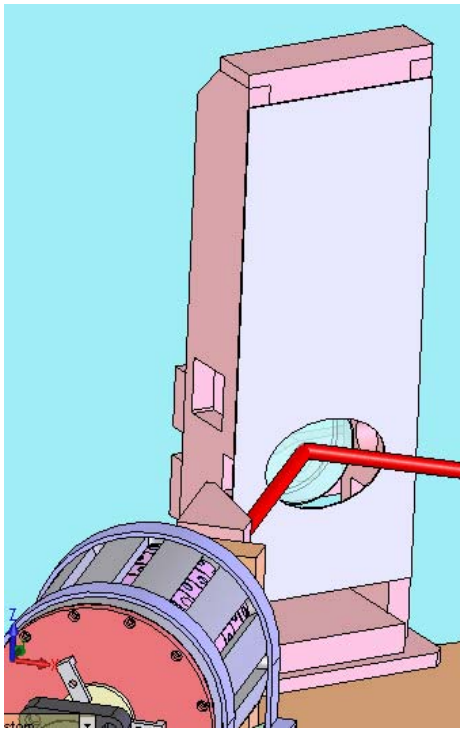

Figure 4.13. SOS baffle for MMT1.

4.4.6 Modified LOS baffle

The modified LOS baffle is used to protect the MMT3 suspension from errant beams. It is similar in design to the bent SOS baffles, just on a larger scale.

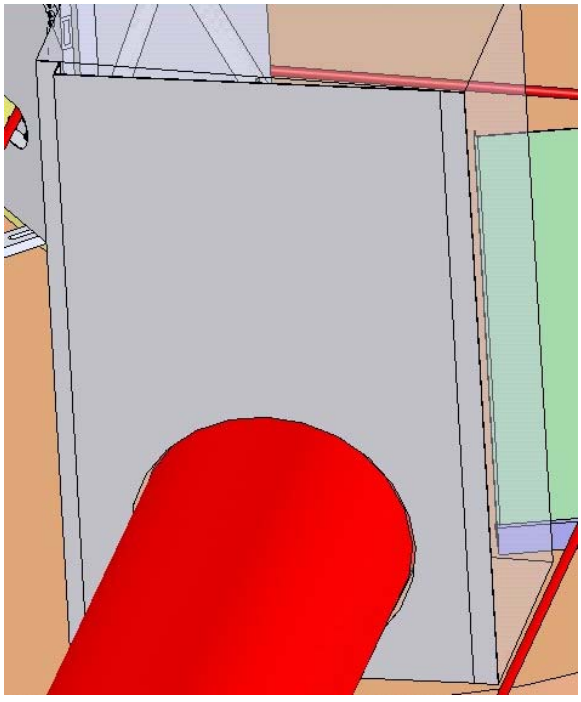

Figure 4.14. Modified LOS baffle.

4.4.7 IMC cleaning baffle

The IMC cleaning baffle is an aperture used to clean scattered light circulating off path in the IMC.

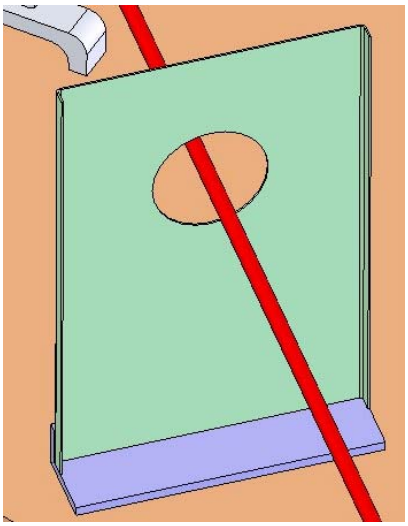

Figure 4.15. IMC cleaning baffle.

4.4.8 HAM 2 baffle

The HAM 2 baffle is used to protect the various wires and electronics in HAM 2 from an errant beam returning from HAM 3. Once the locations and sizes of the wires are determined, this baffle may be replaced with smaller individual baffles at those locations. The second hole in the baffle is to allow a heating beam to pass through, in the event that the MMT2 is heated.

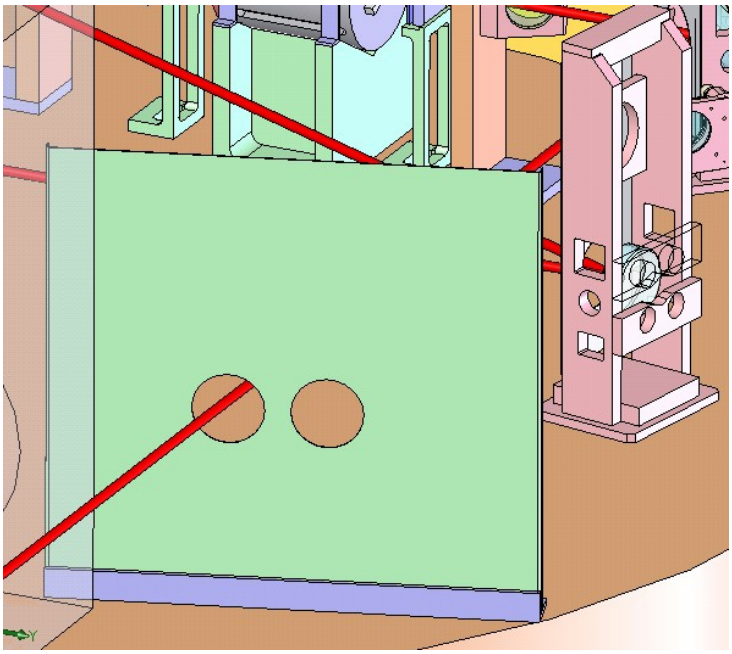

Figure 4.16. HAM 2 baffle.

4.4.9 IO baffle

The IOO baffle is used to separate the IOO section from the COC section. Figure 4.17 shows the basic shape required of the IOO baffle, but it will need to be broken into several pieces in order to allow for changes in the placement of MMT2, and to cover the full beam tube aperture without contacting the ceiling of the HAM chamber. The IOO baffle is the responsibility of AOS, but is presented here because it interfaces closely with IOO components.

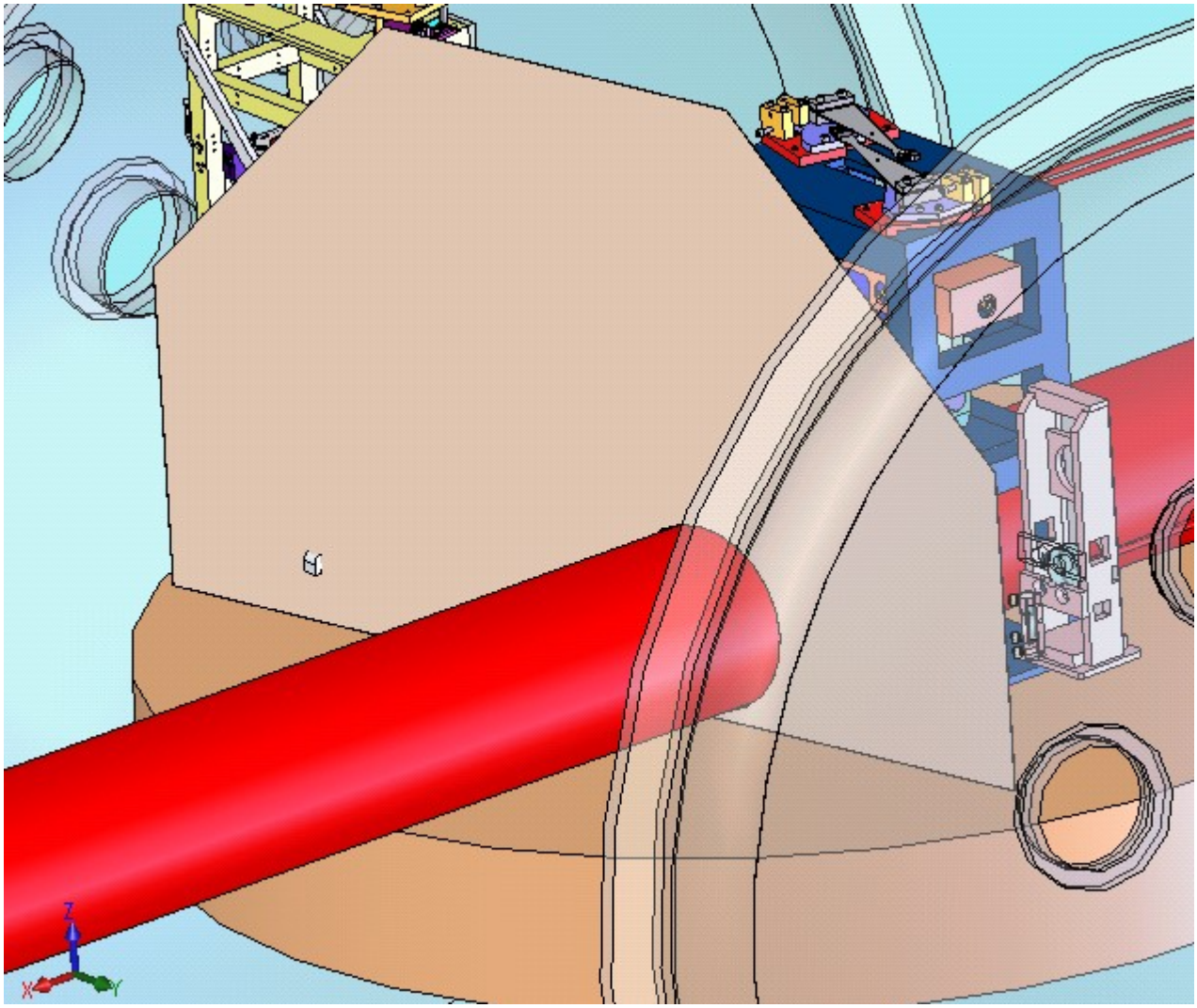

Figure 4.17. IOO baffle.

4.4.10 Beam tube mounted baffles

Beam-tube-mounted baffles have only recently been considered. One advantage to them is that they provide more certainty that no sensitive component can be struck by an errant beam. One disadvantage is that they cannot be mounted on seismic platforms, and hence will have more surface motion, which could increase scattered light noise. Figure 4.18 shows the locations where they could be placed.

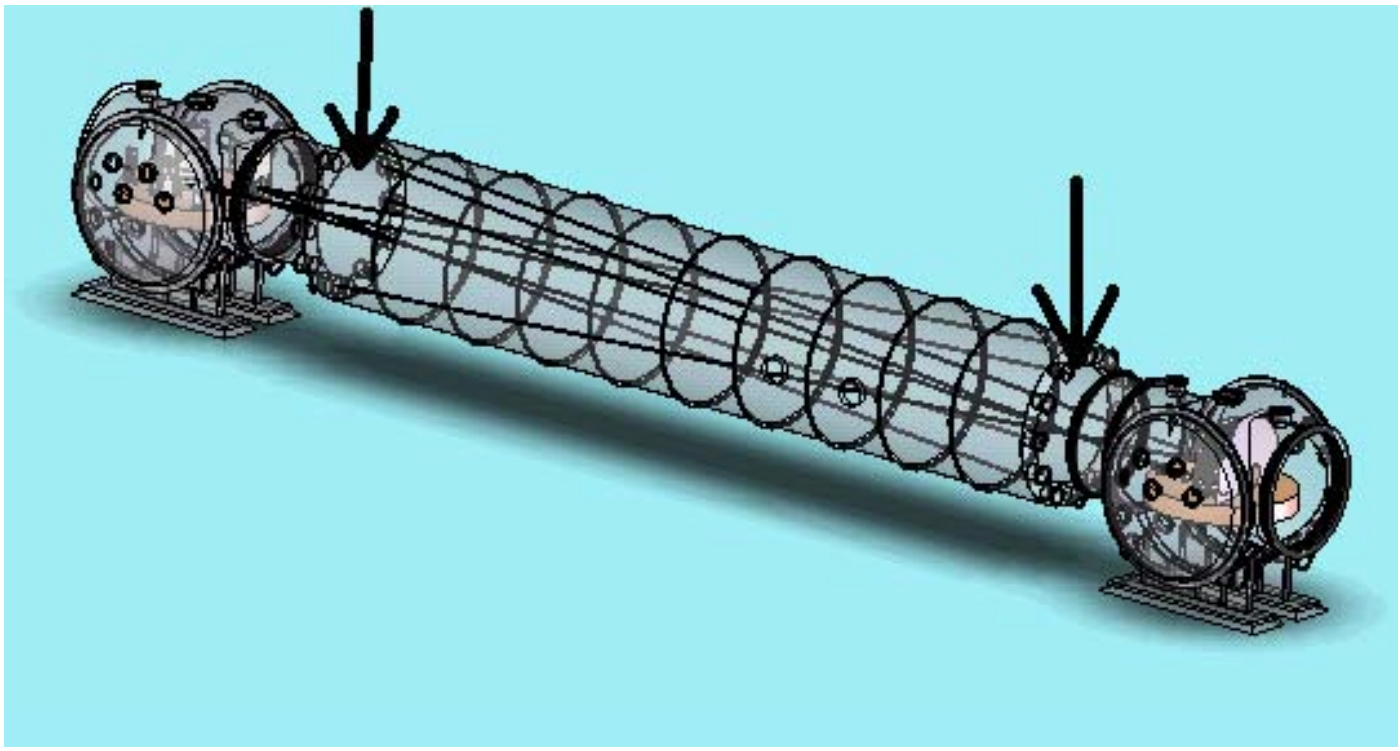

Figure 4.18. Beam tube mounted baffle locations

4.5 Optical levers

All suspended optics will be monitored with optical levers. The routing of the optical lever beams in vacuum is the responsibility of IO. The optical lever transmitters, receivers, and viewports are the responsibility of AOS. The figures below show the current state of the optical lever layout for the MSPRC. Routing for IMC1 and all the SOSs is TBD.

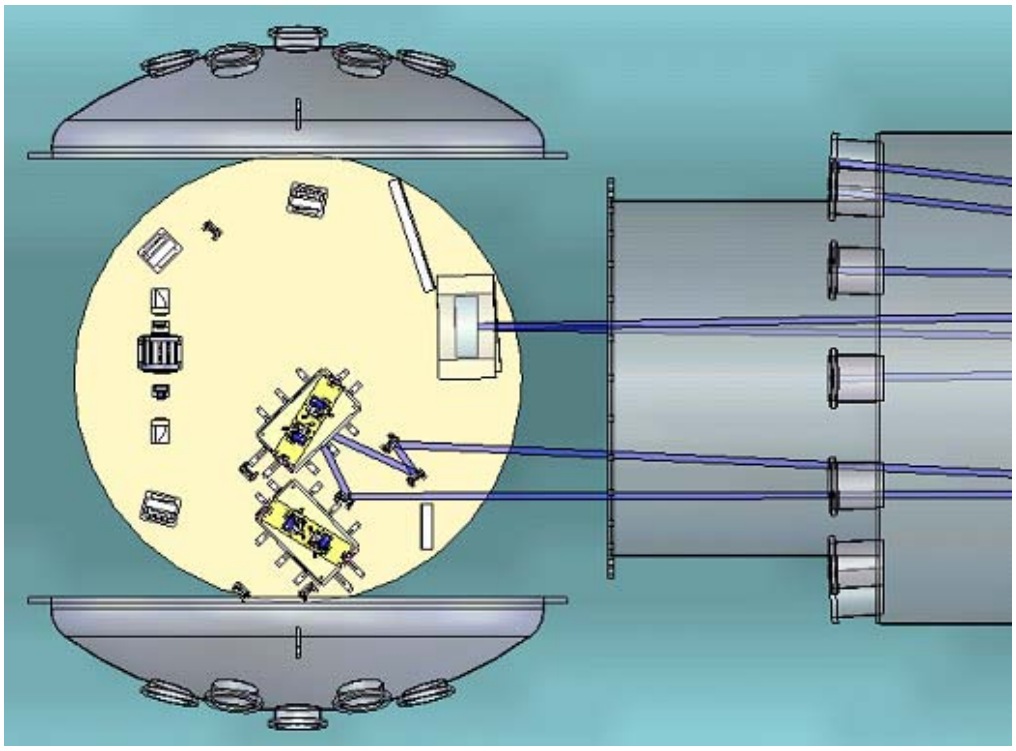

Figure 4.19. HAM 2 optical levers

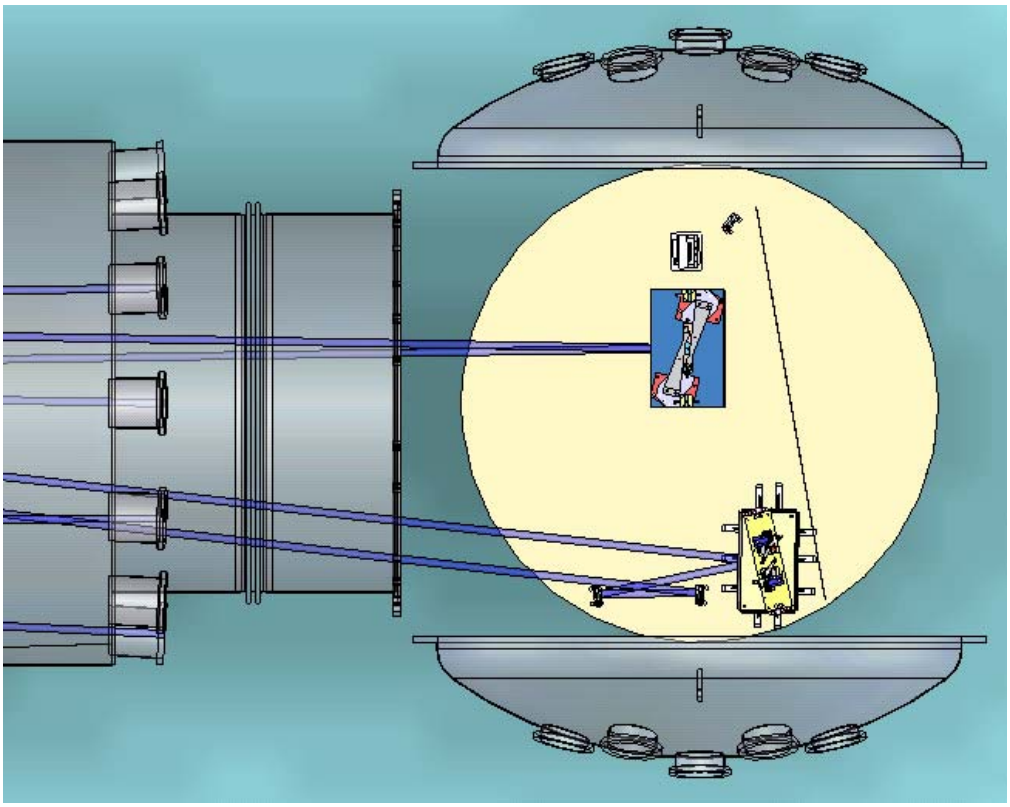

Figure 4.20. HAM 3 optical levers

5 Power Control Subsystem

A power control system similar to that employed in the current LIGO interferometers will provide continuously adjustable variable power into the interferometer without disrupting the interferometer operation. The power control system is not designed to function as an intensity stabilization servo loop system.

5.1 Requirements

The power control system should:

- provide essentially continuous power adjustment into the IMC from ~ 0 W to the maximum available power. The minimum incremental power step should be such that the resultant radiation pressure kick does not knock the IMC out of lock.
- provide an interface to CDS.
- be able to dump the excess light according to the stray light requirements of AdLIGO.

The power control system should not:

- introduce fluctuations in the output power
- unlock the interferometer or IMC undergoing adjustment

5.2 Design

We will use a design similar to that used in initial LIGO based on a polarizer and rotating half wave plate as shown in Figure 5.1.

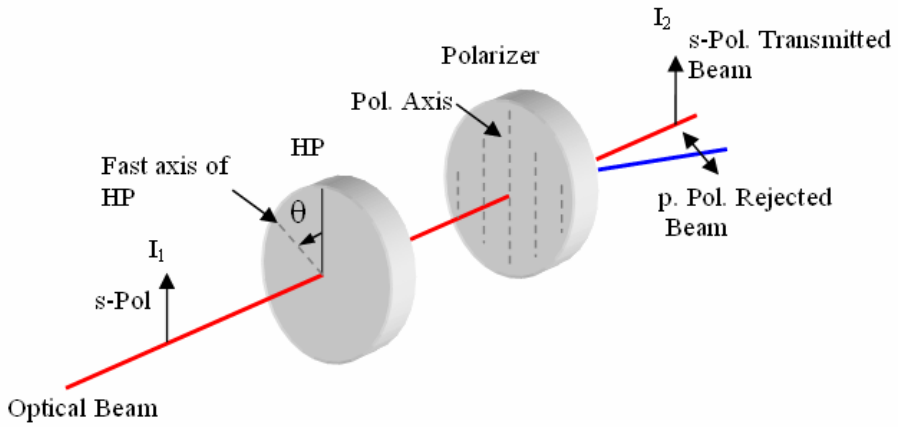

Figure 5.1. Conceptual Design of Power Control System.

The p-polarized IFO optical beam with an intensity of I_1 passes through a HP plate with fast axis at an angle θ with the vertical axis and a TFP with axis along the vertical direction. The s-polarized transmitted light has intensity I_2 while the rejected beam is horizontally ('p') polarized. The relationship is given by Malus's Law:

$$\frac{I_2}{I_1} = \cos^2(2\theta) \qquad \textbf{(5.1)}$$

The full range of power is realized as the HP plate rotates through 0-45^0. LIGO 1 uses New Focus Picomotors to rotate the 1/2 waveplate in 1 dB steps (determined by CDS software). For Advanced LIGO, a motorized rotational stepper stage (Newport URS-100 CC) can provide quasi-continuous rotation of 0.0005^0/step. The corresponding incremental power change as a function of linear step is shown in Figure 5.2

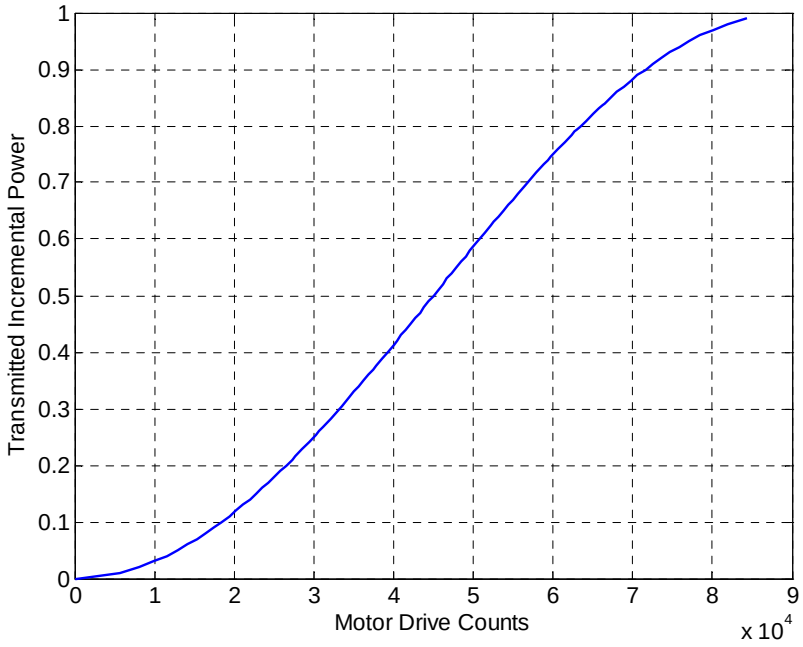

Figure 5.2. Incremental transmitted power as a function of motor drive count to be used to send a control signal to the rotational motorized stage controller. Note that the x-axis is units of 10^4 counts.

5.2.1 Power control adjustment and adjustment speed

An issue with the initial LIGO power control is the limited (1 dB step) amount by which the power can be changed. In advanced LIGO, we plan to provide the operator with the capability of controlling the power ramp speed. At one extreme, the rotational stage is capable of changing power from zero to full load in 5 seconds. This corresponds to about 35 W/second change. At the other extreme, due to the non-linear relationship between the half-wave plate position and the transmitted power, the minimum amount of power change per step can vary from 0.001 mW to 2.1 mW. However, we can obtain uniform changes in power if we adjust the number of steps. The details are dependent upon the software control from CDS. The proposed power control system is flexible enough to incorporate various power ramp-up speeds.

5.2.2 Radiation pressure and IMC displacement

The IMC and IFO mirrors will be subjected to incremental radiation pressure changes as the input power is changed. Since the IMC mirror mass is only 7% of the TM mass, and since the cavity pole of the IFO is much less that of the IMC, and since the IMC stores roughly 1/4 the power of the FP arm cavities, the IMC is most susceptible to radiation pressure kicks.

Power adjustments should occur in such a manner that the incremental 'kick' of the mirrors does not produce longitudinal or angular displacements larger than the bandwidth of the servos used to control the length and alignment.

5.2.2.1 Length Displacement 'Kicks'

The component of force on a mirror from light pressure that induces displacement can be written as:

$$F_{rad} = \frac{2P}{c}\cos\phi \qquad \textbf{(5.2)}$$

where P is the power incident on the mirror, c is speed of light, and ϕ is the angle of incidence of the light on the mirror. Assuming that the cavity is on resonance (i.e., neglecting the correction from the optical spring effect) and the excitation is far above the resonance frequency of the pendulum, the induced longitudinal displacement of a mirror with respect to the cavity axis can be written as:

$$\Delta x_{cav} = \frac{F_{rad}}{\omega^2 M}\frac{1}{\cos\phi} \qquad \textbf{(5.3)}$$

where M is the mirror mass, ω is the angular frequency, and the $\cos\phi$ term accounts for the difference between the displacement and cavity length. For the case of IMC, the $\cos\phi$ terms in the radiation force and the displacement offset each other, and the displacement kicks can be written as:

$$\Delta x_{IMC1,2,3} = \frac{2P_{in}\Im}{c\omega^2\pi M} \qquad \textbf{(5.4)}$$

where P_{in} is the input power and $\Im$ is the finesse of the IMC cavity.

Table 3. Parameter Values for Triple Pendulum IMC Mirror.

Parameter	Unit	Value
P_{in}	W	0-165
IMC Mirror Mass	kg	2.9
$\Im$	-	500
Thickness	cm	7.5

Diameter	cm	15
Angular Frequency	rad/s	$2\pi \times 0.65$

To maintain lock, the radiation pressure kick must be compensated by the IMC LSC. This translates in to a requirement on the slew rate of the servo. For the LSC, we consider the worst case of 82.5 W into the IMC and the maximum power increment at the half power point (HWP set to 22.5^0); this corresponds to an incremental input power change ΔP_{in} = 2.1 mW/step using Eq. 5-1. The radiation pressure kick will be felt by all three IMC mirrors. Thus the total mirror displacement is additive: $\Delta x_{total} = \Delta x_{IMC1} + \Delta x_{IMC2} + \Delta x_{IMC3}$. From Eqs. 5.4, this produces a radiation pressure cavity length displacement Δx_{total} of 131.4 pm/step.

The power build-up time is limited by either the cavity pole filter, $f_{p,IMC}$, or by the speed of the stepper stage. For our design, the maximum speed of the motorized rotational stage limits dP_{in}/dt. Multiplying the displacement/step by steps/s (1778 steps/s for Newport URS-100 CC) produces a maximum IMC mirror velocity of 0.233 pm/μs due to radiation pressure as the power is changed by rotating the HP through the motorized rotational stage. This puts a lower limit on the actuator slew rate. These actuators should be able to move the IMC mirror substantially faster than 0.233 pm/μs. Assuming a safety margin of 10, the MC servo should have a slew rate of better than 0.233 pm/μs.[1]

5.2.2.2 Angle Displacement 'Kicks'

If the beams are not centered on the IMC mirrors, the power increase can cause an angular 'kick' produced by the radiation pressure torque. The torque introduced by an input Power of P_{in} in the IMC that hits a mirror at a distance, d, away from the center and the restoring torque is given by:

$$T = \frac{2P_{in}\Re d}{c\pi} = \alpha\Theta\omega^2. \qquad \textbf{(5.5)}$$

where α is the angle, Θ is the angular moment and ω is the angular frequency in yaw. Simplifying Eqs.(5.4) and (5.5) for α:

$$\alpha = \frac{2P_{in}\Im d}{c\pi\Theta\omega^2}, \qquad \textbf{(5.6)}$$

where Θ along the orthogonal directions to the beam propagation various directions is given by $\Theta_{xx} = \Theta_{yy} = \frac{1}{4}MR^2 + \frac{1}{12}Mh^2$. Here M is the mass, R is the radius, and h is the thickness of the mirror as given in Table 3. Assuming the maximum allowed decentering of 1 mm[9] on the IMC mirror, the angular 'kick' is equal to 0.077 nrad/step at the half power point. Multiplying the nrad/step by the transfer function of the rotational stage, i.e., 1778 step/s gives 0.137 prad/μs.

[9] Advanced LIGO Input Optics Preliminary Design Document, LIGO T-020020-02-D

Considering that there are three mirrors and assuming a safety margin of 10, a minimum of 4.2 prad/μs slew rate should be available from the IMC ASC servo loop.

5.2.2.3 CDS Control of the Input Power

Should it be found during commissioning that incremental radiation pressure due the power control system causes unforeseen problems in the interferometer, the slew rate of the power can easily be (and should be) limited in software. This will be easy to do with stepper motor control

5.3 Beam Dump

The rejected beam in the power control system must be disposed of properly. Although there is no formal requirement, the rejected beam (as much as 180 W) should be dumped with minimal back-scatter. For beam dumps, the IOO base line design is commercially available water cooled beam dumps from Kentek (ABD-2C). The quoted specular reflectance of these beam dumps is less than 0.1%.

To verify this, we have measured the scattering of laser radiation from the commercial beam dump at 100 W input powers. The total scattered power into 2π steradian (half hemisphere) was measured to be 7.6 mW using a calibrated Ophir power meter. The measurements as a function of angle from the normal to the surface of the beam dump at a distance of 18.5 cm away from the surface are shown in Figure 5.3. A 4th degree polynomial is fitted using least squares technique and the result is integrated into 2π steradian (half hemisphere). The total power radiated into half hemisphere is found to be ≈ 10 mW.

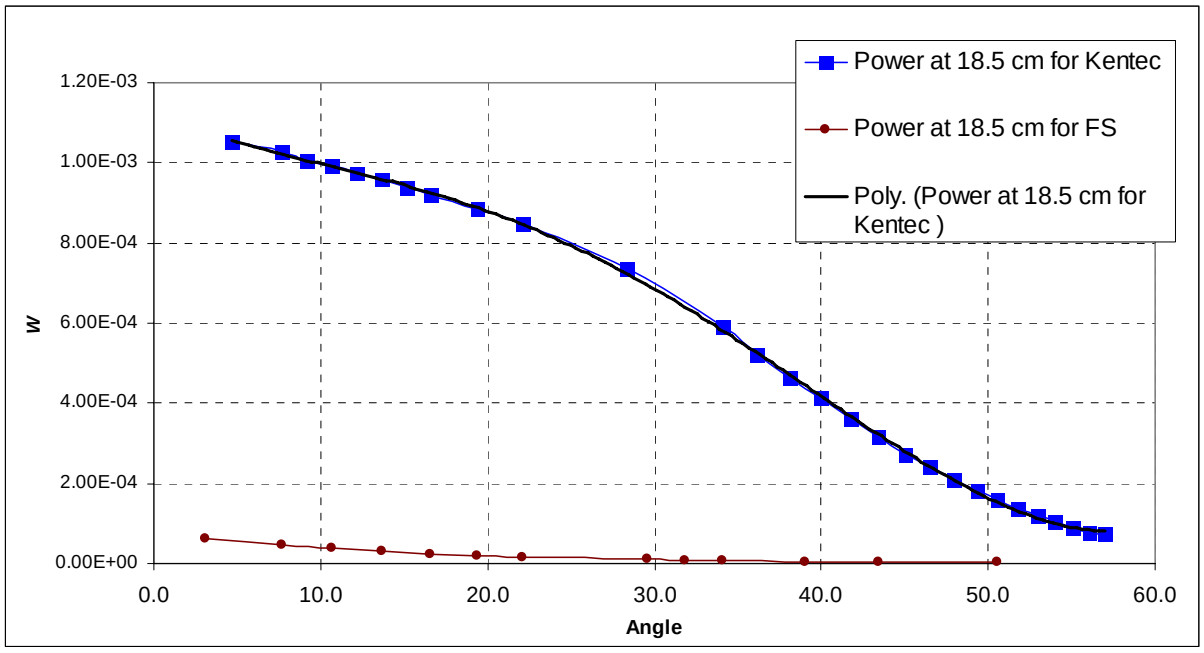

Figure 5.3. Power in W measured at a detector of 1 cm^2 area placed at 18.5 cm from the beam dump as a function of angle from the normal to the beam dump. The blue squares are experimentally measured powers for the Kentek beam dump; the red circles are experimentally measured powers from a home-made beam dump described in the Appendix.

6 RF Modulation

6.1 Introduction

RF modulation is needed to sense and control the interferometer length and alignment DOFs. Three modulation frequencies are needed, one to lock the mode cleaner and two other frequencies to extract control signals of the main interferometer (including Michelson, power recycling cavity, signal recycling cavity and arm cavities). The IOO must produce and monitor these sidebands using RF signals from the ISC.

Specifically, the IOO provides:

- the design, fabrication, and assembly of all RF electro-optic modulators for the production of sidebands for controlling the interferometer and mode cleaner length and alignment sensing systems;
- a 'clean' sideband spectrum. The modulation must avoid the sidebands on sidebands problem[10] for the interferometer's central part control signals (either by using a Mach-Zehnder setup or a complex modulation scheme);
- ancillary optical and mechanical components.

6.2 Baseline Design

AdvLIGO uses the same vacuum chambers as the current LIGO interferometer, thus constraining cavity lengths. The IMC FSR is set by its length to ~9 MHz. In order to pass through the IMC, the IFO control modulation frequencies must satisfy:

$$f_{mc} = n\frac{c}{2L_{mc}}$$

The modulation frequencies for the core interferometer are TBD but the current modulation schemes [6] favor either 9 MHz/108 MHz allowing still the resonant readout scheme[11] or 27 MHz/45 MHz. When choosing the exact values of the modulation frequencies it is paramount that they all miss the harmonics of the 4 km arm cavity free spectral range of 37.5 kHz.

The modulation frequency to be used to lock the mode cleaner is not transmitted (heavily attenuated by the IMC) and can be considered non-critical as long as overlap with the modulation frequencies for the core interferometer is avoided. We choose a value of **31.457 MHz** (**TBR IO**), for the IMC locking, about 100 kHz off the fourth antiresonance (n = 3.5).

[10]LIGO–T040119–00–R, "Mach-Zehnder interferometer for Advanced LIGO optical configurations to eliminate sidebands of sidebands," O. Miyakawa, et al.

[11] The upper modulation frequency is constrained by the space in the vacuum chambers that limits the maximum asymmetry in the Michelson arm length to $\Delta l < 75$ cm.

6.3 Constraints

The constraints on the modulation frequencies are mainly given by the vacuum system. The mode cleaner and recycling cavities span vacuum chambers whose separations determine the various cavity lengths.

6.4 RF modulation requirements

The requirements on optical modulation, including modulation depths, and relative stability of the modulation frequency and amplitude, for Advanced LIGO are described in the IOO DRD, LIGO-T020020 and also EO-Modulators for Advanced LIGO, Part I, LIGO- T020025-00-D.

A more recent investigation was done in the LIGO-T060267-00-D document "Upgrading the Input Optics for High Power Operation". Refer to this document for technical details of the modulator. Changes in the design/performance the AdvLIGO modulators from those ELIGO modulators are discussed in this document.

6.4.1 Modulation frequencies

The final values for the modulation frequencies are **TBD ISC**; nominal values are 9 and 45 MHz. Section 7.2.3 discusses the constraints on the modulation frequencies imposed by the existing physical locations of the HAM and BSC chambers.

6.4.2 Modulation depths

Modulation depths are set by GW shot noise considerations at the asymmetric port. In addition, the IOO must provide for a range of modulations about the specified depths to accommodate diagnostic functions and potential degradation.

- The IOO must provide for modulation depths in the range m = 0-0.8.

6.5 Modulator design

We have made prototype RTP-based phase modulators using 1.5 cm long x 0.4 cm width x 0.4 cm thickness crystals. A preliminary design is given in LIGO-T060267-00-D document "Upgrading the Input Optics for High Power Operation".

6.5.1 Mechanical design

The modulator is enclosed in an industry-standard housing, providing multiple apertures to guarantee that the high power laser beam comes in contact only with the crystal and not the electrodes (thus preventing catastrophic damage). The housing will be manufactured by UF. The crystal housing does not include the resonant circuit and impedance matching network.

6.5.2 Impedance matching

The impedance matching circuit is placed in a separate housing to easily change resonant frequencies without the need to access the sensitive crystal. Figure 6.1 shows the equivalent circuit of the impedance matching network. The matching circuit is designed to have an input impedance of 50 Ω and at resonance to increase the RF voltage at the crystal by Q, the quality factor of the

resonator.

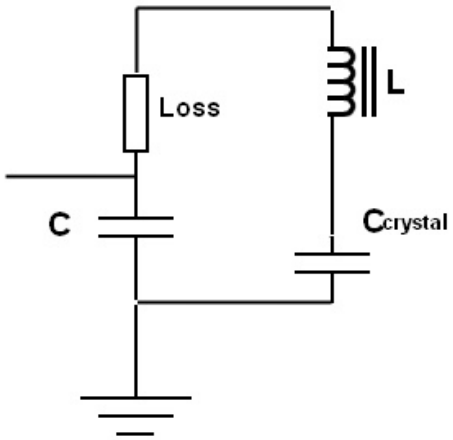

Figure 6.1. Equivalent circuit of the resonant circuit / impedance matching network.

Based on earlier ISC requirements, we have made and tested matching networks for f = 19.7 MHz and 180 MHz. The crystal has capacitance C = 6 pF and the impedance associated with the electrodes and the electrical wiring is about 2 Ω. The shunt capacitance is in the 20 pf range. The 19.7 MHz circuit had Q = 20 while the 180 MHz circuit had Q = 3.

6.5.3 Temperature stabilization

If future tests, or the experiences with the eLIGO modulators, show the need for an active temperature stabilization of the modulator crystal, we are prepared to implement this. The temperature can be measured with standard low voltage temperature sensors like the TMP35/36/37 which has a sensitivity of 10mV/K. The temperature would be stabilized by feeding the error signal to Peltier elements that control the temperature of the modulator housing, using linear temperature-controller circuitry.

6.5.4 Damage testing and thermal lensing

Results of damage testing and thermal lensing are given in "Upgrading the Input Optics for High Power Operation", LIGO-T060267-00-D, and "Modulators and Isolators for Advanced LIGO", LIGO-G060361-00-D.

6.6 Avoiding Sidebands on Sidebands

Currently, three techniques are known to circumvent the sidebands on sidebands problem[12] that arises when phase modulators are used in series to impose modulation sidebands. The baseline design is to split the beam using a Mach-Zehnder interferometer and apply the modulations in different arms. We will concentrate on this in the first part of the following section. An alternate

[12] LIGO–T040119–00–R, "Mach-Zehnder interferometer for Advanced LIGO optical configurations to eliminate sidebands of sidebands," O. Miyakawa, et al.

solution to this problem, pursued by our group as a research project, is *complex modulation*, which can synthesize arbitrary modulation signals. This is described in a separate document.[13] In addition, it is possible to use two-phase locked lasers to generation a frequency-shifted sub-carrier, however we are not actively exploring this as it falls outside of the IOO scope.

Our approach to the design of the AdvLIGO MZ modulation method was informed by discussions with the 40 m team. We learned that:

- The 40 m MZ was not monolithic, but mounted directly to the optical table using standard methods
- In the initial 40 m MZ design, there was no shielding from environmental effects (e.g., air currents, temperature drifts)
- The length control servo relied solely on a mirror-mounted on a PZT, thus had low bandwidth.

The design below addresses these issues.

6.6.1 Parallel (Mach-Zehnder) modulation

The parallel phase modulation was first tested in an interferometer at Caltech's 40 m prototype.[14] This technique entails splitting the laser light with a beam splitter, modulating the transmitted and reflected beams with two different frequencies, and then recombining the light with a second beamsplitter, as shown in Figure 6.2. This configuration is commonly called a Mach-Zehnder (MZ) interferometer.

Although the MZ method avoids the generation of sidebands on sidebands, it creates some other complications:

- An additional servo loop to control MZ differential arm length
- Overdriving the EOMs to achieve the required modulation index
- Possible introduction of excess intensity, frequency and sideband noises
- Additional intensity modulation (noise) at modulation and mixing (sum/difference) frequencies

As an interferometric method is used to recombine the beams, it is necessary to control the differential length arm to keep the output port constructive for the carrier. It is also necessary to keep both arms equal lengths on a macroscopic scale to achieve a good beam overlap and therefore a good visibility.

---

[13] LIGO-T07 T070197-00-D, "Complex Modulation", http://lsc-grid.phys.ufl.edu/ligo-uf/PDR/complex_modulation.doc

[14] LIGO–T040161–00–R, "Effect of Mach Zehnder Residual Displacement Noise on the 40m Detuned RSE Interferometer, S. Kawamura and O. Miyakawa.

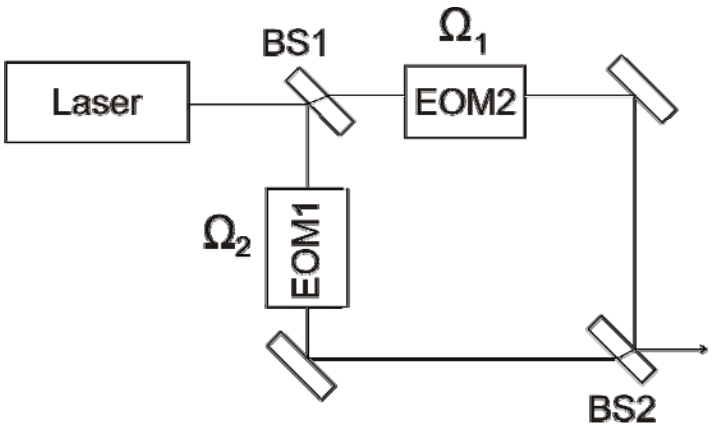

Figure 6.2. Parallel modulation using a Mach-Zehnder interferometer.

Assuming 50/50 beamsplitters for the input and output ports, only half of the light is modulated with each modulation frequency and then half of the modulation is lost at the combining beam splitter, reducing the effective modulation index 4X.[15] The recombined light is constructed from two physically distinct optical paths, thus environmental noise can lead to additional intensity, phase or pointing (beam position) noise. Finally phase modulation directly couples into intensity modulation at the second harmonic if the interferometer is kept on the bright fringe and might even leak into the fundamental if the length is not perfectly kept on the bright fringe.

6.6.2 Noise coupling / estimates

The recombined light emerging from the MZ interferometer may exhibit noisiness in its amplitude, phase, or pointing. These noise terms will not be common to all frequency components, a situation distinct from noise found in serial modulation. The noise is the result of mirror motions or index of refraction changes that may be either common or differential between the two Mach-Zehnder arms, or even between mirrors within a single arm. The mirror motions, in turn, may be either angular or longitudinal, and non-normal angles of incidence on mirrors or beams not centered on the optics will mix the effects.

The laser field exiting the MZ is given by:

$$\frac{E_0}{2} e^{i\omega t} e^{ik\bar{L}} \left(e^{ik\Delta L} e^{im_1 \sin(\Omega_1 t)} + e^{-ik\Delta L} e^{im_2 \sin(\Omega_2 t)} \right) + c.c. \qquad \textbf{(6.1)}$$

Where Ω_1 and Ω_2 are the modulator frequencies, and m_1 and m_2 are the modulation depths of the two EOMs. We also define the common and differential MZ lengths to:

$$\bar{L} = \frac{L_1 + L_2}{2} \quad , \quad \Delta L = \frac{L_1 - L_2}{2} \; . \qquad \textbf{(6.2)}$$

[15] In the event that one modulation frequency dominates, the BS ratios can be adjusted to allow for increased power in one arm

with the L_i denoting the length of the two MZ arms.

6.6.2.1 Longitudinal common motion

Longitudinal common motion, when $\bar{L}$ causes phase noise (or noise frequency sidebands) common to carrier and radio-frequency sidebands, is the same as noise produced by vibrating serial modulation components. Because this is a familiar variety of noise, we expect to be able to combat it with existing techniques. This is accomplished with laser frequency monitoring and feedback through the mode-cleaner, which in turn is locked to the common mode of the long arm cavities.

6.6.2.2 Longitudinal differential motion

When the lengths of the MZ arms change differentially $\Delta L \rightarrow \Delta L(t)$, two noise effects occur. The amplitude of the recombined carrier varies, and relative phase noise develops between recombined carrier and the sidebands.

6.6.2.2.1 Sideband-carrier relative phase noise

With the current Advanced LIGO design, noise in the relative phase between carrier and sideband light can end up as laser frequency noise. As mentioned, the laser's frequency is locked to the mode cleaner, which in turn is locked to the common-mode of the arm cavities. The arm cavity common-mode error signal S will (most probably) be measured in the beat between carrier and the one of the sidebands. In this scheme, relative phase noise is indistinguishable from laser frequency noise, feeding back a corrective signal that will impose noise on the laser. The limit on laser frequency noise has been established for Advanced LIGO[16], see Figure 6.3.

To translate this into a limit on differential motion of the Mach-Zehnder arms, we compare the transfer functions of sideband-carrier relative phase to the arm cavity common-mode error signal and the frequency noise transfer function. Given a frequency noise limit $\Delta f(f)$, the relative phase noise limit $\Delta\Phi(f)$ is

$$\Delta\Phi(f) = \frac{\partial S/\partial f}{\partial S/\partial \Phi}\Delta f(f).$$

Here S is the arm cavities' common-mode error signal.

We find the relative phase noise transfer function with a FINESSE model of the full Mach-Zehnder-enhanced dual-recycled interferometer. This noise analysis uses the current baseline parameters of the locking scheme and assumes that 9 MHz sideband is used to generate the error signal. The same simulation is used to calculate the transfer function of frequency noise. Combining both transfer functions allows us to estimate the maximum allowed phase and therefore displacement noise in the differential arm length. The result is presented in Figure 6.4.

(Once the locking scheme is finalized this investigation has to be repeated to verify the final requirements for the *Sideband-carrier relative phase noise*.)

[16] P. Fritschel, "Advanced LIGO Systems Design Report No. LIGO-T-010075-00-D", LSC Conference 2001.

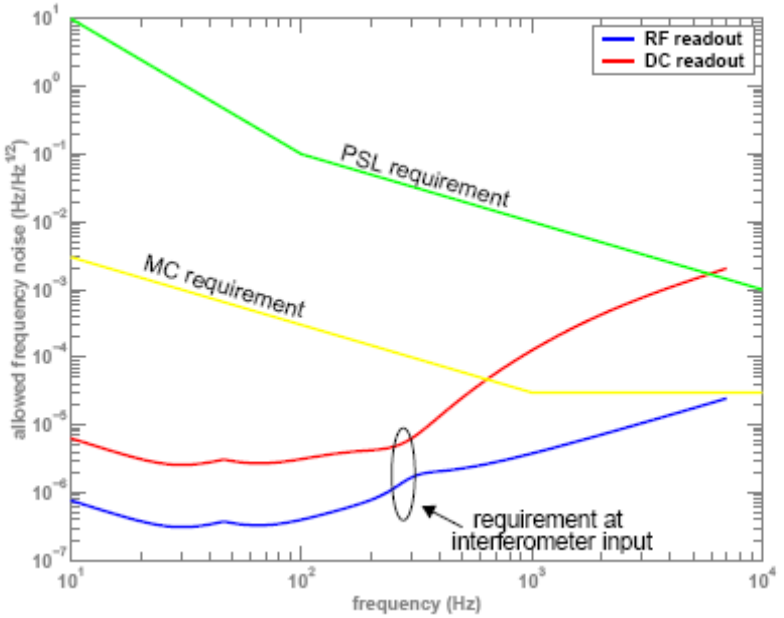

Figure 6.3. AdvLIGO frequency stability requirements

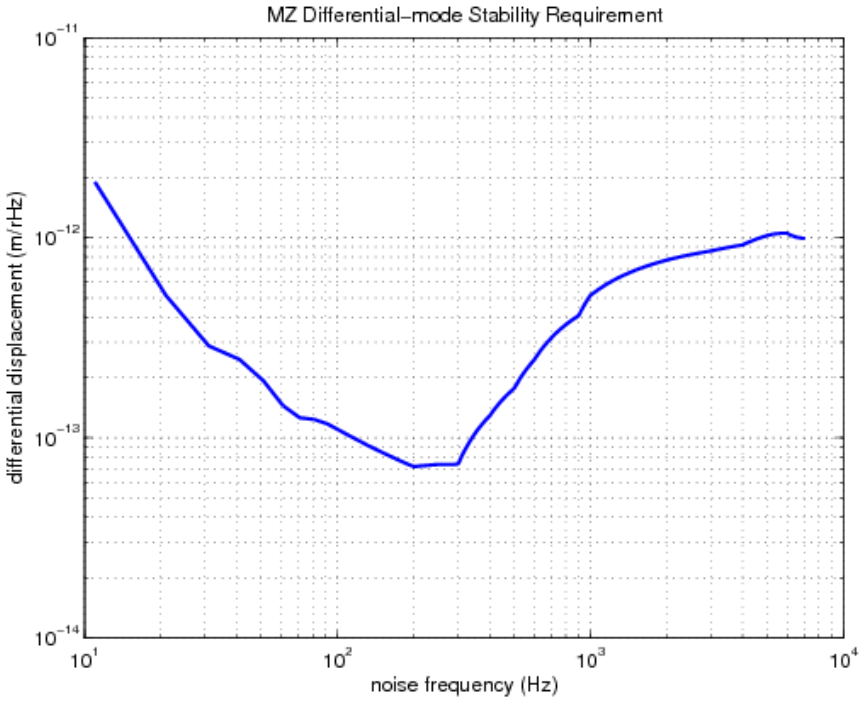

Figure 6.4. Stability requirement for MZ differential mode

6.6.2.2.2 Sideband amplitude noise

The intensity stabilization servo (ISS) after the IMC will make noise in the amplitude of the recombined carrier and the generated sidebands look like noise in the modulation depth.

A limit on Mach-Zehnder differential arm length motion due to sideband amplitude noise is hard to establish but we can quantify the amount of change in the sideband amplitude as a function of the differential length ΔL. The intensity is stabilized to I_0, meaning the following expression can be assumed to be true for all ΔL.

$$I_0 = \frac{I(\Delta L)\cdot 2}{1+\cos(2k\Delta L)} \quad . \qquad \textbf{(6.3)}$$

Solving this for the intensity before the MZ (assuming small ΔL) gives:

$$I(\Delta L) = \frac{I_0}{2}[1+\cos(2k\Delta L)] \approx I_0(1+(k\Delta L)^2) \quad . \qquad \textbf{(6.4)}$$

To first order in $\delta L(f,)$ this directly translates into the apparent relative intensity of the carrier and the sidebands to:

$$RIN(f) = k^2 \Delta L_{RMS}\, \delta L(f) = 4\pi^2 \frac{\Delta L_{RMS}}{\lambda}\frac{\delta L(f)}{\lambda} \qquad \textbf{(6.5)}$$

where ΔL_{RMS} is the fringe offset. Assuming a conservative value of ΔL_{RMS} = 10 nm, this leads to a sideband relative intensity noise $RIN_{sb} \approx 3.5\times 10^{-8}$.

6.6.2.3 Angular mirror motion effects

When mirrors have angular fluctuations, a disparity arises between the optical axes of the Mach-Zehnder IFO and the IMC. Small displacements δ or tilts θ in the recombined beam after the MZ, when expanded in the IMC basis set, will contain small contributions from higher-order Gaussian modes. As the magnitude of the δ or θ mode changes is determined by the differential displacement noise the changes of δ or θ are in the $10^{-13}\frac{\mathrm{m}}{\sqrt{\mathrm{Hz}}}$ or $10^{-13}\frac{\mathrm{rad}}{\sqrt{\mathrm{Hz}}}$ regime (assuming ~1 m long arms) and thus fairly small compared to the waist of the beam and thus the *extra intensity noise* after the IMC will be easily suppressed.

6.6.3 Experimental realization

To investigate the noise properties and potential problems of the parallel modulation scheme, a table-top prototype compact and quasi monolithic Mach-Zehnder interferometer was built. All optics were mounted using small mirror mounts near the plate avoiding long lever arms and hereby reducing potential low frequency resonances. Figure 6.5 shows the schematic realization of the experiment. To allow differential arm length control with a high dynamic range, a small 10.0 mm diameter, 2.0 mm thick HR mirror is attached to a PZT actuator which allows tuning the differential arm length with only 2 V per wavelength. The small mirror creates a resonance of about 13 kHz with the PZT. No high voltage amplifiers are needed to compensate for thermal drifts and

the PZT as well as the EOM are driven directly from a low-noise op amp. The servo description can be found at the end of this section.

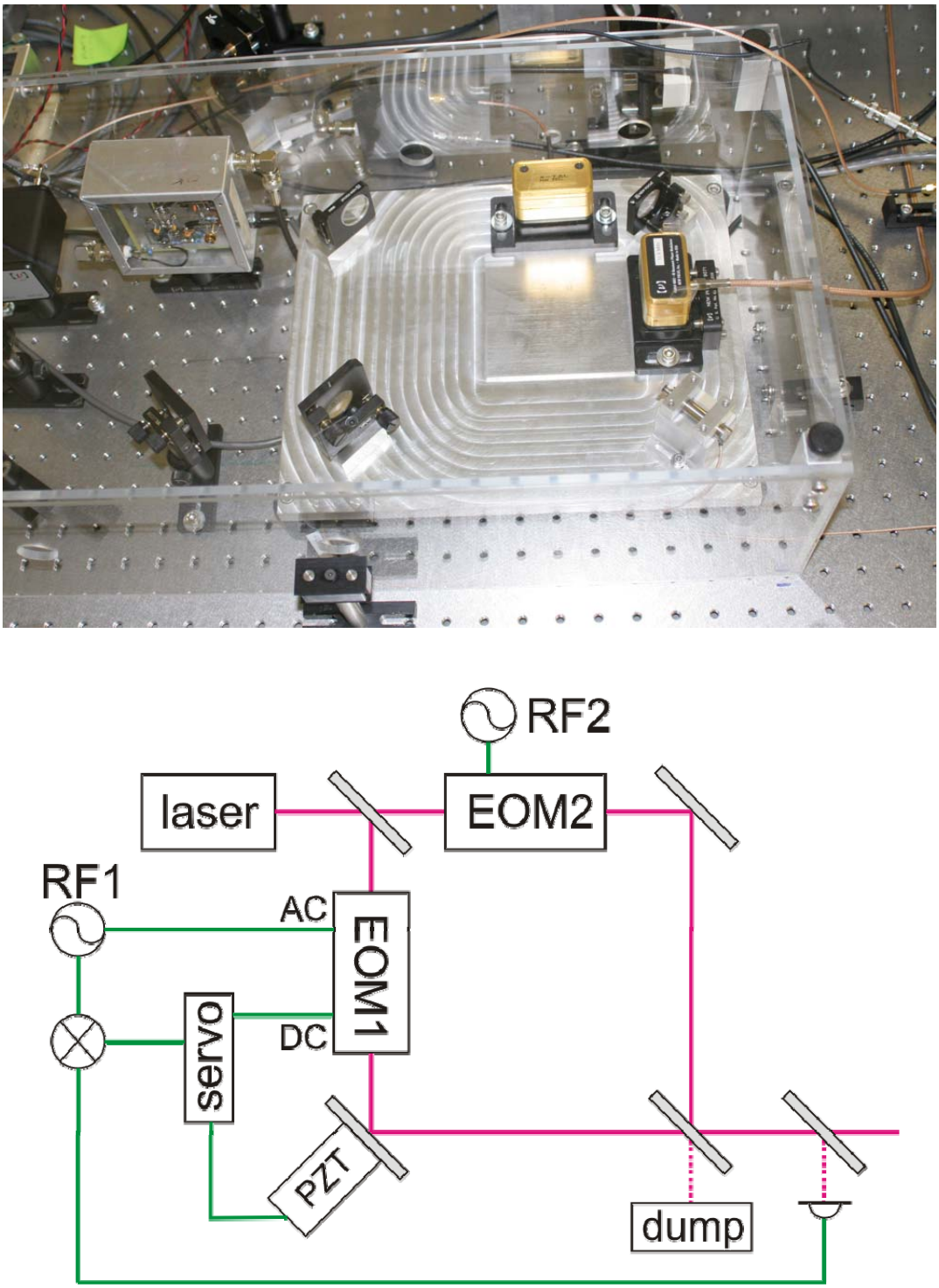

Figure 6.5. Experimental MZ layout. Photo (top) and schematic drawing (bottom).

The EOM2 shown in Figure 6.5 was an off-shelf resonant phase modulator from New Focus while EOM1 was based on an AdvLIGO design (albeit using a $LiNbO_3$ crystal) using a modified external

resonant / impedance matching circuit that permitted a feedback path for frequency actuation signals. The circuit is shown in Figure 6.6.

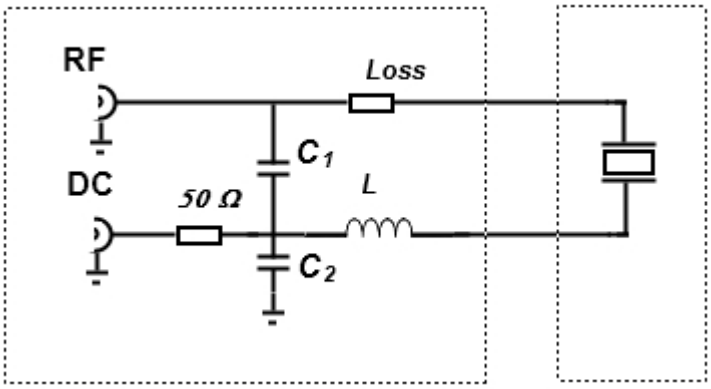

Figure 6.6. Modified impedance matching circuit with DC input and EOM in separate housings.

These modifications allowed us to use the EOM to apply the phase modulation sideband and simultaneously to use it for fast phase (optical path length) correction of the differential arm length. In this prototype, EOM1 was made resonant for 25 MHz and EOM2 was resonant for 31.5 MHz. The 31.5 MHz frequency was used in an internal modulation scheme to generate the error signals for the differential mode. The light for the MZ stabilization is sampled with a pick-off mirror in the bright port of the interferometer.

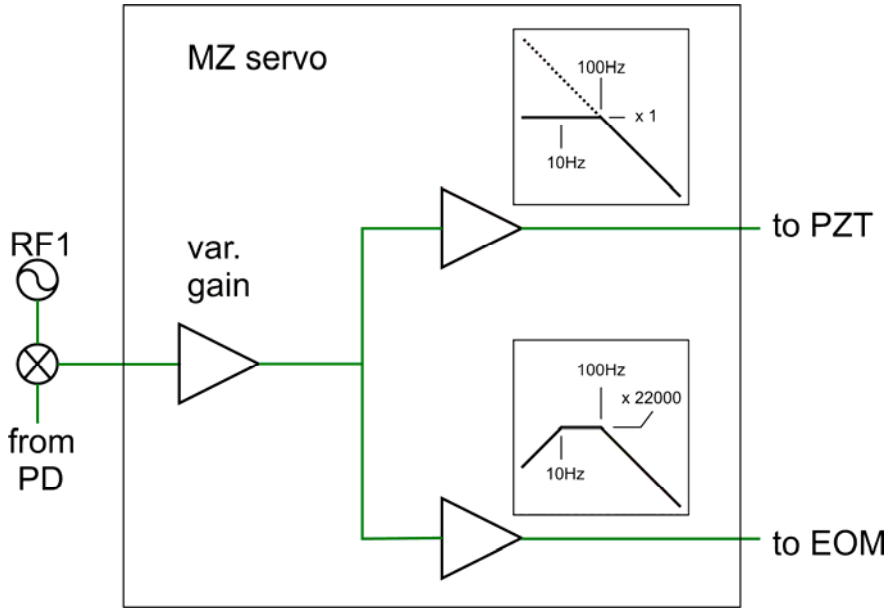

Figure 6.7. Schematic servo design with slow and fast actuator output.

The servo, which is schematically shown in Figure 6.7 above, splits the control signals in “fast” and “slow” components and feds the slow (but with a high dynamic range for drift control) part

back to the PZT and the fast part to the DC input of the EOM. The PZT has a half-wave voltage $V_\pi = 1.04$ V, the EOM shows a $V_\pi = 210$ V and therefore the electrical gain in the EOM part of the servo has to be significantly higher than in the PZT part. Even though the electronic gain is 22000 times bigger at 100 Hz the noise suppression is only 100 times bigger for the EOM as shown in the following measurement. Figure 6.8 shows the achieved unity gain bandwidth of 40 kHz with about 30 dB noise suppression at 1 kHz when using the combined PZT and EOM servo loop. The remaining servo-bump at 100 kHz will be removed in future versions of the servo design.

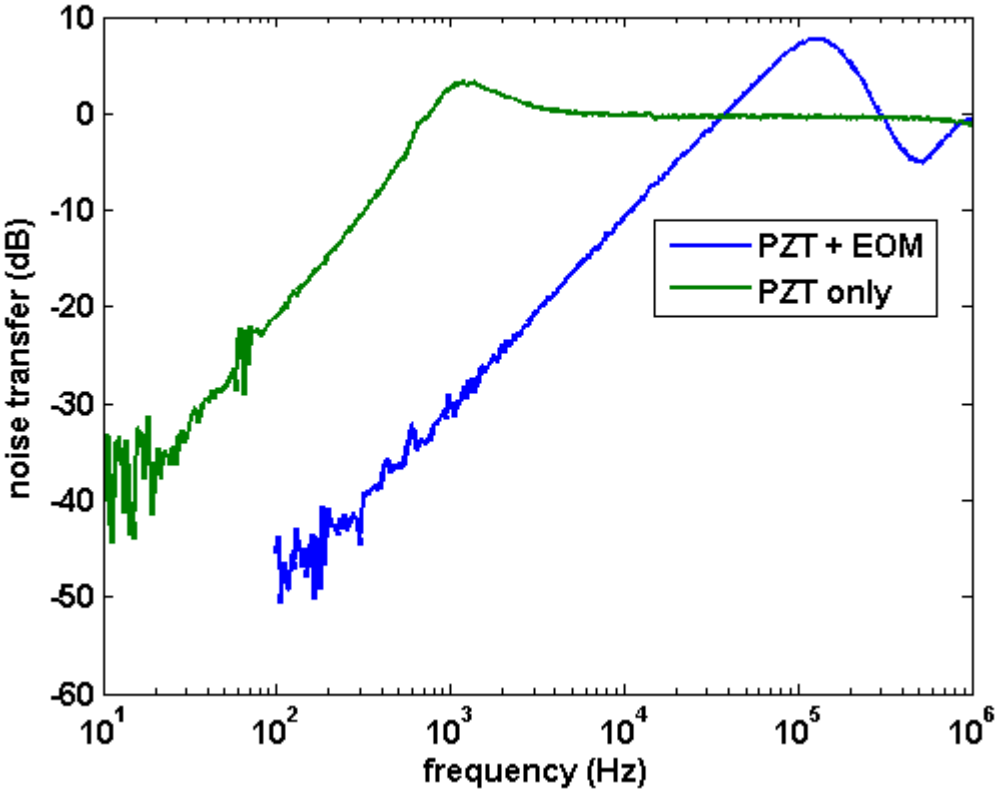

Figure 6.8. Closed-loop noise suppression TF

The complete setup was covered by a Plexiglas enclosure to limit the influence of the environment and the error point noise was used to determine the remaining differential length noise to be less than $10^{-13}\frac{\mathrm{m}}{\sqrt{\mathrm{Hz}}}$, currently limited by the Spectrum Analyzer input noise. Measurements to measure the differential length noise with an independent mixer in an out-of-loop fashion are currently in preparation.

6.6.4 Power scaling

The current set up is not yet ready to handle 180 W of input light but very few changes have to be made to adapt it to this power level. First the EOMs have to be replaced with the final design using RTP crystals instead of MgO:LiNbO3 crystals and secondly the beamsplitters as the only transmissive optics have to be replaced with superior low absorption fused-silica substrates.

7 Input Mode Cleaner

The laser light must be frequency and spatially stabilized before it can be used in the interferometer. The input mode cleaner provides active frequency stabilization through feedback to the PSL, passive frequency noise suppression above its cavity pole frequency, and passive spatial stabilization at all frequencies. The input mode cleaner also reduces higher order modal content of the laser light, suppressing bean jitter.

7.1 Optical Configuration and Definitions

The input mode cleaner is a Fabry-Perot cavity with a moderately high finesse. Its shape is that of a narrow isosceles triangle, as shown in Figure 7.1. The triangle configuration is preferred for several reasons, notably the improved optical isolation it provides. The cavity configuration is flat-flat-curved. The two flat mirrors (IMC1 and IMC3) define the base and act as the input and output couplers. These are located in HAM2. The curved mirror (IMC2) is in HAM3. All three mirrors are suspended.

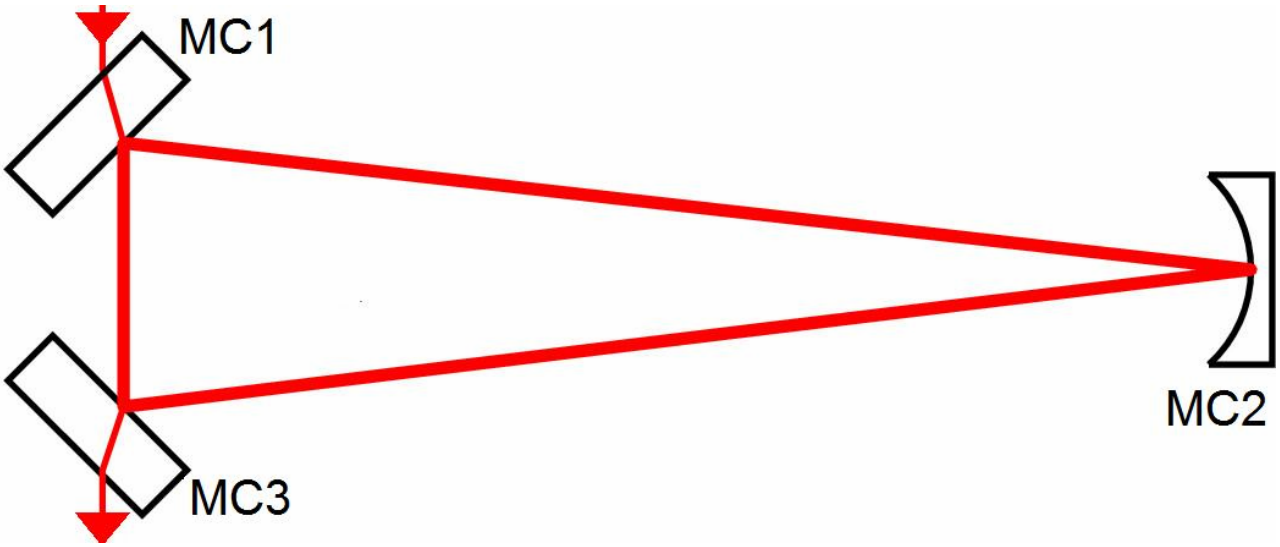

Figure 7.1. Diagram of the input mode cleaner, defining the names of the mirrors.

The three-mirror ring Fabry-Perot cavity has amplitude transmission

$$t = \frac{t_1 t_3 e^{i\beta}}{1 - r_1 r_2 r_3 e^{2i\delta}} \qquad \textbf{(7.1)}$$

for s-polarized light (perpendicular to the plane of the IMC). Here t_i is the amplitude transmissivity and r_i the amplitude reflectivity of the i^{th} mirror, i = IMC1-IMC3; β is the optical phase gained by traveling the base of the triangle; 2δ is the optical phase associated with the cavity round trip length L. (The factor of 2 is to maintain similarity with linear cavities, where the length is usually given as the one-way length.) For plane waves,

$$2\delta = \omega L/c - 3\pi \qquad \textbf{(7.2)}$$

where ω is the angular frequency of the light and there is π phase retardation on reflection at each mirror. The resonator has transmission maxima whenever $\delta = n\pi$, with n an integer.

The input mode cleaner is located in vacuum. The separation between the chambers determines the range of lengths (and thus of the free spectral range) of the input mode cleaner. The input mode cleaner mirrors are suspended in Mode Cleaner Triple Suspensions.

The specific functions of the IMC are discussed in the following paragraphs.

7.2 Input Mode Cleaner Optical Parameters

7.2.1 Constraints and Assumptions

The input mode cleaner (IMC), power recycling cavity (PRC), signal recycling cavity (SRC), and arm cavity lengths are all interrelated. The arm cavity length determines the PRC/SRC and IMC cavity lengths. Moreover, the arm cavities have only +/- 300 mm adjustability in terms of the initial placement of the mirrors and only ~2 mm once placed through motion of the tidal servos. The requirement is that the input mode cleaner and power-recycling cavity resonate the carrier and both locking sidebands but that the arms resonate only the carrier. The sideband is to be a small amount, nominally 5-6 Hz, offset from being maximally antiresonant in the arms.

7.2.2 Lengths

The sideband frequencies must satisfy

$$f_{prc} = (k + 1/2)c/2L_{prc} \qquad (7.3)$$

where (k = 0,1,2 ...) and L_{prc} is the power recycling cavity length. (Here the length is measured from the PRM to the average of the two ITMs.) The factor of 1/2 occurs because the carrier is resonant in the arm cavities whereas the sidebands are not resonant in the arms, giving an extra 180 degree phase shift in the reflectivity of the arms.

Both sidebands must be equal to one of the input mode cleaner resonances, because the RF modulation is imposed before the input mode cleaner. The resonant frequencies of the input mode cleaner are:

$$f_{imc} = nc/2L_{imc} \qquad (7.4)$$

where n is an integer (1,2,3 ...) and L_{imc} the input mode cleaner length.

The signal recyling cavity length is also tied to these frequencies; its length is[17]

$$L_{rcc} = (p + \delta_\phi/2\pi)c/2f_{src} \qquad (7.5)$$

where p is an integer (1,2,3 ...), δ_ϕ is the signal recycling detuning (0.1 rad), and f_{src} is the frequency used to sense the position of the SRM.

There is a modest range of adjustments available for L_{prc} and L_{imc}, determined by the dimensions of the LIGO vacuum envelope, the size of the optical tables, and considerations of other articles that

[17] "Optical Layout for Advanced LIGO," D. Coyne, LIGO-T010076-010D (7/1/2001)

must reside on these tables.[18] In turn, this determines a range of frequencies for both f_{prc} and f_{imc}. The union of these frequencies is available for the controls of the interferometer. The lengths are summarized in Table 4 (all dimension in m):

Table 4. Allowed range of lengths for LIGO cavities

Cavity	Configuration	Min	Max
IMC	All	15.910	16.461*
PRC	Straight, marginal	8.142	9.162
PRC	Straight, stable	55.480	59.255
SRC	Straight	8.606	9.626
AC	Straight	3994.455	3995.033
PRC	Folded, marginal	13.317	14.338
PRC	Folded, stable	60.602	64.495
SRC	Folded	13.321	14.238
AC	Folded	3994.206	3994.721

* The actual max is 0.6 m longer; this space is reserved for input injection optics. Using it for a longer mode cleaner would not affect any of the length issues (such as no 9 MHz frequency for the folded PRC) discussed below.

7.2.3 Modulation frequencies

The procedure we have used for fixing the modulation frequencies then begins by setting the arm cavity lengths. The length of the arm cavity for the straight (non-folded) interferometer is recommended to be 3994.750 m. The length for the folded interferometer is recommended to be 3994.450 m. Given these lengths, one can find a discrete set of frequencies spaced by 37.5 kHz that satisfy equations (7.3) and (7.4) and the nearly antiresonant condition for the sidebands with respect to the arm cavities. Finally, we can set the length of the SRC from equation (7.5).

The power recycling cavity length is of course quite different depending on whether marginal or stable configurations are chosen, and also differs between the straight (H1/L1) and folded (H2) interferometers.

We highlight one issue at this point: *Given the present location of the HAM chambers, there is no solution lower than 27.3 MHz for the folded interferometer with marginal PRC*. For the stable PRC, the lowest frequency is 17.6 MHz. The minimum frequencies could be reduced to 16.4 MHz (marginal) and 8.4 MHz (stable) by adding 1.8 m to the HAM2/HAM3 separation.

The cases are discussed in the following sections.

[18] "Constraints of Advanced LIGO Cavity Lengths, Version 2" by Luke Williams, LIGO T-###

7.2.4 Straight IFO, Marginal PRC

The length ranges for the IMC are 16.284-16.461 m. The length ranges for the PRC are 8.142-8.321 m. (This is the range for each where solutions exist.) A set of lengths (and corresponding frequencies) that meet the requirements is:

Table 5. Straight IFO, Marginal PRC

AC Length	m	3994.750
IMC Length	m	16.338
PRC Length	m	8.169
First frequency	MHz	9.1744
Second frequency	MHz	45.8722
SRC Length	m	9.855*
Alternative second frequency	MHz	64.2211
Alternative SRC length	m	9.373
High second frequency	MHz	183.4890
SRC length for high frequency	m	8.999

*This length is 229 mm *longer* than allowed by physical constraints in the SRC HAM.

One could use IMC and PRC lengths of 16.406 m and 8.203 m respectively also; this is the only other possibility if the low modulation frequency is to be near 9 MHz.

7.2.5 Straight IFO, Stable PRC

The length ranges for the IMC are 15.910-16.461 m. The length ranges for the PRC are 55.685-57.614 m. A set of lengths (and corresponding frequencies) that meet the requirements are”

Table 6. Straight IFO, Stable PRC

AC Length	m	3994.750
IMC Length	m	15.947
PRC Length	m	55.815
First frequency	MHz	9.3996
Second frequency	MHz	46.9979
SRC Length	m	9.619
Alternative second frequency	MHz	65.7971
Alternative SRC length	m	9.149
High second frequency	MHz	175.5922
SRC length for high frequency	m	9.246

7.2.6 Folded IFO, Marginal PRC

The length ranges for the IMC are 15.980-16.461 m. The length ranges for the PRC are 13.317-13.718 m. A set of lengths (and corresponding frequencies) that meet the requirements are:

Table 7. Folded IFO, Marginal PRC

AC Length	m	3994.450
IMC Length	m	16.139
PRC Length	m	13.449
First frequency	MHz	27.8631
Second frequency	MHz	65.0140*
SRC Length	m	13.870
High second frequency	MHz	185.754
SRC length for high frequency	m	13.731

* 46.4386 MHz leads to a SRC length of 12.936 m, 255 mm too short.

The PRC is longer for the folded interferometer, putting its first resonance at 5.2-5.6 MHz and its second resonance near 15.7-16.9 MHz. Neither frequency is consistent with the 9.26 MHz median input mode cleaner FSR; the first hit occurs for $n = 3$ and $k = 2$ in equations (7.3) and (7.4) above.

If the tube that links HAM2 and HAM 3 were increased in length by 1.8 m, then the input mode cleaner FSR is decreased to 8.33 MHz, and a frequency of 16.65 MHz could be used. (Note that this tube is scheduled for replacement in Advanced LIGO.)

7.2.7 Folded IFO, Stable PRC

The length ranges for the IMC are 16.160-17.061 m. The length ranges for the PRC are 60.602-63.979 m. A set of lengths (and corresponding frequencies) that meet the requirements are:

Table 8. Folded IFO, Stable PRC

AC Length	m	3994.450
IMC Length	m	16.221
PRC Length	m	60.829
First frequency	MHz	18.4816
Second frequency	MHz	64.6857
SRC Length	m	13.941
High second frequency	MHz	175.575
SRC length for high frequency	m	8.551

If the tube joining HAM2 and HAM3 were increased in length by 1.8 m, a low frequency between 8.31 and 8.46 MHz could be employed.

7.2.8 Calculated Optical Parameters

The following sections list the optical parameters chosen for the input mode cleaner. To save space, the results are presented only for the straight interferometer, marginal PRC case. Gaussian parameters change a few % for the other cases.

Table 9. Optical parameters for the straight interferometer, marginal PRC

IMC Length	m	16.338
IMC free spectral range	Hz	9,174,449
IMC polarization		's'(⊥ to plane of IMC
IMC1/3 radius of curvature	m	>10000
IMC1/3 transmittance		0.006
IMC1/3 reflectance		0.994
IMC2 radius of curvature (cold)	m	26.769
IMC2 transmittance		<0.00001
IMC2 reflectance		0.9999
Mirror absorption/scatter loss (each)	ppm	30
IMC finesse		519
Cavity Pole Frequency	Hz	8,830
Cavity g factor		0.3897
IMC waist	mm	2.103
Rayleigh range	m	13.05
Input Power	W	165
Stored IMC Power	kW	23.2
Intensity at Flat mirrors	kW/cm^2	167
IMC mirror mass	kg	2.92
IMC mirror diameter	cm	15
IMC mirror thickness	cm	7.5
IMC1,3 HR center-center distance	cm	43.18
IMC1,3 intracavity angle of incidence, θ	deg	44.625
Static radiation pressure (IMC1/IMC3)	Pa	7.9

Static radiation pressure (IMC2)	Pa	4.3
Static force from radiation pressure (IMC2)	μN	155

7.2.9 Input Mode Cleaner Locking Frequency

The modulation frequency to be used to lock the mode cleaner is not transmitted (heavily attenuated by the IMC) and can be considered non-critical as long as overlap with the modulation frequencies for the core interferometer is avoided. We choose a value of **32.011 MHz** (**TBR IO**), for the IMC locking, about 100 kHz off the fourth antiresonance (n = 3.5).

7.3 Input Mode Cleaner Expected Performance

7.3.1 Transmission

Fig. 7.2 shows the calculated mode cleaner transmission as a function of frequency for one FSR above the carrier.

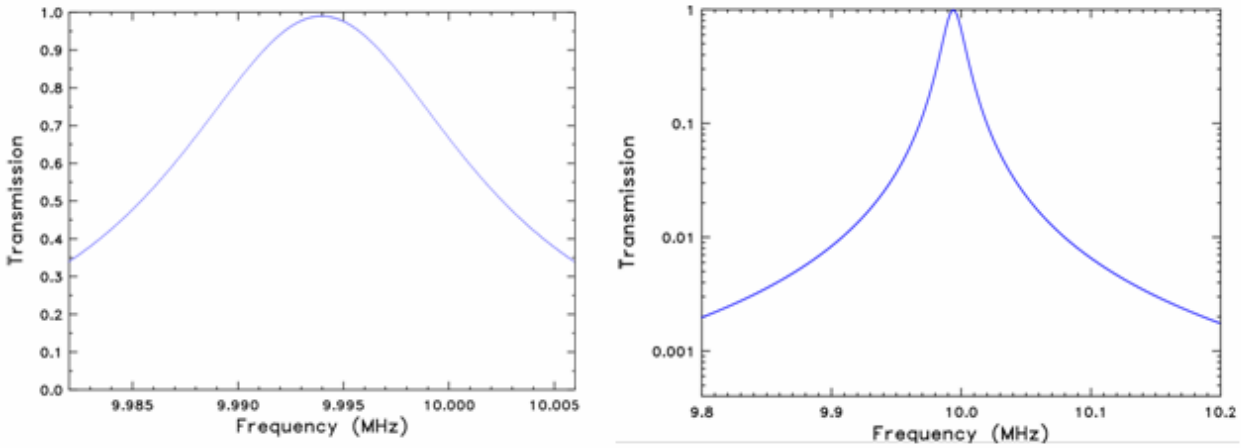

Figure 7.2. Calculated input mode cleaner transmission as a function of frequency, one FSR above the carrier. The left panel shows the spectrum on a broad frequency scale and a logarithmic scale for the transmission; the left panel shows the detail.

7.3.2 Jitter Suppression

For Advanced LIGO, the beam jitter required at the input to the core optics is such that the relative amplitude of the TEM_{10} mode is 4×10^{-9} /$Hz^{1/2}$ at 230 Hz and above, rising as $1/f^2$ below 230 Hz. The pointing from the PSL is expected to be 1×10^{-6} /$Hz^{1/2}$. The input mode cleaner therefore must provide a filtering of a factor of 250.

Beam wiggle (angular and lateral deviations of the beam) may be viewed as the superposition of higher-order Gaussian modes on the TEM_{00} mode. Because higher-order modes are suppressed by the input mode cleaner, beam wiggle is also suppressed. The amplitude of the suppression is

$$S_{lm} = \frac{1}{\left[1 + \left\{\frac{2\mathcal{F}}{\pi}\sin[(l+m)\,\mathrm{acos}(\sqrt{g})]\right\}^2\right]^{\frac{1}{2}}} \qquad \textbf{(7.6)}$$

where $\mathcal{F}$ is the finesse of the cavity. For high-order mode reduction, the quantity $(l+m)\,\mathrm{acos}(\sqrt{g})$ is chosen *not* integer times π, making value of the sinusoid not zero. If we take it to be a typical value, 1 rad, then, since $\mathcal{F}$>>1,

$$S_{lm} \approx \frac{\pi}{2\mathcal{F}\sin(1)} \qquad \textbf{(7.7)}$$

A finesse of 500 will meet the jitter requirements.

7.3.3 Higher Order Mode Rejection

For TEM_{lm} Gaussian modes, the input mode cleaner Fabry-Perot resonances occur at frequencies

$$\nu_{lm} = \frac{c}{2L}\left[n - \frac{1}{2} + \frac{l+m+1}{\pi}\,\mathrm{acos}(\sqrt{g})\right] \qquad \textbf{(7.8)}$$

where $g = 1\text{-}L/R$ with R the radius of curvature of the curved mirror. The resonator is adjusted for resonance with the TEM_{00} mode; this sets the value of n (of order 30 million). The cavity length and mirror radius of curvature (and hence g) are chosen so that the resonance condition can be satisfied for some n and l=m=0 not satisfied any other $\{n,l,m\}$. This condition is met when

$$\frac{l+m}{\pi}\,\mathrm{acos}\sqrt{g} \neq integer + \varepsilon \qquad \textbf{(7.9)}$$

where ε specifies the amount the higher-order mode avoids being resonant. It is assumed that the actual frequency from the laser of the fundamental and all higher-order modes is the same.

Fig. 7.3 shows the transmittance of the mode cleaner (in ppm) vs. mirror radius of curvature. The mode cleaner was taken to be illuminated with light in which all the modes with the fundamental and higher modes satisfying $0 < l + m < 65$ existed with amplitude ~ 1/sqrt($l + m$). The transmittance of the fundamental is unity. As the radius of curvature is varied, one or another of the higher order modes is transmitted. There is a large peak of 14% at r = 26.73, when the modes with $l + m$ = 7 are transmitted, and then a broad decrease at higher radius, followed by many narrow peaks for larger values of $l + m$. Because the radius of curvature changes by 0.13 m (see below) between cold and hot cases, we pick the cold ROC at r = 26.769 m anticipating an increase to 26.9 m when hot.

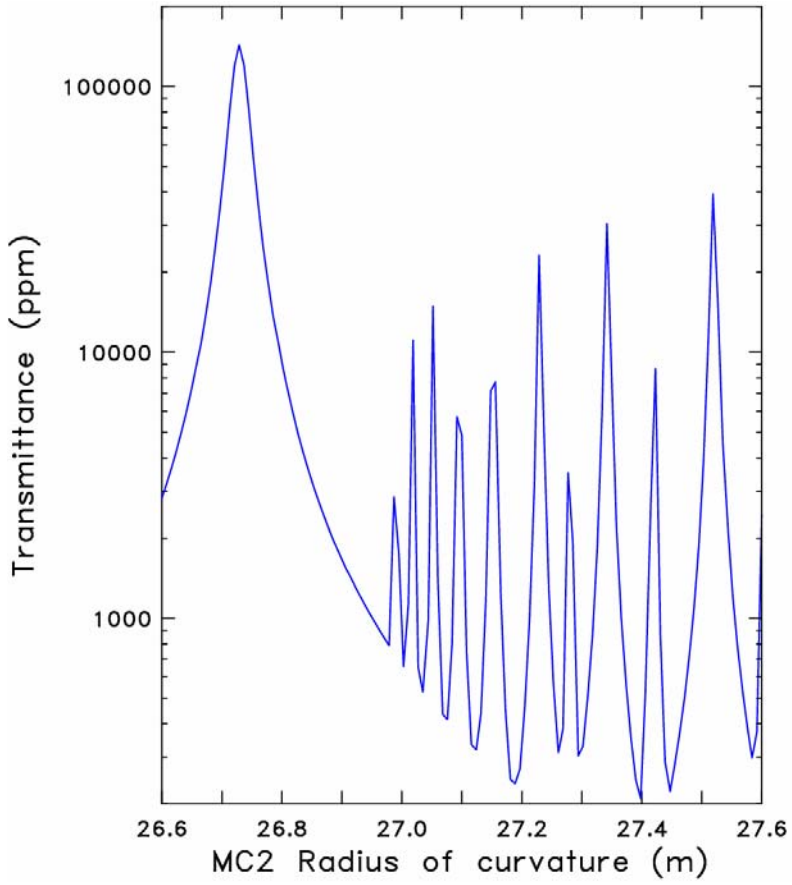

Figure 7.3. Transmission of IMC Cavity

7.3.4 Laser wavelength stabilization

The input mode cleaner can serve as a length standard for the laser. The arms are better standards, but the input mode cleaner plays an intermediate role in the length control system.

7.3.5 Laser noise suppression

The input mode cleaner acts as a low-pass filter, with a corner frequency of $f_c = 1/\tau$, where $\tau = 2FL/c$ is the storage time of light in the cavity. Amplitude and frequency noise at frequencies above the corner frequency are suppressed as $1/f$ (20 db/decade).

7.3.6 Polarization

The input mode cleaner transmission is polarized. Because the light in the input mode cleaner has an odd number of reflections during one round-trip circuit, the overall phase of s-polarized light (E normal to plane of the cavity) is reversed on one circuit. This effect shifts the resonance condition from the usual $\nu = cn/2L$ to

$$\nu = \frac{c}{2L}\left(n - \frac{1}{2}\right)$$

The phase reversal does not happen for p-polarized (*E* in the plane) light, for which ν= *cn/2L*. Thus, the input mode cleaner acts as polarization sensitive filter. As its length is varied, first one and then the other polarization are transmitted.

The input mode cleaner uses s-polarized light (perpendicular to the plane of the IMC).

7.3.7 Input Mode Cleaner Instabilities

7.3.7.1 Optical Spring Effect

The static radiation pressure force in the IMC when on resonance (see above) is 155 μN. If the length of the IMC is changed, this force drops; this change of force with length resembles a spring.[19] The spring is unusual, in that its spring constant is itself linear in the distance from the cavity resonance. The "spring constant" k_{opt} can be calculated: $k_{opt} = dF_{RP}(x)/dx$, where $F_{RP}(x)$ is the radiation pressure force in the cavity, and follows the usual Fabry-Perot resonance form. In the IMC, this resonance (for fixed laser wavelength) occurs over 1.2 nm (FWHM), and the corresponding optical spring would have maximum spring constant (near the ¾ maximum points) of +/- 130,000 N/m. This is enormously larger than the 170 N/m restoring force of the pendulum suspension. Fortunately, the mode cleaner servo keeps the mirror much closer than 1.2 nm to the resonance; if the deviations are +/- 1 pm, the optical spring constant will be below 160 N/m comparable (but not negligible) to the gravitational spring. Thus optical spring effects could change the pendulum resonances by 40%.

7.3.7.2 Angular (Sidles-Sigg) Instabilities

These instabilities[20] work as follows: angular misalignment of the beam in the cavity (decentering) introduces a torque on the suspended mirrors. If fluctuations in this radiation induced torque become larger than the restoring torque of the torsion pendulum, then the resonator becomes unstable. Following the analysis in LIGO-T030275 we calculate the critical power $P_{crit} = \Theta c\omega^2/2k_2L$ (where Θ is the suspension angular moment, ω is the pitch angular frequency, $k_2 = 0.39$

---

[19] V. B. Braginsky, M. L. Gorodetsky, and F. Ya. Khalili, Phys. Lett. A **232**, 340 (1997);

Benjamin S. Sheard, Malcolm B. Gray, Conor M. Mow-Lowry, David E. McClelland and Stanley E. Whitcomb, "Observation and characterization of an optical spring," Phys. Rev. A **69**, 051801(R) (2004); A. Di Virgilio, et al. "Experimental evidence for an optical spring." Phys. Rev. A **74**, 013813 (2006).

[20] John A Sidles and Daniel Sigg, "Optical torques in suspended Fabry Perot interferometers." Physics Letters A **354**, 167-172 (2006); Daniel Sigg, "Angular Instabilities in High Power Fabry-Perot Cavities," LIGO-T030120-00; Daniel Sigg, "Angular Stability in a Triangular Fabry-Perot Cavity," LIGO-T030275-00.

is a *g*-dependent eigenvalue of the equations of motion, and *L* is the cavity length) for the IMC. We obtain P_{crit} =2.0 MW, compared to the 23 KW circulating power in the advanced LIGO IMC design. The mode cleaner should not suffer from this instability.

7.3.7.3 Parametric Instabilities

Although a rigorous analysis has not been done, the IMC is also free of these instabilities, on account of the small spot sizes and large free spectral ranges.

7.3.8 Input Mode Cleaner Thermal effects

Circulating power

The stored power in the input mode cleaner is larger than the incident power by 1/*T*, with *T* the (power) transmittance of the input and output couplers.

Absorption in coatings and the substrates of the input mode cleaner mirrors will lead to changes in the effective radii of curvatures, changing and distorting the spatial eigenmode of the input mode cleaner. The heating in the coating will change the sagitta δs across the beam profile of the input mode cleaner mirrors. This change can be approximated by the Hello-Vinet theory and the details are presented in the supporting document LIGO T070090-00-D.

Based on an absorption coefficient of 0.5 ppm for the coatings and 10 ppm/cm substrate absorption, the fused silica mirror will change their sagitta by δs = 0.523 nm for the IMC1 and IMC3 mirrors and a beam waist of 2.1028 mm. This would change the radii of curvatures of the flat mirror to -4 km. The radius of curvature of the curved mirror would change from 26.769 to 26.840 m due to a sagitta of 0.62 nm for a 3.4 mm beam size. (See Table 10.) However, an effective radius of curvature at IMC2 that incorporates the change of -4 km at IMC1 and IMC3 and the 10 km change at IMC2 can be modeled as if the hot ROC of curved mirror is 26.9116 m. This is the number that can be used to find the hot beam waist and the g-factor of the cavity. . Note that we are using a substrate with an absorption of 10 ppm/cm. This substrate produces more thermal lensing than would occur with the best Suprasil (4 ppm/cm). Apart from decreasing cost, simulations show that the use of this substrate with its the higher thermal lens actually helps in reducing the amount of adaptive thermal lensing required to be generated by the ring heater around the DKDP in the Faraday subsystem.

The substrates of IMC1 and IMC3 will act as a thermal lens for the input and output beams. Using the Hello-Vinet theory and the absorption losses mentioned above, a thermal lens of 135 nm is expected. This corresponds to a sagitta of 15.5 nm. This lens is astigmatic in nature because of the 45^0 angle of incidence at the flat mirrors. The value of 135 nm corresponds to sagittal plane. The thermal lens in the tangential plane is smaller by a factor of 2 because the beam waist in the tangential plane is larger by a factor of $\sqrt{2}$. Therefore a lens of 270 m is expected in the tangential plane. However, for the worst case scenario, if we consider an equal thermal lens of 135 m in both directions, the resultant mode miss-match is less than 0.4% as the interferometer goes from cold to hot state. This thermal lensing if left unchecked will not decrease the power in the TEM_{00} mode appreciably.

The thermal lensing in the IMC mirror will actually be used to improve the mode matching. This will be done by ensuring that the residual thermal lensing in the FI stays negative. Then the positive lens in the IMC mirror will cancel the effect of residual thermal lensing in FI to a certain extent. A

RH is being planned around DKDP crystal that will further ensure that the beam parameters as seen by the mode stay same from cold to hot operation. Further details of the scheme will be discussed in Section 9.

With 26 kW stored in the cavity, and 50 ppm losses at each mirror, the changes in cavity parameters from cold to hot cavity are:

Table 10. Temperature effects in the IMC

		cold	Hot
IMC1 radius of curvature	m	>10000	-4000
IMC2 radius of curvature	m	26.769	26.9116
IMC3 radius of curvature	m	>10000	-4000
Cavity g factor		0.3897	0.3929
IMC waist	mm	2.1028	2.1098
Rayleigh range	m	13.0558	13.1429

The rejection and dewiggling properties of the input mode cleaner are not affected by heating.

Frequency Noise

Length fluctuations of the input mode cleaner will compromise the frequency stability of the light leaving the input mode cleaner. Figure 7.4 shows the expected total frequency noise performance and individual contributions to the IMC frequency noise assuming the characteristics above. The frequency stability is limited by technical radiation pressure noise over the entire frequency range. This stability and the allowed frequency noise of the field going into the main interferometer set the requirements on the frequency stabilization loop gains.

7.3.9 Input Mode Cleaner Noise Budget

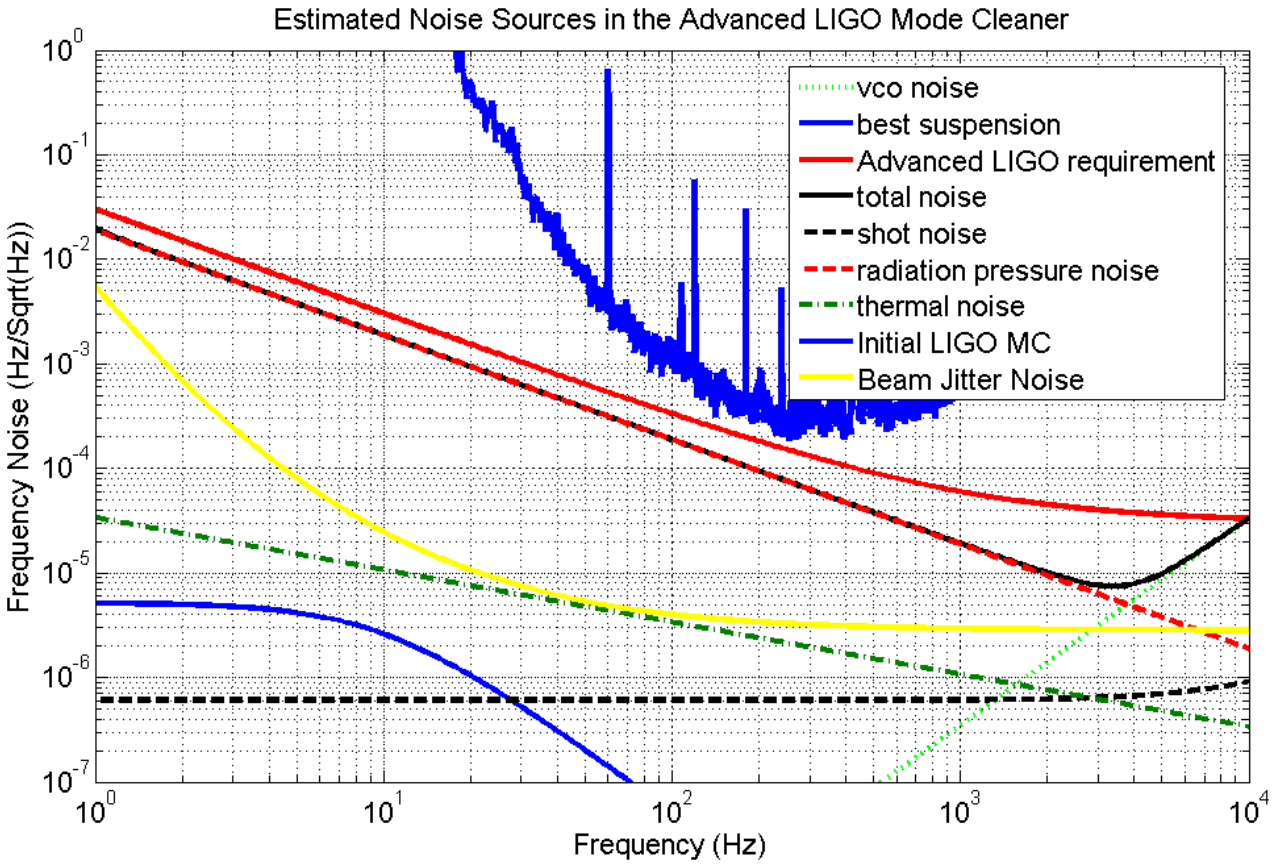

Figure 7.4. Predicted IMC Frequency noise properties.

The code for this plot is described in LIGO-T030258-00-R "Single Test Cavity Design and use of the Xarm for LASTI," David Ottaway 10/30/03, but the calculation is for the mode cleaner of Advanced LIGO.

8 Faraday Isolator

The Faraday Isolator (FI) is responsible for rejecting the back-reflected light from propagating towards the IMC and generating phase noise in the interferometer. It is also responsible for providing light in the symmetric (REFL) port for control of the interferometer length and alignment DOFs. At high optical powers, absorption in the FI optical components generates thermally-induced birefringence, thermal lensing and beam steering, requiring alternative designs and compensation methods, as well as a careful selection of the polarizers and crystals.

The Advanced LIGO Faraday Isolator design under went a Preliminary Design Review on 28 April 2006 in anticipation of Enhanced LIGO.[21] Here, we briefly update the status of the FI design since the PDR.

8.1 Faraday Isolator Design

The Faraday Isolator consists of a birefringence-compensated Faraday Rotator (consisting of two TGG crystals and a quartz rotator), polarizers, a λ/2 waveplate, and a negative dn/dT material for thermal lens compensation.[22]

The FI for Advanced LIGO will most likely use three polarizers instead of two: a pair of calcite wedge polarizers (CWP) possessing high extinction ratios for optimal isolation and a thin film polarizer (TFP) inserted in between to minimize power-dependent beam steering in the REFL port.

8.2 Optical Characterization

Here, we separately investigated the isolation and the beam steering at optical powers as high as 103 W using a mode size of 3.9 mm, nearly identical to that expected in Advanced LIGO. Two different configurations[23] were tested:

- A hybrid configuration, consisting of a fused silica thin film polarizer and a 2.5 mm thick calcite wedge, with a 4.3^{o} wedge angle (TFP + CWP).
- A pair of identical calcite wedge polarizers (CWP + CWP) – same as in the (TFP + CWP) setup.

The performances of the FI are summarized in Table 11 below.

While we have not yet characterized the full 3-polarizer setup, the two tests above provide confidence that it will work. A full test will take place at LLO in September, 2007

---

[21] LIGO-T060267-00-D, "Upgrading the Input Optics for High Power Operation", UF LIGO Group, IAP Group; LIGO-G060361-00-D, Modulators and Isolators for Advanced LIGO, UF IOO Group.

[22] E. Khaznov, N. F. Andreev, a. Mal'shakov, O. Palashov, A. K. Poteomkin, A. Sergeev, A. A. Shaykin,V. Zelenogorsky, I. A. Ivanov, R. Amin, G. Mueller, D. B. Tanner, and D. H. Reitze, "Compensation of thermally Induced Modal Distortions in Faraday Isolators" IEEE J. Quantum Electron., 40, 1500-1510 (2004).

[23] The high power performance of the FI was previously tested in a third configuration, consisting of two thin film polarizers, with very satisfactory results regarding beam drift (1.5 μrad at 30 W optical power).

Table 11. Performance of the Advanced LIGO FI

Performance		*TFP + CWP*	*CWP + CWP*	*Comments*
Isolation Ratio (at 103 W input):		**39 dB**	**49 dB**	For TFP + CWP, 39 dB is limited by the extinction of the TFP.
Variation in isolation across 0-103 W		**< 1 dB**	**< 5 dB**	For CWP + CWP, isolation is maximum at maximum input power and decreases at lower powers.
Maximum back-transmitted Power (103 W input):		**12.9 mW**	**1.3 mW**	Better suppression for the CWP + CWP setup.
% Transmitted Power:		**94 %**	**95 %**	The FI was optimized for max. isolation (min. back reflection).
Total Optical Losses (at 103W input):		**6 W**	**5 W**	Of which ~ 3 W are lost in the second polarization of the second CWP.
Thermal Drift (at 103W input): *(± 30 μrad)*	*Transmission:*	**< 30 μrad** ***(0.3 μrad/W)***	**< 50 μrad** ***(0.5 μrad/W)***	Larger drift for CWP + CWP setup.
	Reflection:	**< 50 μrad** ***(0.25 μrad/W)***	**< 80 μrad** ***(0.4 μrad/W)***	Drift in reflection is ~twice as in transmission (FR and first CWP are double passed).

8.2.1 Optical Isolation

The optical isolation was determined as the dB ratio between the incident and the backward transmitted light. In Figure 8.1 below, the isolation ratio vs. incident optical power is displayed for each of the two configurations. In each case, the setup was optimized for maximum isolation at the highest power (103 W) and not adjusted thereafter.

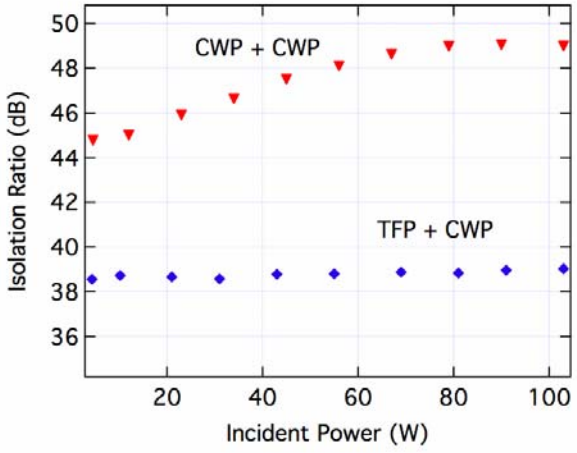

Figure 8.1. Power-dependent optical isolation for FI using one TFP and CWP (blue diamonds) and a pair of CWPs (red triangles)

The TFP + CWP configuration presents a lower isolation ratio (39 dB), limited by the extinction ratios of the TFPs (measured to be 40 dB). An isolation ratio of 49 dB is obtained at 103 W for CWP + CWP, essentially constant for power changes from 80 to 103 W. It decays to 44 dB as the power is reduced.

8.2.2 Thermal Drift

Thermal beam steering in forward transmission and back reflection were measured at 103 W incident power, with a Quadrant Photodetector (QPD) located ~2.5 m from the FR. The beam was first blocked for 45 min and then recorded the beam displacement for 30 minutes after illumination. As some optical elements warm up as they are illuminated (0^o mirror that reflects light back into FI as well), it is not possible to separate the thermal drift caused by the FI from the environmental drift (temperature changes). Including the environmental contribution, a maximum value of **80 μrad** was measured at 103 W in reflection for the double calcite wedge setup **(0.40 μrad/W)** and **50 μrad** was measured at 103 W in reflection for the double calcite wedge setup **(0.25 μrad/W)**.

8.2.3 Thermal Lens Compensation

This was investigated in a previous study[22] in a double calcite polarizer setup, by placing a DKDP crystal after the second polarizer of the isolator. The total thermal lensing observed at 70 W of incident power was 40 m. The original thermal lensing from TGG was about 8 m. Therefore a correction factor of about 5 was obtained. The experiments were repeated at LLO in vacuum, at 30 W laser power, and a cumulative thermal lensing of -40 m to -56 m was found. Here, the DKDP crystal slightly overcompensated the positive lens induced in the two TGG crystals. No significant difference regarding thermal lensing was observed between vacuum and air. We are planning to buy new DKDP crystals whose length will compensate the thermal lensing in TGG to a much better extent. Testing in vacuum at LLO will take place once the new parts have been received.

8.3 Vacuum compatibility

A modified housing design of the Faraday rotator was vacuum-baked (at 60C) and tested at Caltech in December 2006. An analysis by Dennis Coyne of the outgassing rate indicated that it was adequate for Enhanced LIGO and possibly Advanced LIGO, but showed high levels of “broad carbon peaks repeating every 14 AMU (broadly around 41, 55, 69, 83) … with robust signal”. This unit was then rebaked at 80 C showing improved outgassing and no degradation in magnetic field strength.

For details, see http://www.ligo.caltech.edu/~rtaylor/your%20folder/Luke_Williams.htm

The modified design has undergone a cavity contamination test at Caltech and has not caused any degradation of the cavity.

8.3.1 Preliminary UHV performance tests

The Faraday isolator in the two-calcite polarizer configuration was tested in vacuum at pressure values as low as 2×10^{-4} torr The isolator was optimized at 1 atm and the throughput light was measured as a function of the pressure inside the chamber while the chamber was being pumped, at

three different incident powers: 104 W, 50 W and 30 W. Preliminary results showed strong degradation of the isolation as the pressure was lowered below 0.1 Torr. This degradation can be explained by the less efficient convection cooling of the absorbing optical elements of the Faraday isolator at higher vacuum levels.

8.3.2 Isolation restoration with waveplate adjustment

Recently we have inserted a vacuum-compatible motorized rotation stage in the chamber to control the half-wave plate for a better optimization of the isolation. Fig. 8.3 shows that the isolation can be recovered by small adjustments of the half-wave plate in vacuum. For the data shown, the system had run for an hour and the waveplate adjusted for best isolation. Then, the isolation was measured at 10 minute intervals during the next 90 minutes, showing a decrease from just below 40 dB to about 36 dB. The initial isolation was then recovered by a fractional degree adjustment of the waveplate. There was a minor pressure increase, attributed to outgassing of the isolator as the temperature increased.

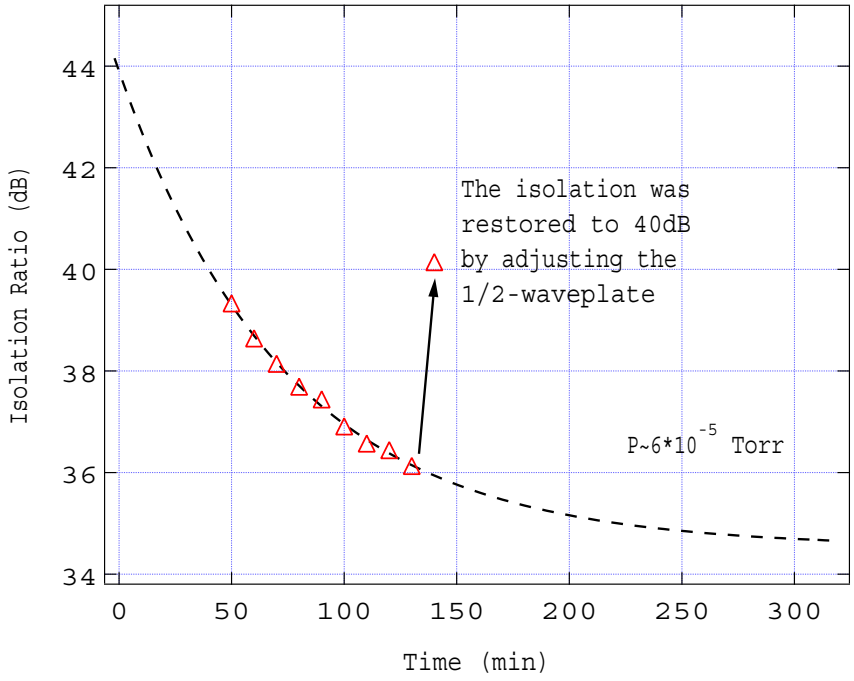

Figure 8.2. Isolation recovery with waveplate adjustment. The measurement was made at 30 W.

The experiments were repeated at LLO with the DKDP for thermal lens compensation, and the isolation was fully restored to the initial value of 44 dB with the in-situ waveplate adjustment, and stayed stable after 12 hrs time period.

8.3.3 Design of a TGG holder for more efficient heat transfer by conduction

In addition to restoring the isolation with the motorized waveplate, we have developed a design that has more effective conduction cooling channels, this way reducing the heat stored in the crystal, though the thermal effects associated with it.

Experiments continue at LLO, to investigate the time dependence of the thermally induced depolarization in the Faraday rotator and, separately, in the calcite polarizers, at constant, minimum achievable pressure.

8.4 Excess Phase Noise

As the parts of the Faraday Isolator are transmissive optics that are not suspended their motion is significantly bigger that that of the suspended optics and this could lead to extra phase/frequency noise in the light after the mode cleaner. The following sections will investigate the influence of moving focusing elements and prisms (wedged optics).

8.4.1 Movement of a focusing element

To estimate the phase changes because of transversal movement of lenses or curved mirrors we consider only perfect lenses. (This also applies to thermally generated lenses). The optimal form (no aberrations) of a focusing element with focal length f can be represented as the following change to the optical path for a given distance r from the axis:

$$\Delta l(r) = \frac{1}{4f} r^2 \qquad \textbf{(8.1)}$$

We use this to calculate optical path change that a beam experiences when it moves from the center of the element (r = 0) to a position r. This formula corresponds to the following phase change for light of the wavelength λ :

$$\Delta\phi = \frac{2\pi}{4f\lambda} r^2 \qquad \textbf{(8.2)}$$

From <http://ilog.ligo-wa.caltech.edu:7285/advligo/HAM_ISI_Expected_Performance> we can use the motion at 10 Hz ($3\cdot10^{-11}\frac{\mathrm{m}}{\sqrt{\mathrm{Hz}}}$) to estimate the introduced phase noise. For a focal length of f = 50 m this leads to a phase noise of $2.8\cdot10^{-17}\frac{\mathrm{rad}}{\sqrt{\mathrm{Hz}}}$. This corresponds to a frequency noise of $1.8\cdot10^{-15}\frac{\mathrm{Hz}}{\sqrt{\mathrm{Hz}}}$ and is well below the frequency noise requirement in LIGO-T010075-00-D at 10 Hz, which is around $10^{-5}\frac{\mathrm{Hz}}{\sqrt{\mathrm{Hz}}}$.

8.4.2 Movement of a prism (wedge)

The following picture illustrates the effect of a prism moving "perpendicular" to the beam.

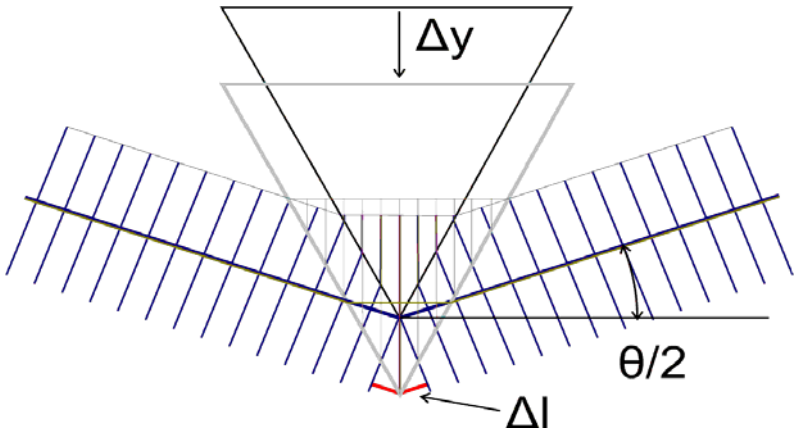

Figure 8.3. Prism moving perpendicular to the beam.

Even though the previous graph assumes plane waves it can be used to approximate the phase change of a moving (shaking) prism. In this configuration the effect is purely a phase change, but no beam shift. The path length change is:

$$\Delta l = 2\sin\left(\frac{\theta}{2}\right)\Delta y \quad \textbf{(8.3)}$$

The angle θ is the bending angle relative to the incident beam. The corresponding phase change is:

$$\Delta\phi = \frac{4\pi}{\lambda}\sin\left(\frac{\theta}{2}\right)\Delta y \quad \textbf{(8.4)}$$

If we assume that the bending of the beam by the two calcite wedges compensates because of the common ground motion, there will still be a residual angle by which the beam is bent because the deviation at each wedge depends on its alignment. For a (assumed) remaining angle of 0.005 degrees and motion at 10 Hz of ($3\cdot10^{-11}\frac{\mathrm{m}}{\sqrt{\mathrm{Hz}}}$) this leads to a phase noise of: $3.3\cdot10^{-8}\frac{\mathrm{rad}}{\sqrt{\mathrm{Hz}}}$ or $2.1\cdot10^{-6}\frac{\mathrm{Hz}}{\sqrt{\mathrm{Hz}}}$. This is still within the specification but great care has to be used when setting up the two anti-parallel wedges.

For TFP polarizers, we are safe as long as the surfaces of the TFPs are parallel to each other within 0.005 degrees (1/3 minute). This is about a factor of 10 better than commercial flats, so some effort will be needed to produce high quality TFPs

Note that the motion of the prism along the beam introduces a parallel beam shift of

$$\Delta r = \sin\left(\frac{\theta}{2}\right)\Delta x \ , \quad \textbf{(8.5)}$$

but has **no** effect on the phase.

8.4.3 Fizeau Effect

An analysis of the Fizeau effect was done for the conceptual design review. Since that time, the HAM seismic isolation requirements have been relaxed:

- Old requirement: $\delta x = 2 \times 10^{-13}$ m/rHz @ 10 Hz
- New requirement: $\delta x = 4 \times 10^{-11}$ m/rHz @ 10 Hz; 1.5×10^{-11} m/rHz, $f > 20$ Hz

This leads to an induced frequency noise of:

- Old: $\delta f = 1.5 \times 10^{-12}\ (f/10)^2$ Hz/rHz
- New: $\delta f = 3 \times 10^{-10}\ (f/10)^2$ Hz/rHz @ 10 Hz; $1.13 \times 10^{-10}\ (f/10)^2$ Hz/rHz $f > 20$ Hz

Comparing this to the IOO requirement of $\delta f = 3 \times 10^{-5}$ Hz/rHz above 1 kHz, we find that the frequency noise induced by the Fizeau effect meets the requirements below 5 kHz, but is slightly higher than requirement above 5 kHz (1.1×10^{-4} Hz/rHz at 10 kHz)

9 IFO MODE MATCHING TELESCOPE

The IOO MMT delivers the light from the mode cleaner to the IFO with the proper mode content. The IOO DRD requires that the coupling efficiency of light into the main interferometer shall be 0.95 or greater in TEM_{00}. The IOO MMT matches to the average of the two interferometer arm cavities ('common mode').

The MMT is designed to:

- compensate for static variations from design values in IOO as well as thermally-induced variations in the IOO components.
- provide for diagnostic measurement of the mode-matching in the IFO.
- Meet constraints imposed by the physical dimensions of the HAM stacks and vacuum system.

The MMT does not:

- Correct for differential mode changes between the X and Y arms due to static errors in the COC ROC. This falls in the scope of AOS (TCS).
- Correct for thermally induced variations in the COC components. This also falls in the scope of AOS (TCS).

9.1 Overview of Mode Matching Telescope Design

The configuration of the MMT depends upon the choice of specific recycling cavity design, i.e., Stable Power Recycling Cavity (SPRC) or Marginally Stable Power Recycling Cavity (MSPRC). As of this writing, the MSPRC is the baseline, but SYS is holding for the possibility of a SPRC. For the SPRC, the MMT is integrated in the SPRC; in the MSPRC, the MMT is separate. Thus, preliminary MMT designs for both the MSPRC and the SPRC are presented.

9.1.1 Design Philosophy

The MMT design philosophy is governed by the following criteria:

- Minimizing the number of optics after the mode cleaner.
- Adjustment of the mode parameters in the IFO sufficient to meet the requirements through either (re)positioning of the MMT mirrors or adaptive heating of DKDP.
- Provide for diagnostic measurement of the mode-matching.
- Minimize astigmatism and other aberrations introduced into the main beam.
- Allow for steering of the beam into the mode IFO without significant higher order modal contamination.

9.1.1.1 Marginally Stable Power Recycling Cavity MMT

In Initial LIGO, the criteria above led us to select a three element telescope comprised of spherical reflective optics for $MMT_{1,2,3}$.[24] For Advanced LIGO, an analysis of i) the constraints imposed by the physical layout of the IOO in vacuum, ii) the available tuning of the mode matching available using the motion of MMT_1, and iii) the capability for adaptive *in situ* tuning have led us to propose a design where MMT_1 is a flat mirror. For the Advanced LIGO FP arm cavities, the mode matching is relatively insensitive to changes in the position of MMT_1 over possible range of motions on HAM_2. Most significantly, the HAM_2 layout imposes an angle of incidence of 6.675° for MMT_1. Making MMT_1 flat will ensure that no aberrations are introduced in the system. The angles of incidence for MMT_2 and MMT_3 are much smaller (~0.5°) such that the reduction in TEM_{00} power coupling into the arm cavity is less than 0.1%.

9.1.1.2 Stable Power Recycling Cavity MMT

In the case of SPRC, $MMT_{1,2,3}$ are located in the SPRC and will have proper ROC matching to the recycling cavity mode. The beam from IMC will be incident at normal incidence on MMT_1 (or Power Recycling Mirror PRM). The suspensions for MMT_2 and MMT_3 now need to be similar to IMC mirrors.

9.1.2 Design Assumptions

In designing the MMT, the following assumptions are used:

- Values for COC ROC and their tolerances as given in LIGO-E060268, "Advanced LIGO Pathfinder Polish".
- Values for the IMC mirror ROC and their tolerances are as given in Section 9.2.
- TCS will hold the COC ROC to their nominal values, ensuring that IOO will mode match to the same arm cavity mode at all power levels.
- Static or fixed errors will be corrected by changing the distance between MMT_2 and MMT_3. Adaptive heating will be used to correct dynamic (power-dependent) errors in the IO.
- Aberration and wavefront modeling done for the initial LIGO MMT (see LIGO-T970143-00-D) showed that achievable surface figure errors in polishing and coating did not contribute to degradation of the wavefronts.[25] In addition, for small angles of incidence on the curved MMT mirrors, the introduced astigmatism did not compromise the theoretical amount of TEM_{00} matched in the FP arms.
    - A 0.1% reduction in TEM_{00} power coupling is allocated for astigmatism that restricts the angles of incidence to less than 0.6^0 on curved mirrors. Details are included in Section 9.2.5.2.

[24] LIGO-T970143-00, Design Considerations for LIGO Mode-Matching Telescopes, T. Delker, et al.

[25] Ibid

9.2 MSPRC MMT

9.2.1 Optical Layout of MMT

Figure 9.1 shows the conceptual layout and definition of parameters. Table 12 lists the design parameters for MSPRC. The distance values in Table 12 come from the IOO optical layout. MMT radii of curvature were determined using an ABCD Gaussian propagation code and an optimization routine.[26]

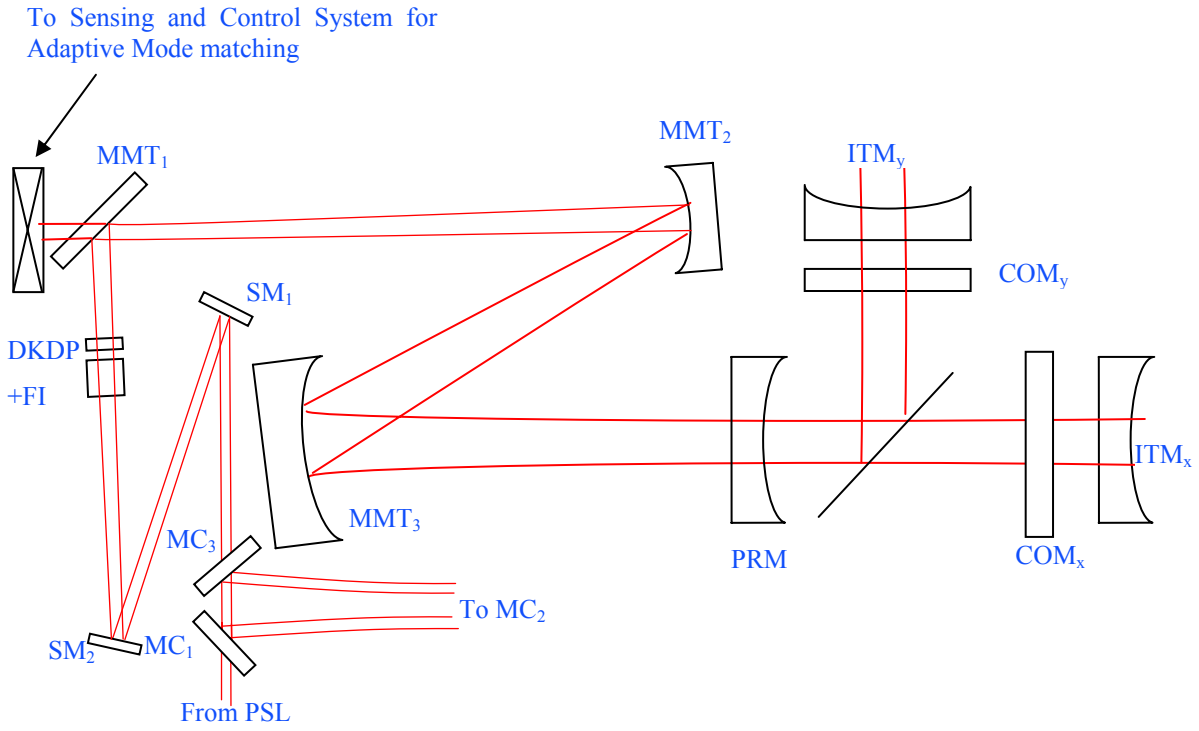

Figure 9.1. Marginally Stable Recycling Cavity Optical Layout. $MMT_{1,3}$ are located on HAM_2; MMT_2 is located on HAM_3. Ring Heater (RH) of DKDP is used for adaptive adjustment.

9.2.2 MMT Design Parameters

Table 12. Parameters for MSPRC

Definition	*Unit*	*Value)*
W_{imc} = Waist Size in IMC	mm	2.1028

[26] POINTER TO YOUR MATLAB CODE

d_{mf}= Distance b/w IMC waist and FI	m	3.1925
d_{fs} = Distance from FI to MMT_1	m	0.5539
MMT_1 radius of curvature	m	>10000
d_{12}= Distance b/w MMT_1 and MMT_2	m	16.8488
R_2 = MMT_2 ROC	m	1.8135
d_{23}= Distance b/w MMT_3 and MMT_3	m	15.54088
R_3 = MMT_3 ROC	m	28.7936
d_{pr}= Distance b/w MMT_3 and PR	m	15.40822
R_{pr}= PR ROC	m	1436.1
d_{pb}= Distance b/w PR and BS	m	3.50880
d_{bs}= BS Effective thickness	mm	68.783
d_{bt}=Distance b/w BS and ITM	m	4.5
R_{itm} = ITM ROC	m	2076
w_c = Reqd. beam waist size in arm	mm	11.53
w_{itm} = Spot Size at ITM	cm	6.0
d_c= Beam waist location from ITM	m	2000
θ_1= Incident angle at MMT_1	degree	44.88
w_1= Spot Size at MMT_1	Mm	2.2
θ_2= Incident angle at MMT_2	degree	0.62
w_2= Spot Size at MMT_2	mm	3.9
θ_3= Incident angle at MMT_3	degree	0.74
w_3= Spot Size at MMT_3	cm	6.13
w_{pr}= Spot Size at PR	cm	6.03

9.2.3 Preliminary Mirror Component Specifications

General optical component specifications for the MSPRC are represented in Table 12

Table 13. Component Specifications

Definition	***Unit***	***MMT1***	***MMT2***	***MMT3***	***Notes***
Marginally Stable Power Recycling Cavity					
Substrate material		Fused Silica	BK7[1]	BK7[1]	[1] See 9.2.3.1
AR Surface ROC	m	>10000	>10000	>10000	
Diameter	mm	75.0, +1, -0	75.0, +1, -0	265.0, +1, -0	
Thickness	mm	25.0, +0, -0.5	50.0, +0, -0.5	100, +0, -0.5	
Wedge Angle/orientation	Arc minutes	30, +10, -0	30, +10, -0	120, +10, -0	

HR Surface Reflectivity (Intensity)		>0.9999	>0.9999	>0.9999	
Clear Aperture	mm	>60	>60	>250	
HR Surface ROC	m	>10000	1.813, ±0.05[2]	28.82,±0.025 [2]	[2]Similar to LIGO1

Note that the tolerances on ROC are similar to Initial LIGO. These tolerances are determined that any error in ROC can be compensated by repositioning MMT_2 with less than 0.5% drop in TEM_{00} power coupling into the arm cavity.

9.2.3.1 MMT Substrate Material

To allow for unanticipated problems in TCS during commissioning and the maximum possible flexibility in IFO thermal compensation methods, we adopt BK7 as material for the MMT mirrors. This is done in order to take advantage of the 10 times larger thermal expansion coefficient of BK7 relative to FS in the event that TCS adaptive control is needed on those mirrors.

The IOO layout allows for the injection of CO_2 heating beams onto MMT_2 and $MMT_{,3}$ should they be needed. Similarly provision will be made for an anticipated ring heater at MMT_3 to help in TCS operation. The CO_2 laser system was designed to exploit the huge dynamic range available for adaptive mode matching if this is required on account of thermal lensing in the core optics components. The current understanding and goal of TCS is to keep the mode in the arm cavity and the recycling cavities at the nominal value. Therefore the CO_2 heating system is currently not in the baseline design. However, we have included the capability for CO_2 beam injection in the optical layout, so that if thermal problems in the core optics arise, a CO_2 laser system may be installed.

9.2.3.2 Thermal Effects in MMT Mirrors

Thermal effects in MMT mirrors can be completely neglected. The power incident on $MMT_{2,3}$ is 125 W and at 1 ppm coating absorption, the amount of heat absorbed is 100 μW. Therefore no correction is required for thermal effects in MMT mirrors.

9.2.4 Adaptive Mode Matching

Adaptive mode matching will be required to compensate for thermal effects in FI. There is a passive thermal compensation through DKDP crystal for FI. However, there might be some residual thermal lensing left. Also, IMC mirror thermal lensing may contribute to mode miss-match in the interferometer. Therefore, an adaptive system is proposed where the DKDP will be installed with a RH around its barrel for adaptive mode matching.

A four-segment RH design has been chosen to allow compensation for astigmatic thermal lensing in the IMC substrates. Moreover, this can also serve to compensate for astigmatism produced by other components, e.g., astigmatism from the PSL, astigmatism due to non-normal incidence angles on mirrors, or astigmatism in the Faraday Isolator, Although the combined losses due to these effects are estimated to be less than 1%, including a four-segment RH does not provide any significant technical challenge and does provide considerable flexibility.

9.2.5 MSPRC Mode Matching Operation and Performance

- Static errors in IOO ROC will be corrected by changing the distance between MMT_2 and MMT_3. The ROC tolerances to MMT mirrors is assigned in such a way that mode matching can be improved to 99.9% for the worst case scenario in ROC errors through distance position change of MMT_2 in MSPRC.
- The proposed dynamic system of adaptive heating on DKDP is capable of handling both the thermal effects in IMC as well as any residual thermal lensing in FI. Using the proposed RH, 99.5% mode matching can be restored at full power.
- Assuming simultaneous occurrence of various errors, the proposed MMT is designed to recover > 99% mode matching in the following manner:
    - Static errors due to MMT_2, MMT_3, IMC mirrors, and tolerances at their worst case values are corrected by changing the distance between MMT_2 and MMT_3.
    - The passive DKDP compensation and adaptive DKDP compensation via RH on DKDP can correct the residual thermal lensing in FI such that the mode matching loss is less than 0.5%.

9.2.5.1 COC Variations

The beam waist location and beam waist size inside the arm cavity are not independent quantities. Any change in the arm cavity mirror ROC due to figure errors affects both beam waist size and location. LIGO-E060268 provides:

- Absolute ROC = 2076 – 2137 m
- Arm cavity ITM-ETM ROC mismatch tolerance = ± 3 m

Using the range of absolute ROC values, the possible beam waist location and size is shown in Figure 9.2. Using a fixed MMT design will introduce static mode-mismatch in the arm cavity with a worst case coupling efficiency drop of 3.0% assuming worst case tolerances in the ROC of the COC and the IOO and appropriate re-positioning of the MMT mirrors. This mismatch is still tolerable under the IOO requirements of maintaining more than 95% coupling efficiency. However, adaptive mode-matching system consisting of CO_2 heating at MMT_2 and a RH at MMT_3 can be installed in future if needed be.

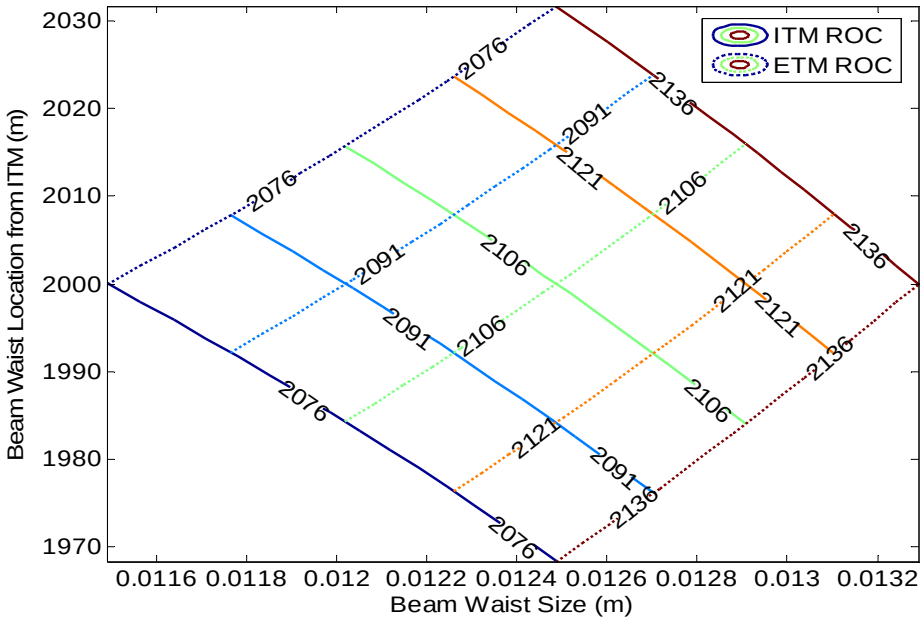

Figure 9.2. Modal Space showing the beam waist location and beam waist size inside the arm cavity as ITM and ETM ROC are varied from 2076 m to 2137 m exploring every possible combination of the two cavity mirrors. The solid lines are the contour of constant ITM ROC.

9.2.5.2 Assignment of ROC Tolerances for MMT_2, MMT_3

The ROC tolerances on MMT_2 and MMT_3 are assigned in such a way that the mode mismatch due to these tolerances can be mitigated independently by repositioning of the MMT optics to recover 99.9% mode-matching. The tolerances (similar to initial LIGO MMT specs) are presented in Table 13.

The designed value of MMT_2 ROC is 1.8130 m and the tolerance is ± 0.05 m while designed value of MMT_3 ROC is 28.7936 and the tolerance is ± 0.025 m. In terms of normalized value, this is equivalent to a ±3.0 % (0.03 Normalized) of the designed MMT_2 ROC. Similarly for MMT_3 the respective tolerance corresponds to a ROC of 17 km (± 12.0 $\times 10^{-5}$ Diopter). In terms of normalized value, this is equivalent to a ±0.15 % (0.0015 Normalized) of the designed MMT_3 ROC.

9.2.5.3 Mode Matching Adjustments for the MSPRC

9.2.5.3.1 Static Error Sources

Static errors in IOO may consist of IMC curved mirror ROC tolerance resulting in IMC waist miss-match from the IFO mode, incorrect positioning of the optics from IMC flat mirrors to the MMT_1, incorrect positioning of $MMT_{2,3}$, and ROC tolerance of MMT_2 and MMT_3 assuming that TCS holds the ETM/ITM curvatures to their nominal value of 2076 m. The contribution of these errors to the mode matching drop is presented in Table 14.

Table 14. Static Errors Sources and Mode Mismatch

Static Error Source	Nominal Value	Tolerance		Mode Mismatch
		Values	%	%
IMC Waist	2.1028 mm	±4 mm	±1.0	0.01
Distance from IMC-MMT_1	3.7464 m	±24 cm	±6.5	0.01
MMT_2 ROC	1.8130 m	±0.05 m	±3.0	36
Moving MMT_2 [A]		±15 mm		14
Moving MMT_2		±1.5 mm		0.16
MMT_3 ROC	28.7936 m	±0.025 m	±0.15	12
Moving MMT_3 [A]		±15 mm		14
Moving MMT_3		±1.5 mm		0.16
Moving PR Mirror		±15 cm		0.0002
Moving ITM		±4.5 cm		0.0001

Note A: This is for controlling purposes. Otherwise, the expected tolerance on positioning is ±1.0 mm.

Here, Table 14 shows that a budget of 0.5% mode mismatch is adequate except for the ROC tolerance of $MMT_{2,3}$. However, as is evident from Note A above, repositioning MMT_2 and MMT_3 can alter the mode mismatch quite significantly. Therefore we can use this distance to correct errors in ROC tolerances of MMT mirrors. Moving either $MMT_{2,3}$ changes the distance between these mirrors but since moving MMT_2 is easier because it is a smaller mirror, therefore for static error correction for ROC tolerances of MMT mirrors will be mitigated by repositioning MMT_2.

In fact, the tolerances on MMT_2 and MMT_3 are assigned such that more than 99.5% mode matching can be recovered by repositioning of MMT_2.

When the MMT ROCs are at their worst case values, mode matching drops to 40% with no repositioning. Mode matching into the arm cavity is far more sensitive to MMT_3 ROC. Therefore it is suggested that MMT_3 is fabricated first and ROC measured and then accordingly MMT_2 ROC is assigned.

9.2.5.3.2 Static Error Correction

To correct these static ROC errors, the position of MMT_2 is optimized. Changing position of MMT_2 by 1 cm means that the distance between MMT_1-MMT_2 and MMT_2-MMT_3 is changed by 1 cm. Using a search algorithm, the distance change that gives the maximum of mode matching is selected. Analysis in the MMT design document shows that mode matching can be recovered to 99.9% for all possible combinations of ROC tolerances. Figure 9.3 shows improved mode matching after reposition MMT_2 to an optimal value.

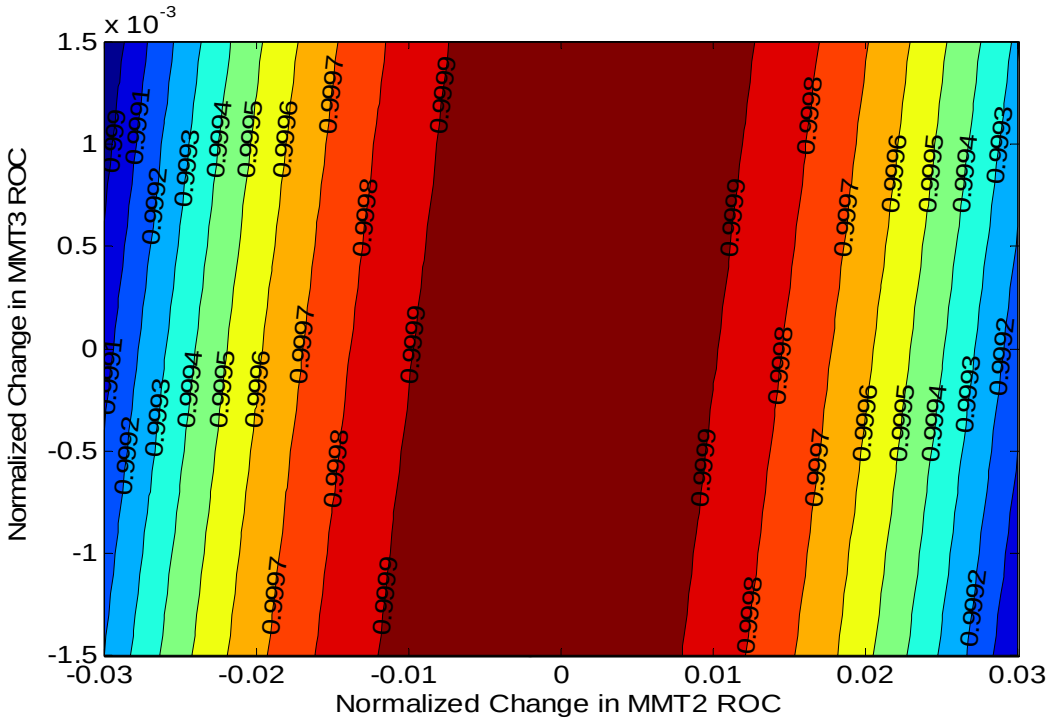

Figure 9.3. Improved mode matching as a result of repositioning MMT2 mirror to correct static errors in MMT2 and MMT3 ROC. The lines are contour of constant mode matching. The worst case mode matching is 99.6%.

9.2.5.3.3 Static Error Corrections using Adaptive Heating

Adaptive heating of MMT_2 and MMT_3 can be used to correct static errors also. However, this is not currently being planned but keeping the option of heating these mirrors, can be used further to improve mode matching if needed be.

9.2.5.3.4 Dynamic Error Correction using Adaptive Heating

Adaptive heating will be built into the IOO MMT to compensate for power-dependent thermal lensing in the IOO optical components (Faraday Isolator, IMC optics) via RH installed on DKDP.

9.2.6 Preliminary Adaptive Mode Matching Specifications

The DKDP serves two purposes. It passively compensates for the FI lensing. For optimal compensation, the length has to be selected very precisely and the absorptions should be known very precisely. In actual practice, there will be some residual thermal lensing left. It is proposed that the length be such selected that the residual thermal lensing is always negative. This will ensure that the positive thermal lensing in the IMC flat mirror will compensate the residual FI lensing. Furthermore, the RH on DKDP will adaptively provide compensation for thermal lensing in FI. RH will provide an *in-situ* adaptive positive lensing element.

Another responsibility of DKDP adaptive compensation is to mitigate the effect of astigmatic thermal lensing in IMC flat mirror. However, if we even neglect the astigmatic lens unchecked, the mode miss-match is of the order of less than 0.5%. In principle, the DKDP will be designed in such a way that we can produce an astigmatic lens in the DKDP using RH.

9.2.6.1 Optical Dynamic Range

The thermal lensing in MIO will actually help in relaxing the amount of compensation required at DKDP using RH. However, as a worst case we can assume that the there is no thermal lensing in IMC mirrors. Then the optimal correction is equal to the negative of residual thermal lensing in FI as shown by blue straight line in Figure 9.4 for every value of residual thermal lensing in FI. Any thermal lensing in IMC will help in reducing the amount of correction needed at RH.

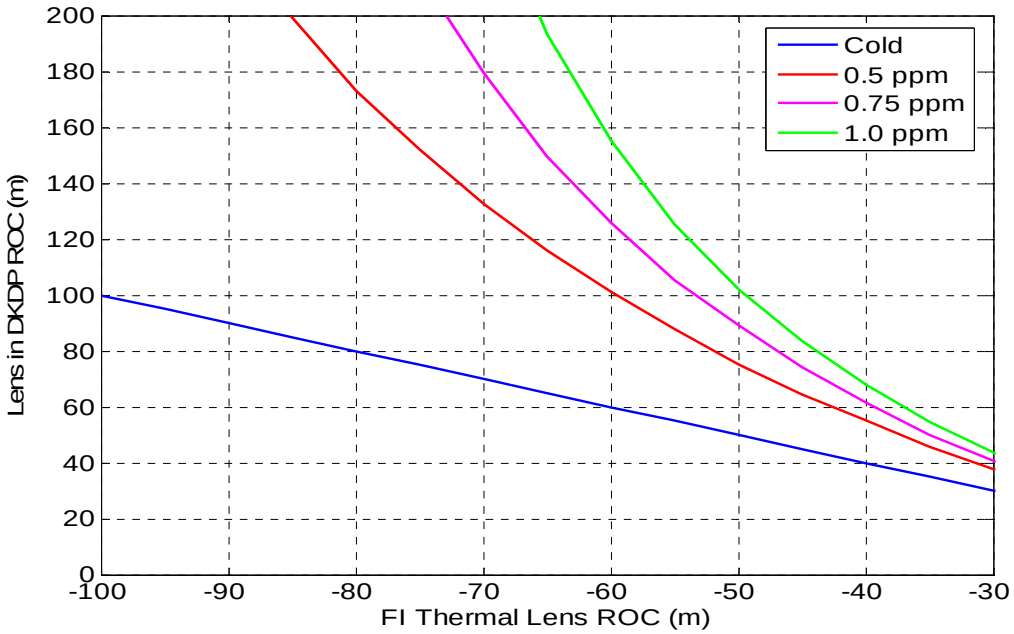

Figure 9.4. Optimal ROC required at DKDP via RH for improving the mode matching. The resultant mode mismatch becomes less than 0.25% if we apply the required correction at the DKDP for a given value of residual thermal lensing in FI.

A worst case thermal residual lensing in FI could be -60m ROC. Using this estimate, the dynamic range for the RH at DKDP should be from -60m to infinity.

9.2.6.2 Ring Heater Specifications

The RH for DKDP will consist of four segments of Nichrome Wire placed as shown in Figure 9.5. Here $RH_{1,2}$ will be used to provide compensation for the horizontal direction while $RH_{2,4}$ will be used for compensating for vertical direction. The exact details of required compensation depend upon FI performance. A servo loop will control the amount of power into the RH based upon the beam width measurements described in 1.2.6.3.

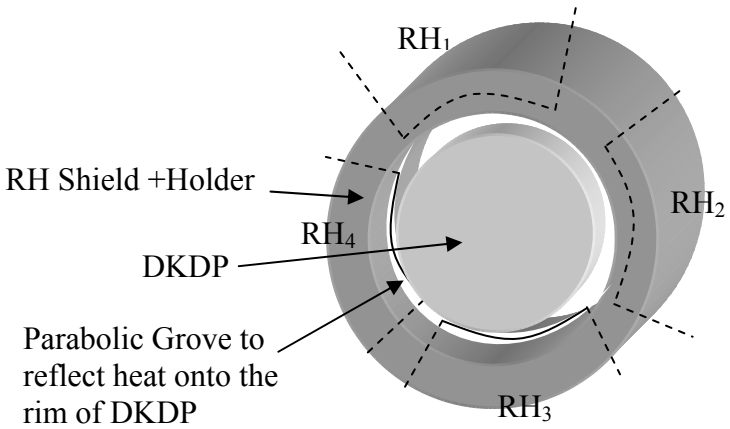

Figure 9.5. Conceptual layout of DKDP RH design. The parabolic groove will ensure that a constant flux from the heating Nichrome wire element incident on the rim of DKDP.

9.2.6.3 Sensing and Control Adaptive Heating

Sensing and control of adaptive mode matching is realized by measuring the beam width of the laser beam transmitted through MMT_1. The optical layout is shown in Figure 9.6. Here the transmitted (or leaked) beam through MMT_1 coming from FI is used to monitor the combined residual thermal lensing in FI, DKDP, and IMC mirrors. A quad photodetector is used to monitor the position of the beam and can be used for steering the beam in the right direction. The sensing of the residual thermal lensing is realized through the beam width measurements by the CCD Camera. The effect of thermal lensing on the beam width is shown in Figure 9.7.

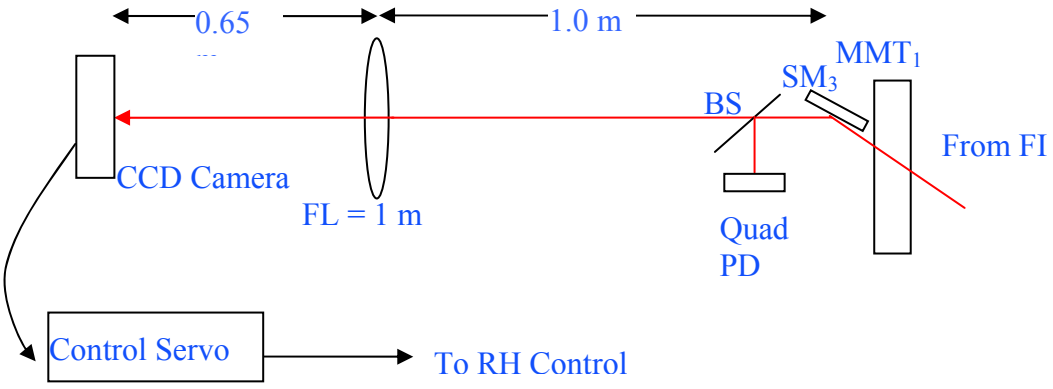

Figure 9.6. Sensing and control of adaptive mode matching in the IOO. Steering mirror SM3, BS, and Quad photodetector are located in vacuum while the lens and the CCD camera are

located outside the vacuum chamber. A control servo converts the beam width data to four control signals to the four DKDP RHs.

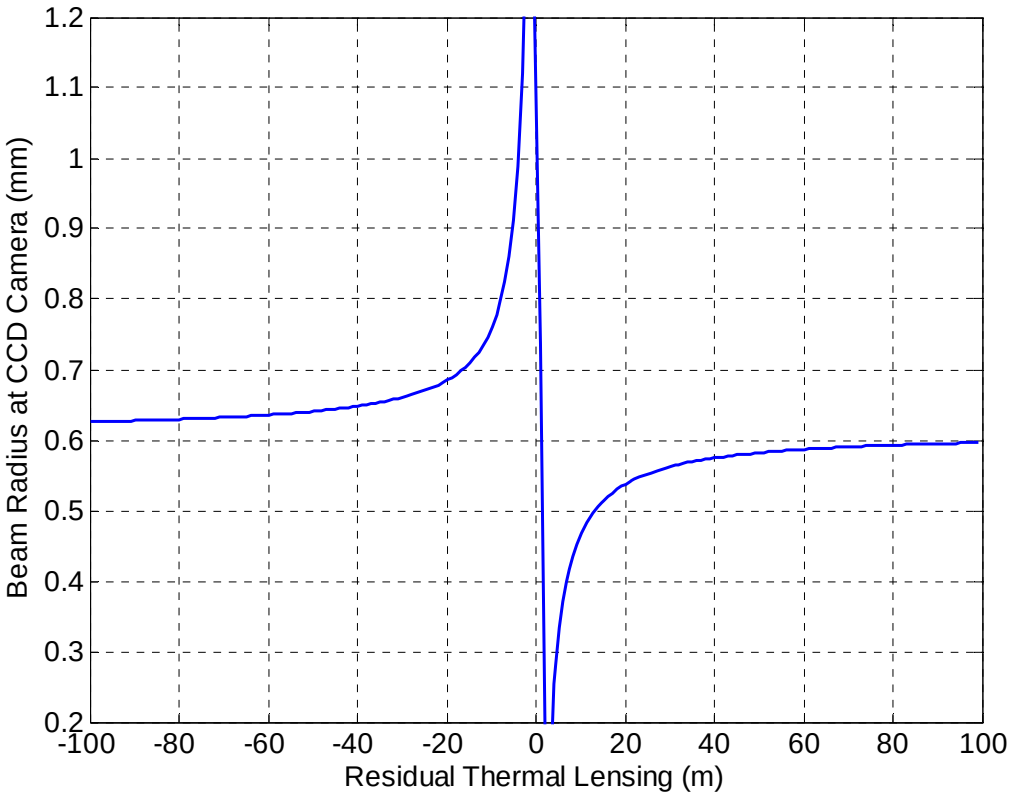

Figure 9.7. Beam radius at CCD in Figure 9.6 as a function of residual thermal lensing in FI, DKDP, and IMC mirrors.

As mentioned earlier that the residual thermal lensing is expected to be negative but the system is capable of differentiating between positive and negative thermal lensing. Figure 9.7 shows that if the beam width is more than a certain threshold value (0.61 mm in this case for the specific geometry used) the residual thermal lensing is negative and the beam width increases as the residual thermal lensing gets stronger. This beam width data can then be used to control the current in DKDP RH. Here, beam width in two orthogonal directions should be measured so that any astigmatism present due to astigmatic nature of IMC thermal lensing or birefringence of optical components can be corrected. The exact details of the control servo will be finalized later based upon RH design.

9.2.6.3.1 CCD Camera

Based upon available data, Spiricon L230 CCD camera is selected to be used in beam width measurements. This CCD camera comes with a software package and USB2 connection and hence

can be readily integrated into the electronic control system. Any extra frame-grabber is not required with this CCD camera.

9.3 SPRC Mode Matching Telescope

An alternate design for the recycling cavity is the Stable Power Recycling cavity. Here the MMT is incorporated in the recycling cavity and the cavity G-factor becomes 0.4. Depending upon the parametric instabilities, alignment control, and layout considerations, either of the two designs may be selected for the final design. Therefore, both designs are being considered for the IOO design document.

9.3.1 Optical Layout of Mode Matching Telescope

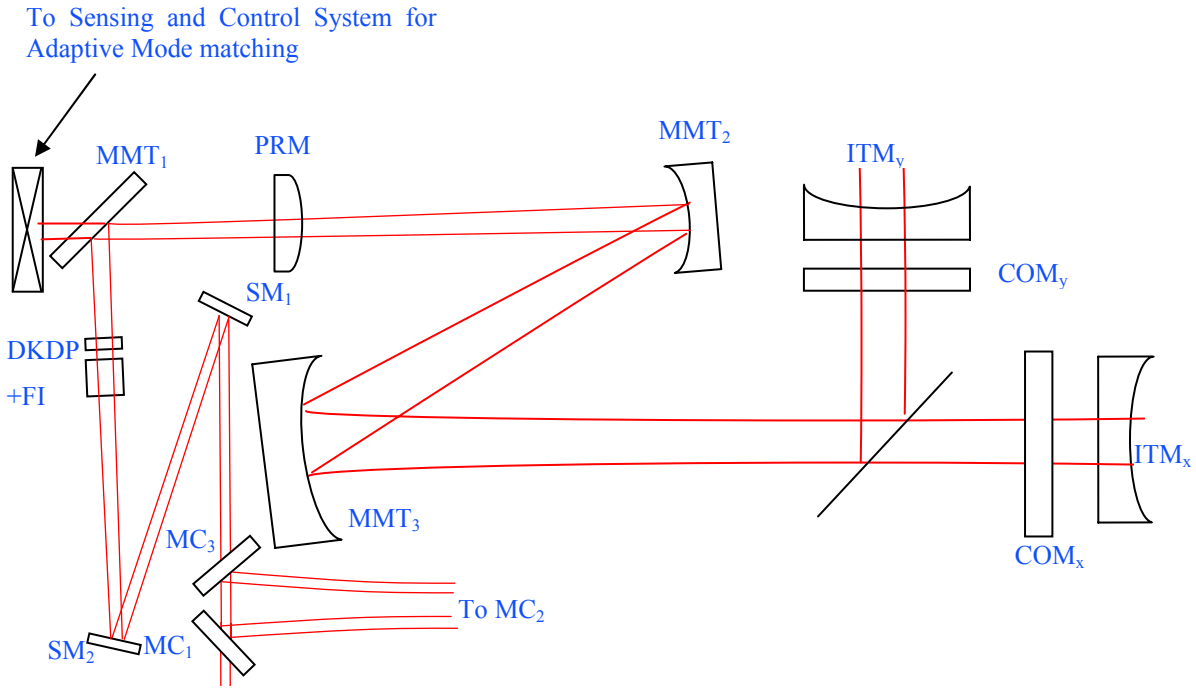

Figure 9.8. Optical layout of Stable Power Recycling Cavity. PRM and MMT3 are located on HAM2; MMT2 is located on HAM3. The main difference between SPRC and MSPRC is the position of the PRM. In SPRC, PRM replaces MMT_1.

Same procedure was used as outlined in Section 9.2.1 for determining the ROC of MMT mirrors. The distance values in Table 15 come from the IOO optical layout.

9.3.2 MMT Design Parameters

Table 15. Parameters for SPRC

Definition	*Unit*	*Value)*
w_{mc} = Waist Size in IMC	mm	2.1028
d_{mf}= Distance b/w IMC waist and FI	m	3.1925
d_{fp} = Distance from FI to PR	m	0.5539
PR radius of curvature	m	-70.3
d_{12}= Distance b/w PR and MMT_2	m	16.585
R_2 = MMT_2 ROC	m	1.8560
d_{23}= Distance b/w MMT_2 and MMT_3	m	16.655
R_3 = MMT_3 ROC	m	31.059
d_{mb}= Distance b/w MMT_3 and BS	m	20.655
d_{bs}= BS Effective thickness	mm	68.783
d_{bt}=Distance b/w BS and ITM	m	4.5
R_{itm} = ITM ROC	m	2076
w_c = Reqd. beam waist size in arm	mm	11.53
w_{itm} = Spot Size at ITM	cm	6.0
d_c= Beam waist location from ITM	m	2000
θ_1= Incident angle at PR	degree	0.0
w_1= Spot Size at PR	mm	2.2
θ_2= Incident angle at MMT_2	degree	0.745
w_2= Spot Size at MMT_2	mm	3.7
θ_3= Incident angle at MMT_3	degree	1.265
w_3= Spot Size at MMT_3	cm	6.11

9.3.3 Preliminary Mirror Component Specifications

Table 16. Component Specifications

Stable Power Recycling Cavity					
Substrate material		Fused Silica	BK7[1]	BK7[1]	[1]See 9.3.3.1
AR Surface ROC	m	>10000	>10000	>10000	
Diameter	mm	150.0, +1, -0	150.0, +1, -0	265.0, +1, -0	
Thickness	mm	75.0, +0, -0.5	75.0, +0, -0.5	100, +0, -0.5	

Wedge Angle/orientation	Arc minutes	30, +10, -0	30, +10, -0	120, +10, -0	
HR Surface Reflectivity (Intensity)		0.9985	0.9999	0.9999	MMT_1 transmission specified by required PRC gain
Clear Aperture	mm	125	125	250	
HR Surface ROC	m	-70.3, ±2	1.856 ±0.05	31.059,±0.25	

9.3.3.1 MMT Substrate Material

Same as Section 9.2.3.1.

9.3.3.2 Thermal Effects in MMT Mirrors

The power incident on $MMT_{2,3}$ is 2.1 kW and at 1 ppm coating absorption, the amount of heat absorbed is 2.1mW. This results in a 2 km (3 nm sagitta change) thermal lens at MMT_2 and 6000 km (0.3 nm sagitta change) at MMT_3. Hence the thermal distortion due to coating absorption can be neglected.

9.3.4 Adaptive Mode Matching

The adaptive mode matching using DKDP is independent of the geometry of the recycling cavity and therefore it will remain same for the SPRC.

9.3.5 SPRC Mode Matching Operation and Performance

This section is same as Section 9.2.5. The only difference is that the PRM will also has to be moved by twice the distance by which MMT_2-MMT_3 distance is changed to keep the recycling cavity length constant.

9.3.5.1 Assignment of ROC Tolerances for MMT_2, MMT_3

The ROC tolerances on MMT_2 and MMT_3 are assigned in such a way that the mode mismatch due to these tolerances can be mitigated independently by repositioning of the MMT optics to recover 99.5% mode-matching and by adaptive heating. The tolerances (similar to initial LIGO MMT specs) are presented in Table 16.

The designed value of MMT_2 ROC is 1.8560 m and the tolerance is ± 0.05 m while designed value of MMT_3 ROC is 31.059 and the tolerance is ± 0.025 m. This tolerance on MMT_2 corresponds to a lens with ROC of - 33 m (- 0.06 Diopter). In terms of normalized value, this is equivalent to a ±3.0 % (0.03 Normalized) of the designed MMT_2 ROC. Similarly for MMT_3 the respective tolerance corresponds to a ROC of 17 km (± 12.0 $\times 10^{-5}$ Diopter). In terms of normalized value, this is equivalent to a ±0.15% (0.0015 Normalized) of the designed MMT_3 ROC.

9.3.5.2 Mode Matching Adjustments for the SPRC

9.3.5.2.1 Static Error Sources

The details are similar to the MSPRC design. An added constraint is to move PRM by twice the distance by which MMT_2 is repositioned.

9.3.5.2.2 Static Error Corrections using Adaptive Heating

Adaptive heating of MMT_2 and MMT_3 can be used to correct static errors also. However, this is not currently being planned but keeping the option of heating these mirrors, can be used further to improve mode matching if needed be.

9.3.5.2.3 Dynamic Error Correction using Adaptive Heating

Same as Section 9.2.5.3.

9.3.6 Preliminary Adaptive Mode Matching Specifications

Same as Section 9.2.6.

9.4 Angular Noise

The requirement on the beam jitter $\Delta\phi$ of the beam after the mode cleaner at a given frequency in terms of the amplitude of TEM_{10} mode is given by $|a_{10}| \le 7 \cdot 10^{-9} \sqrt{1+\left(\frac{230Hz}{f}\right)^4} / \sqrt{\text{Hz}}$ assuming a misalignment of 10^{-9} rad for the ITM (from: Beam jitter coupling in advanced LIGO, G. Mueller). At 10 Hz this leads to $|a_{10}| \le 3.7 \times 10^{-6} / \sqrt{\text{Hz}}$. Thus the total angular beam jitter contribution from the input optics should be less than this value.

The input section has one mode cleaner cavity that suppresses the beam jitter from the PSL by a factor 0f 250 (i.e., by 0.004). All the steering mirrors and the MMT mirrors contribute to the beam jitter also. For the case of steering mirrors and MMT mirrors, the contribution to the noise is suppressed by the transfer function of their respective suspension systems. The contribution of each component to angular beam jitter can be calculated by using ABCD matrices from the component to the final point in the chain. We have selected AR side of PRM as the point of evaluation. Using ABCD law, the contribution to the beam jitter is given by:

$$\Delta\tilde{\phi}_x = \sqrt{\left|A \times \tilde{x}\right|^2 + \left|B \times \tilde{\alpha}\right|^2} \quad \text{and} \quad \textbf{(9.1)}$$

$$\Delta\tilde{\phi}_\alpha = \sqrt{\left|C \times \tilde{x}\right|^2 + \left|D \times \tilde{\alpha}\right|^2}$$

Here $\tilde{x}$ is the frequency dependent displacement due to HAM chamber and $\tilde{\alpha}$ is the pitch or yaw of the optical component due to HAM motion. $\Delta\tilde{\phi}_x$ is the contribution to beam jitter due to displacement fluctuations and $\Delta\tilde{\phi}_\alpha$ is the contribution due to angular fluctuations.

Taking into account the suppression due to the optical mount, this can be written as:

$$\Delta\tilde{\phi}_x = \sqrt{\left|A\cdot\tilde{x}\cdot\tilde{\gamma}_x\right|^2 + \left|B\cdot\tilde{\alpha}\cdot\tilde{\gamma}_\alpha\right|^2 + \left|B\cdot\tilde{x}\cdot\tilde{\gamma}_{x\alpha}\right|^2} \quad \text{and} \qquad \textbf{(9.2)}$$

$$\Delta\tilde{\phi}_\alpha = \sqrt{\left|C\cdot\tilde{x}\cdot\tilde{\gamma}_x\right|^2 + \left|D\cdot\tilde{\alpha}\cdot\tilde{\gamma}_\alpha\right|^2 + \left|D\cdot\tilde{x}\cdot\tilde{\gamma}_{x\alpha}\right|^2}$$

where $\tilde{\gamma}_x$ is the damping to displacement (i.e., x to x coupling mainly), $\tilde{\gamma}_\alpha$ is damping to angular motion (i.e., yaw to yaw mainly), and $\tilde{\gamma}_{x\alpha}$ is the damping to displacement dependent angular motion (i.e., x to pitch mainly). Note that here we have only considered the dominant coupling mechanisms. The transfer functions for suspensions are taken from private communication with Mark Barton at University of Glasgow. For the case of fixed mounts, we can take these two damping factors as 1. All other degrees of freedom have much lower damping factors. Note that the resultant contribution to the beam jitter by these mechanisms is being added incoherently. Note that the amplitude of the TEM_{10} mode is related to these two contributions according to:

$$\left|a_{10}\right|_{\Delta\phi} = \sqrt{\left|\Delta\tilde{\phi}_x\cdot\frac{1}{w}\right|^2 + \left|\Delta\tilde{\phi}_\alpha\cdot\frac{\pi w}{\lambda}\right|^2} \qquad \textbf{(9.3)}$$

where w is the beam radius.

The targeted displacement from HAM chamber $\tilde{x}$ is $4.0\times10^{-11} m/\sqrt{Hz}$ at 10 Hz while yaw angular motion $\tilde{\alpha}$ is $2.0\times10^{-12} rad/\sqrt{Hz}$ at 10 Hz (HAM Seismic Isolation Requirements by Peter Fritschel, T060075-00-D and entry at Advanced LIGO wiki by B Lantz). The PSL beam jitter specifications are $374\times10^{-6}/\sqrt{Hz}$ for the amplitude of the TEM_{10} mode at 10 Hz. Allocating equal amount of contribution from angular and displacement beam jitter and multiplying with the conversion factors of w for displacement and $\lambda/(\pi w)$ for angle, $\tilde{x}_{PSL}$ is $5.3\times10^{-7} m/\sqrt{Hz}$ at 10 Hz angular motion $\tilde{\alpha}_{PSL}$ is $4.48\times10^{-8} rad/\sqrt{Hz}$ at 10 Hz. Mode cleaner provides a filtering of about 1/250. Using this formulation, contribution from various components is calculated as shown in the Table below.

Table 17. Contribution to Displacement Beam Jitter from IOO Mirrors

Optical Component	TF from ABCD Matrice		Mounting					F x Damp x Expected Moti		Total
	Dis. to angle A (m/m)	Angle to angle B m/rad	Type	Dis. Damping (γx) m/m at 10 Hz	Dis.-to-Pitch (γxα) rad/m at 10 Hz	Angular Damping (gγ) rad/rad at 10 Hz	No. of Elements	From Dis. m²/Hz at 10 Hz	Angular m²/Hz at 10 Hz	m²/Hz at 10 Hz
PSL/MC	16.3	308.5	MC Filterin	0.004	0.004	0.004	1	3.4E-08	7.8E-08	8.5E-08
From Steering Mir	16.3	269.6	SOS	0.01	0.025	0.0063	3	6.5E-12	2.7E-10	8.1E-10
MMT1	16.3	260.3	SOS	0.01	0.025	0.0063	1	6.5E-12	2.6E-10	2.6E-10
MMT2	16.3	14.3	SOS	0.01	0.025	0.0063	1	6.5E-12	1.4E-11	1.6E-11
MMT3	0.1	15.4	LOS	0.06	0.01	0.002	1	1.6E-13	6.2E-12	6.2E-12
									Total Beam J	**8.53E-08**
									Total Coh. B.	**8.53033E-08**

Table 18. Contribution to Angular Beam Jitter from IOO Mirrors

Optical Component	|TF| from ABCD Matrices		Mounting					TF x Damp x Expected		Total
	Dis. to angle C (rad/m)	Angle to angle D rad/rad	Type	Dis. Damping m/m at 10 Hz	Dis.-to-Pitch (gxa) rad/m at 10 Hz	Angular Damping (ga) rad/rad at 10 Hz	No. of Elements	From Dis. rad/?Hz at 10 Hz	Angular rad/?Hz at 10 Hz	rad/?Hz at 10 Hz
PSL/MC	0.019	0.291	MC Filtering	0.004	0.004	0.004	1	2.78E-12	5.20E-12	5.90E-12
From Steering Mirror	0.019	0.247	SOS	0.01	0.025	0.0063	3	7.44E-15	2.47E-13	7.40E-13
MMT1	0.019	0.236	SOS	0.01	0.025	0.0063	1	7.44E-15	2.36E-13	2.36E-13
MMT2	0.019	0.078	SOS	0.01	0.025	0.0063	1	7.44E-15	7.77E-14	7.81E-14
MMT3	0.069	1	LOS	0.06	0.01	0.002	1	1.66E-13	4.00E-13	4.33E-13
									Total Beam Jitter	**5.97E-12**

The total contribution due to the mirrors in IOO can be calculated by using Eq. 9.3 where $\Delta\tilde{\phi}_x$ and $\Delta\tilde{\phi}_\alpha$ are the total beam jitter values in Table 17 and Table 18 respectively. The beam size to be used is 6.0 cm because we are calculating the amplitude of TEM_{10} mode at the AR side of the PRM. This provides a total beam jitter of $1.77\times10^{-6}/\sqrt{\text{Hz}}$ as compared to the $3.7\times10^{-6}/\sqrt{\text{Hz}}$ limit due to the ITM differential limit. The total contribution is still a factor of two lower than the proposed limit. Table 17 and Table 18 also show that the PSL noise is the main contributing noise source for the beam jitter and the SOSs used for the mode matching optics provide sufficient suppression. Table 19 shows the summary of the above results. Here column 2 of the table shows the total normalized contribution of the optical elements to the beam jitter noise. Column 3 shows the incoherent running sum of the noise contributions. Individually, PSL beam jitter is the main noise contributing factor that is scaled to one. The next significant source is the MMT_3 contribution that is about 23% of the beam jitter noise due to PSL. However as these noise factors add incoherently, the contribution is about 2.6%. Overall there the beam jitter noise contribution from the optical components in the IOO chain is about 4% of the PSL beam jitter contribution.

Table 19. Summary of the Beam Jitter Contribution from Noise Sources

Optical Component	Normalized Contribution	Individual Incoherent Contribution
PSL/MC	1	1
From three Steering Mirror	0.167	0.0139
MMT1	0.053	0.0014
MMT2	0.018	0.0141
MMT3	0.226	0.0263
	Total	**1.0403**

10 Overall IOO Performance

10.1 Optical throughput

The overall throughput based on the IOO layout is given in Table 20. A basis of estimation is given for each subsystem or component. We assume that the PSL will meet it spec of 165 W TEM_{00} at the PSL IOO handoff.

Table 20. Optical throughput

IO Subsystem or Component		*Transmission*	*Cumulative Transmission*	*Basis of Estimation*
From PSL		1.0	1.0	Input beam from PSL
PSL Table Optics				
	CCD pickoff wedge	0.995	0.9950	Fused silica substrate; 300 ppm AR coatings, scatter due to dust from ambient environment
	Lens 1	0.995	0.9900	Fused silica substrate; 300 ppm AR coatings, scatter due to dust from ambient environment
	M1	0.998	0.9880	HR, scatter due to dust from ambient environment
	M2	0.998	0.9861	HR, scatter due to dust from ambient environment
	Lens 2	0.998	0.9841	Fused silica substrate; 300 ppm AR coatings, scatter due to dust from ambient environment
	1/2 wave plate	0.99	0.9743	Quartz components, commercial AR coating
	Thin film polarizer	0.98	0.9548	Measured transmission in P-pol
	MZ EOM	0.9	0.8593	Assumes 50/50 BS, ~100% visibility, m=0.6 in each arm
	M3	0.998	0.8576	HR, scatter due to dust from ambient environment
	EMMT1	0.998	0.8559	HR, scatter due to dust from ambient environment
	EMMT2	0.998	0.8541	HR, scatter due to dust from ambient environment
	EMMT3	0.998	0.8524	HR, scatter due to dust from

				ambient environment
	Pick off wedge	0.995	0.8482	Fused silica substrate; 300 ppm AR coatings, scatter due to dust from ambient environment
	1/2 wave plate	0.98	0.8312	Quartz components, commercial AR coating
	Thin film polarizer	0.99	0.8229	Measured transmission in P-pol
	Lower periscope mirror	0.995	0.8188	HR, scatter due to dust from ambient environment; vertically oriented surface
	Upper periscope mirror	0.998	0.8171	HR, scatter due to dust from ambient environment
Vacuum				0.8171
	HAM1 Vacuum Feedthrough	0.995	0.8131	Fused silica, 300 ppm AR coatings, some scatter
	HAM2 Vacuum Feedthrough	0.999	0.8130	Fused silica, 300 ppm AR coatings, clean environment
	DLC-M1	0.9999	0.8129	HR, clean environment
	DLC-M2	0.9999	0.8128	HR, clean environment
	IMC	0.9	0.7315	Historical data with some optimism thrown in…
	SM1	0.9999	0.7315	HR, clean environment
	SM2	0.9999	0.7314	HR, clean environment
	Faraday Isolator	0.95	0.6948	Measured transmission
	MMT1	0.995	0.6913	5000 ppm transmission, clean environment
	MMT2	0.9999	0.6913	HR, clean environment
	MMT3	0.9999	0.6912	HR, includes worst case beam clip losses, clean environment
Cumulative transmission			**69.1%**	

Based on this estimation, the IOO will deliver approximately 69.1% of the light from the IOO to the PRM, or roughly 114 W. This is less than the requirement, but assumes somewhat conservative values for the scatter loss on the PSL table optics.

The 'bad actors' are the MZ modulation, the IMC, and the Faraday isolator. Of these, there is not much we can do with the MZ and the FI, but if the IMC transmission can be improved to 96%, we can get to ~74%.

11 Diagnostics

11.1.1 PSL Table

11.1.1.1 RF Modulation

The IOO will have an optical spectrum analyzer (Tropel) on the PSL/IOO table for analyzing RF sidebands on the PSL table.

11.1.1.2 RFAM monitor

A fast photodiode (2 GHz, Thorlabs) will monitor the amplitude sidebands of the light after the Mach-Zehnder interferometer. This measurement also needs a RF spectrum analyzer capable of seeing at least three times the highest modulation frequency used.

11.1.1.3 DC photodiode monitor

A photodiode capable of measuring intensity fluctuations at the 10^{-8} RIN noise level will be present to monitor the intensity noise in the DC to 10 MHz range.

11.1.2 Mode Cleaner

11.1.2.1 RF frequency / IMC length

Since we are not actively controlling the sideband frequency relative to the mode cleaner length, an RF photodiode will be used to monitor the amount of sideband power that gets rejected. RF frequency and/or IMC length adjustments can be made manually when necessary.

The IOO will have the capability to monitor IMC cavity ring down times using a fast photodiode on located on the ISC table.

11.1.2.2 IMC mirror alignment

Cameras behind the IMC mirrors can be used to monitor the IMC alignment and also to guide the initial alignment or restore the alignment back to a known value.

11.1.3 Faraday Isolator

11.1.3.1 Polarization losses

The intensity of the second (unwanted) polarization at the second polarizer will be monitored to identify an increase or decrease in the polarization losses.

11.1.3.2 Depolarization and thermal lensing

The other polarization from the second polarizer can also be used to estimate the thermal lensing, including the possible effects of a ring heater around the DKDP, in the FI by measuring the beam diameter with a CCD camera. This image can also be used to gain information about the depolarization by looking at the mode picture.

11.1.4 IFO Mode-Matching Telescope

11.1.4.1 Measurement of Mode-Matched Power

Measurement of mode matched power will utilize two Bull's Eye position sensors to measure the mismatch of cavity waist size and position in the back-reflected light from the IFO.

11.1.4.2 Sensing and Control of Adaptive Heating

The adaptive mode matching needs a quadrant camera and a CCD camera (Spiricon L230) to monitor the effects of the adaptive heating, see Section 9.2.6.3 for more details.

12 Preparation for Delivery

12.1 Preparation

- Vacuum preparation procedures as outlined in LIGO Vacuum Compatibility, Cleaning Methods and Procedures (LIGO-E960022-B-D) shall be followed for all components intended for use in vacuum. After wrapping vacuum parts as specified in this document, an additional, protective outer wrapping and provisions for lifting shall be provided.
- Electronic components shall be wrapped according to standard procedures for such parts.

12.2 Packaging

12.2.1 Small Optics

Vendor provided transport packaging will be used for small optical components (diameter < 7.5cm) as in initial LIGO. At the sites we will use clean trays (D9890509-00) to hold the clean optics.

12.2.2 Mode Cleaner Mirrors and Large MMT mirror

The IMC and MMT mirrors will be packed in specially designed containers. The COC group is developing a design to contain their large optics, although a final design has not been determined. Key elements of the design include o-ring seals to isolate the entire optic from the atmosphere, as well as Teflon or silicon o-rings used to further seal the optic surface and provide cushioning. The IOO group intends to adapt the final design to the scale of the IMC and Large MMT mirrors.

12.3 Marking

Appropriate identification of the product, both on packages and shipping containers; all markings necessary for delivery and for storage, if applicable; all markings required by regulations, statutes, and common carriers; and all markings necessary for safety and safe delivery shall be provided.

12.3.1 Vendor-supplied catalog items

For catalog products, vendor-provided model numbers will suffice for identification purposes. For items such as optical components (lenses, mirrors), no marks will be placed on the optics, but items will be identified their packaging.

12.3.2 Vendor-supplied custom items

For non-catalog products, vendors will be requested to provide markings. In the event that is not possible, we will identify parts by labeled packaging until installation.

12.3.3 UF manufactured mechanical and opto-mechanical components

Parts manufactured at UF will have DCC and serial numbers machined into the surface via CNC. Parts which are too small will not have numbers machined into the surface but will be identified by labeled packaging.

12.3.4 Suspended mirrors

Identification of the material shall be maintained through all manufacturing processes. Each component shall be uniquely identified. The identification shall enable the complete history of each component to be maintained (in association with Documentation “travelers”). A record for each component shall indicate all weld repairs and fabrication abnormalities. Serial numbers will be added to the suspended mirrors as noted in the individual manufacturing specifications.

13 Assembly and Installation

13.1 Installation Tooling and Fixtures

The IOO alignment will use fixtures for assembly and installation of the optical components followed by an optical alignment using a low-power beam from the PSL (or another low-power laser co-aligned with the PSL beam). The following tooling and fixtures will be required.

13.1.1 PSL Table

13.1.1.1 Mach-Zehnder Modulation

- Low-power laser
- Single and Quad photodiodes
- Other standard optical lab facilities

13.1.1.2 PSL-HAM injection optics

- TBD awaiting choice of injection location.

13.1.2 In-HAM optics

13.1.2.1 Mode Cleaner Triple Suspensions

The mode cleaner triple suspensions will be provided by SUS. Vacuum preparation, cleaning, assembly, mirror insertion, and mirror balancing will follow SUS procedures, TBD.

After assembly/balancing the following will be needed: (Definition of who is responsible is TBD.)

- Clean storage
- Mechanism to transport towers from assembly area to LVEA
- Apparatus to lift towers over beam tube to access the folded interferometer
- Apparatus to lift, position, and place towers on HAM table
- IO will provide fixtures to define position on HAM table (see below)

LASTI experience could be very helpful here.

13.1.2.2 Small Optics Suspensions

These suspensions will be manufactured by the IOO group, and IOO will be responsible for providing hardware (silver-plated stainless screws, ordinary stainless screws, dowel pins, etc). ISC provides the OSEMS. For assembly IOO will require the following items. (Definition of who is responsible is TBD.)

- Vacuum bake ovens for cleaning parts
- Small arbor press for inserting pins
- Air-bake oven for curing epoxy
- Low power laser and quad photodiode for balancing optic
- SOS EPICS controller for testing OSEMS, balance (from ISC?)
- Clean storage

- IO will manufacture the glue fixtures for attaching magnets (including fixtures for attaching magnets to standoffs)

IO will design and provide fixtures to define the SOS locations.

13.1.2.3 MMT 3 Large Optic Suspension

These suspensions will be manufactured by SUS, including assembly and hardware. ISC provides the OSEMS. After arrival at the site, IOO will require:

- Vacuum bake ovens for cleaning parts
- Glue fixtures for attaching magnets (including fixtures for attaching magnets to standoffs)
- Air-bake oven for curing epoxy
- Low power laser and quad photodiode for balancing optic
- SOS EPICS controller for testing OSEMS, balance (from ISC?)
- Clean storage
- IO will provide fixtures to define position on HAM table (see below)

13.1.2.4 Faraday Isolator

IO is responsible for the Faraday isolator. The Faraday rotator parts (case, magnets, TGG and quartz crystals, polarizers, waveplate, mounts, breadboard, other small parts) will be cleaned and baked individually at a location TBD. IOO will provide apparatus for assembly into a completed rotator at the site. At the site, IOO will require

- Air bake oven for cleaning class B assembly apparatus
- Low power laser and quad photodiode for aligning Faraday
- SOS EPICS controller for testing OSEMS, balance (from ISC?)
- Clean storage
- IO will provide fixtures to define positions of parts on the breadboard and of the breadboard on HAM table (see below).

13.1.2.5 Auxiliary Optical Components

IO will provide any fixtures necessary to define position of auxiliary beam steering mirrors.

13.2 Installation and Alignment Procedures

Major subassemblies (Faraday isolator, Mach-Zehnder modulator, suspended optics) will be prepared in the optics lab or vacuum prep lab, aligned there, and placed into the detector as a unit. Other units (steering mirrors, mode matching optics for the IMC and for the core optics) will be placed in position individually.

13.2.1 Mechanical alignment

The fixtures will index the part to the holes on the table, which are believed to be good to +\- 50 μm (0.002 inch), assuming good shop practices. A complete Solidworks model of the IOO exists, and this will be used to determine the position of the part on its table. Chamber separation is known to +/-1 mm, based on the properties of the initial LIGO mode cleaner.

The fixtures will be in essence L-shaped brackets, touching the part at two points along one edge and at one point along a perpendicular edge. These three touches will set the translational and angular position of the part. In initial LIGO, the IOO group made a universal fixture, with micrometers that could be adjusted to pre-calculated settings. This procedure worked adequately. However, it was tedious to use and risked systematic errors if the installation of the micrometers was not good. Therefore, for advanced LIGO, we will design and make fixtures for each part. These will be simple and can be manufactured in-house at Florida, so costs will not be large.

Fixtures for use in the vacuum chambers will be cleaned and bake to class B standards.

13.2.2 Optical alignment

Optical alignment will employ a low power PSL beam.

On the PSL/IO table, fixed apertures will be used to set the beam height and (with a fixture) lateral position. The components will be aligned to the beam rather than the beam aligned to the component. The alignment process will minimize the pointing and displacement of the beam relative to the fiduciary points. The polarization of the beam will be set perpendicular to the table surface (s-polarization).

In the vacuum chamber, we will use targets attached to the suspension frames for alignment of the beam The input polarization of the light will be rotated to horizontal using a half wave plate positioned at the base of the telescope. This is done to increase the transmittance through IMC1 and IMC3.

Beam height targets will be used to set the beam horizontal, and at the correct height above the table in the HAM. The adjustments will be done either on the periscope mirrors or using mirrors on the PSL/IO table.

Table height and level will need to be monitored and adjusted during this process.

With the mirrors hanging free, the beam will be aligned through the IMC using targets, then by ensuring that the beam closes on itself, using suspension controls. (Small rotations of the towers can be used if the initial pointing is too far off.) We will not try to resonate the IMC in air.

The IMC reflected beams and transmitted beams (the latter taken through SM1) will be aligned into HAM1 and onto the detectors.

The beam will be aligned through the Faraday isolator and the mode-matching telescope in a similar fashion. With the “wrong” polarization being sent through the IMC, the Faraday half-wave plate will need to be adjusted to maximize the transmission through the Faraday for horizontally polarized light. This will have to be repositioned just before vacuum closeup.

Appendix A: Alternate Low Backscatter Beam Dump

An alternate ultralow backscatter beam dump has been designed and tested (Figure A.1) using a commercially available infrared spectrometer gas cell where the light is absorbed in the circulating water containing India ink. A glass cylinder is sealed using fused silica windows at the end with AR coatings at the front and back surfaces. There are two inlets to the cylinder, one for water entering the enclosed cylinder and the other for water going out from the cylinder. An experiment was conducted using 42 W laser power and the results are shown in Figure A.2.

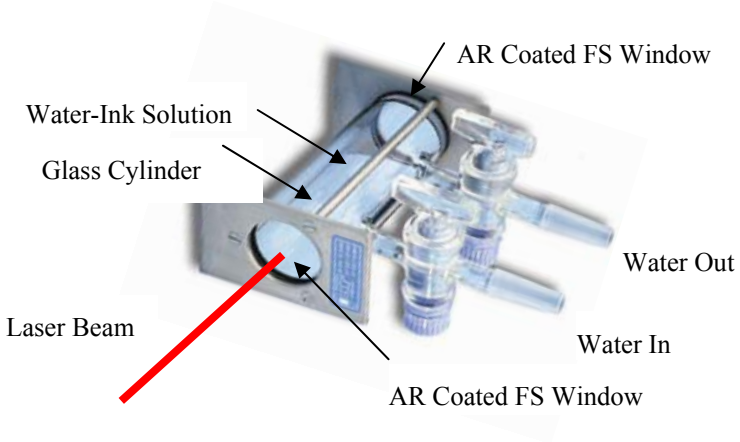

Figure A.1. UF-made beam dump for ultra-low scattering/reflection high power laser power absorption.

As shown in Figure A.2, a 0.8 ml/L solution of India-Ink in water in a 10 cm path can successfully dump 100 W of laser power. The non-specular back-reflectance was minimized by AR-coated fused silica windows (Figure A.1). This option can be used if the commercially available beam dumps do not provide satisfactory requirements in terms of back-reflectance and scattering.

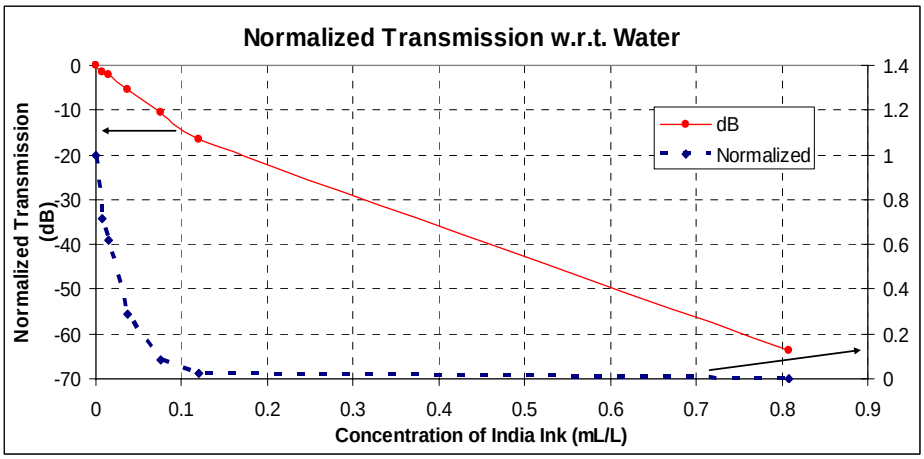

Figure A.2. Experimental results showing the transmission (1 pass attenuation) of the low scatter beam dump.